Fusion in Focus: Unveiling the Roles of Apq12, Brl1 and Brr6 in Nuclear Pore Complex Biogenesis

Azqa Ajmal Khan

2024

Inaugural dissertation

for

obtaining the doctoral degree

of the Combined Faculty of Mathematics, Engineering and Natural Sciences

of the

Ruprecht - Karls - University

Heidelberg

Presented by

M.Sc. Azqa Ajmal Khan

Born in Lahore, Pakistan

Oral examination: 19th June, 2024

Fusion in Focus:
Unveiling the Roles of Apq12, Brl1 and Brr6 in Nuclear Pore Complex Biogenesis

Referees: Prof. Dr. Elmar Schiebel

Prof. Dr. Michael Knop

Acknowledgements

First of all, I would like to congratulate and pat myself on the back for sticking it out. Yay me!

Ami, Abu, Rida, Aimen, Arfaa, you can finally stop asking me "کتنا رہ گیا ہے؟"

Nabeel, I still remember calling you in panic to come meet me at the bakery when one of my experiments kept failing. You've seen it all, across continents. It's been real.

Thank you Elmar for this opportunity and for your continued guidance and input throughout these five years. A special thanks to my TAC members Dr. Michael Knop and Dr. Gislene Pereira for their helpful suggestions along the way. Ex and current Schiebel lab members, this process would've been a lot more tedious and a lot less fun without you all. Thank you for all the memories.

Summary

The nuclear envelope (NE) is a hallmark of eukaryotic cells, functioning as a physical barrier that separates the genome from the cytosol. In organisms with closed mitosis, essential macromolecular complexes like the nuclear pore complex (NPC) and the spindle pole body (SPB) must embed into the NE, requiring the fusion of both the inner (INM) and outer nuclear membranes (ONM). How this fusion of the two membrane bilayers happens remains unclear. In this study, I report that three integral membrane proteins - Apq12, Brl1 and Brr6 - are required in NPC biogenesis by associating with the assembly sites in the NE during the interphase assembly process.

I show that Apq12, Brl1 and Brr6 localize to the NE and endoplasmic reticulum (ER). Each protein carries two transmembrane domains that flank an amphipathic helix (AαH) that is located in the perinuclear space. These amphipathic helices have the ability to localize to the nuclear envelope on their own.

In the first part, I report that the integral membrane protein Apq12 plays a crucial role in modulating the NE/ER and cooperates with NPC biogenesis factors Brl1 and Brr6. Disruption of its AαH (*apq12-ah*) leads to defects in NPC biogenesis and NE integrity, while not affecting the topology or localization of Apq12-ah within the NE/ER. Moreover, overexpression of wild-type *APQ12*, but not the *apq12-ah*, induces pronounced proliferation of the ONM/ER and leads to enrichment of phosphatidic acid (PA) at the NE. Both Apq12 and Apq12-ah are found to associate with NPC biogenesis intermediates, with the mutation of the AαH resulting in elevated levels of Brl1 and increased interaction between Brl1 and Brr6.

In the second part, I show that not only is the AαH of Brl1 essential for its function, but over-expression of its mutant results in the formation of a novel type of herniation; petal-like structures, resulting from failed INM-ONM fusion. Furthermore, it also leads to mislocalization of a number of cytoplasmic nucleoporins, consistent with the inside-out model of interphase NPC assembly.

Lastly, I show that Brr6 also has a role in INM-ONM fusion as ts-mutants with mutations in the cysteine residues lead to the formation of herniations. Over-expression of its AαH mutant $brr6^{L145E}$ causes mislocalization of all nucleoporins except the transmembrane nucleoporins, suggesting an additional role beyond INM-ONM fusion during biogenesis.

Taken together, this work sheds light on the process of membrane fusion during NPC biogenesis. The data shows that the amphipathic α-helix of Apq12 plays a critical role in regulating the functions of Brl1 and Brr6, potentially facilitating PA accumulation at the NE making it more susceptible to deformations. Brl1 and Brr6 also localize to the sites of NPC assembly on the INM and ONM, respectively, and bring the two bilayers together for fusion by interactions between their anti-parallel helix bundles stabilized by two disulfide bridges (DAH).

This study offers a conceptual framework for understanding the fusion of the nuclear envelope during NPC biogenesis. It is highly probable that the fundamental principles are conserved across yeast and humans. Further comparative analysis of the assembly process in other organisms will elucidate these conserved principles.

Zusammenfassung

Die Kernhülle (NE) ist ein Markenzeichen eukaryontischer Zellen und dient als physische Barriere, die das Genom vom Zytosol trennt. In Organismen mit geschlossener Mitose müssen essenzielle makromolekulare Komplexe wie der Kernporenkomplex (NPC) und der Spindelpolkörper (SPB) in die NE eingebettet werden, was die Fusion der inneren und äußeren Kernmembranen erfordert. Wie diese Verschmelzung der beiden Membranschichten vonstatten geht, ist nach wie vor unklar. In dieser Studie berichte ich, dass drei integrale Membranproteine - Apq12, Brl1 und Brr6 - für die NPC-Biogenese erforderlich sind, indem sie sich während des Interphasen-Assemblierungsprozess an die entstehende Kernpore binden und die Fusion beider Kernmembranen bewirken.

Ich zeige, dass Apq12, Brl1 und Brr6 im NE und im endoplasmatischen Retikulum (ER) lokalisiert sind. Jedes Protein besitzt zwei Transmembrandomänen, die eine amphipathische Helix (AαH) flankieren, die sich im perinukleären Raum befindet. Diese amphipathischen Helices haben die Fähigkeit, selbständig an der Kernhülle zu binden.

Im ersten Teil berichte ich, dass das integrale Membranprotein Apq12 eine entscheidende Rolle bei der Modulation des NE/ER spielt und mit den NPC-Biogenesefaktoren Brl1 und Brr6 zusammenarbeitet. Die Unterbrechung seines AαH (apq12-ah) führt zu Defekten in der NPC-Biogenese und der NE-Integrität, während die Topologie oder Lokalisierung von Apq12-ah innerhalb des NE/ER nicht beeinflusst wird. Darüber hinaus induziert die Überexpression von Wildtyp *APQ12*, aber nicht von *apq12-ah*, eine ausgeprägte Proliferation der Kernmembran/ER und führt zu einer Akkumulation von Phosphatidsäure (PA) im NE. Sowohl Apq12 als auch Apq12-ah assoziieren mit Zwischenprodukten der NPC-Biogenese, wobei die Mutation des AαH zu einer erhöhten Konzentration von Brl1 und einer verstärkten Interaktion zwischen Brl1 und Brr6 führt.

Im zweiten Teil meiner Arbeit zeige ich, dass Brl1 AαH nicht nur essentiell für seine Funktion ist, sondern dass die Überexpression einer Mutante mit einem AαH Defekt zur Bildung einer neuen Art von Herniation führt. Herniationen sind deformationen der inneren Kernmembran (INM) in Richtung der äußeren Kernmembran (ONM) und resultieren aus einer fehlgeschlagenen INM-ONM-Fusion. Darüber hinaus führt die Überexpression der *BRL1* Mutante auch zu einer Fehllokalisierung einer Reihe von

zytoplasmatischen Nukleoporinen, was mit dem Inside-Out-Modell der Interphasen-NPC-Montage übereinstimmt.

Schließlich zeige ich, dass Brr6 auch eine Rolle bei der INM-ONM-Fusion spielt, da ts-Mutanten mit Mutationen in den Cysteinresten zur Bildung von Herniationen führen. Die Überexpression der AαH-Mutante *brr6*^{L145E} führt zur Fehllokalisierung aller Nukleoporine mit Ausnahme der Transmembran-Nukleoporine, was auf eine zusätzliche Rolle über die INM-ONM Fusion während der Biogenese hinaus hindeutet.

Zusammengefasst zeigen meine Ergebnisse, dass die amphipathische α-Helix von Apq12 eine entscheidende Rolle bei der Regulierung der Funktionen von Brl1 und Brr6 spielt und möglicherweise die PA-Akkumulation an der NE erleichtert, wodurch diese anfälliger für Deformationen wird. Brl1 und Brr6 lokalisieren an den Stellen des Zusammenbaus von NPCs und bringen die INM und ONM durch Wechselwirkungen zwischen ihren antiparallelen Helix-Bündeln, die durch zwei Disulfidbrücken (DAH) stabilisiert werden, zusammen und schließlich zur Fusion, was den Einbau von neuen NPCs in die NE Doppelmembran erlaubt.

Diese Studie liefert einen konzeptionellen Rahmen für das Verständnis der Kernhüllenfusion während der NPC-Biogenese. Es ist sehr wahrscheinlich, dass die grundlegenden Prinzipien in Hefe und Mensch konserviert sind. Weitere vergleichende Analysen der Fusionsprozesse in anderen Organismen werden diese konservierten Prinzipien aufklären.

Table of Contents

1. Introduction

1.1 The Eukaryotic Cell Cycle

The eukaryotic cell cycle is divided into two main stages: interphase and mitosis. Interphase is the longest stage of the eukaryotic cell cycle, and it is the period of the cell cycle between two consecutive mitotic divisions. During interphase, the cell grows and replicates its genetic material in preparation for cell division. Interphase can be subdivided into three stages: G1, S, and G2, each characterized by distinct cellular events. The first stage of interphase is the G1 phase, which stands for "Gap 1". During G1, the cell is metabolically active, and its primary task is to grow and synthesize proteins and organelles. In this phase, the cell is also subjected to various environmental cues and signaling pathways that help regulate cell growth and division. This stage lasts the longest, and its duration can vary depending on the cell type and its environmental conditions. Following G1, the cell enters the S phase, which stands for " DNA synthesis". During this stage, the cell replicates its DNA in preparation for cell division. DNA replication begins at specific sites in the genome called origins of replication. The process of DNA replication is highly regulated and requires the coordinated activity of various proteins and enzymes. Errors during DNA replication can lead to mutations and genetic instability, which can contribute to the development of cancer. After S phase, the cell enters the G2 phase, which stands for "Gap 2". During G2, the cell continues to grow and prepare for mitosis. In this phase, the cell synthesizes proteins and organelles that are needed for cell division. G2 also serves as a checkpoint in the cell cycle, ensuring that all the genetic material has been faithfully replicated before the cell enters mitosis.

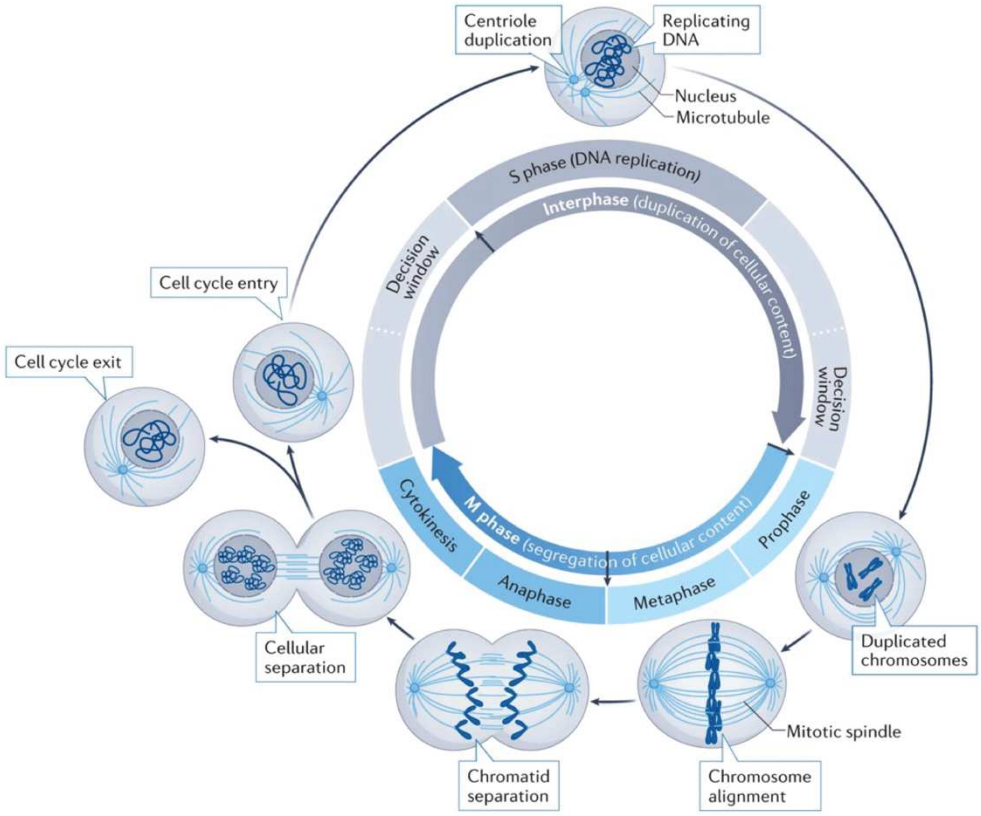

Figure 1. Overview of the phases of the eukaryotic cell cycle. Figure adapted from (Matthews, Bertoli et al. 2022).

Mitosis is the stage of the eukaryotic cell cycle in which the replicated chromosomes are segregated into two nuclei. This process is divided into several phases. The first stage of mitosis is prophase, during which the chromatin condenses and forms visible chromosomes. The spindle apparatus, which is composed of microtubules and centrosomes, also forms during prophase. The centrosomes move to opposite poles of the cell and begin to form spindle fibers that will later attach to the chromosomes. The nuclear envelope (NE) also disassembles, allowing the spindle fibers to access the chromosomes. During prometaphase, the spindle fibers attach to the kinetochores of the chromosomes, allowing them to be pulled apart later during mitosis. The kinetochore is a protein structure located at the centromere of each chromosome that is involved in spindle fiber attachment. The next stage of mitosis is called metaphase, during which the chromosomes are aligned along the equator of the cell, known as the metaphase plate. The spindle fibers, attached to the kinetochores on opposite sides of each chromosome, pull them in opposite directions, aligning them at the metaphase plate. In the next stage, called anaphase, the spindle fibers pull the sister chromatids apart, segregating them to opposite poles of the cell and the cell begins to elongate in preparation for telophase.

Finally, during telophase, the chromosomes arrive at the opposite poles of the cell, and a new nuclear envelope begins to form around each set of chromosomes. The spindle fibers disassemble, and the cell completes cytokinesis, dividing into two daughter cells.

In addition to these stages, the cell cycle has an additional stage called the G0 phase. The G0 phase is a quiescent state in which the cell is not actively dividing. Some cell types in the G0 phase can re-enter the cell cycle under specific conditions or remain in this stage indefinitely (such as neurons). The G1 checkpoint, also called the restriction point, is a critical regulatory point that determines whether the G1 cell will enter S phase or the G0 cell will enter the cell cycle and proceed with cell division.

1.2 Cell Cycle Control

The cell cycle is a tightly regulated process, and each phase is checked to ensure that the generated daughter cells are accurate duplicates of the parent cell and mutation-free. There are three main checkpoints in place near the end of G1, at the G2/M transition, and near the end of the metaphase stage of mitosis (spindle checkpoint). The G1 checkpoint ensures that the cell has enough energy, has no DNA damage and is an appropriate size. Similarly, the G2 checkpoint guarantees complete and accurate chromosome replication. Finally, the spindle checkpoint makes sure that all the sister chromatids are correctly aligned and attached to the microtubules to allow equal segregation. These checkpoints halt cell cycle progression if the cell has not met each of the requirements being evaluated.

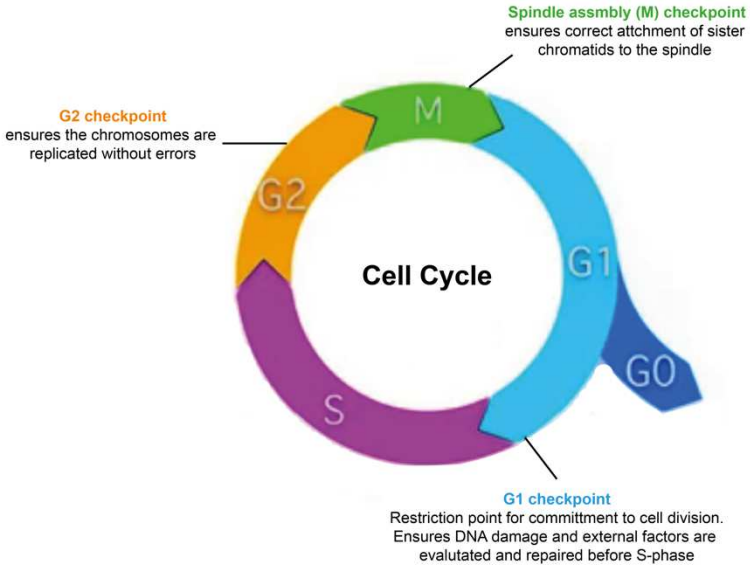

Figure 2. Cell cycle and its checkpoints to ensure production of healthy cells after each round of division.

The key regulators of the cell cycle are cyclins and cyclin-dependent kinases (Cdks). Cyclins are categorized into groups based on the phase of the cell cycle they regulate, with their expression increasing or decreasing during different phases (Murray 2004). The Cdk subunit can bind to various cyclins, and the specific cyclin determines which protein substrates are phosphorylated by the resulting Cdk-cyclin complex. According to the classical model of cell cycle control (Nurse 2000), D-type cyclins and Cdk4 or Cdk6 control early G1 phase events. The S phase is initiated by the accumulation of cyclin E-Cdk2 complex, and completion of the S and G2 phases are regulated by cyclin A-Cdk2 or cyclin A-Cdk1 complexes. The cyclin B-Cdk1 complex then controls mitosis. Protein phosphorylation catalyzed by Cdks and dephosphorylation by phosphatases are important for transition between phases of the cell cycle and its general progression.

Eukaryotes employ two distinct mechanisms to achieve the essential process of cell division; open and closed mitosis. Open mitosis is a mitotic process characterized by the dissolution of the nuclear envelope, allowing direct interaction between the spindle microtubules and the chromosomes in the cytoplasm. Closed mitosis, in contrast, is characterized by the maintenance of the nuclear envelope throughout the entire mitotic process. This process is commonly observed in organisms such as fungi, amoebas, and certain protists. Throughout closed mitosis, the spindle-pole bodies that are embedded in the nuclear envelope, initiate the formation of microtubules within the nucleus. Following the completion of DNA segregation, the nucleus undergoes division. This unique configuration ensures the segregation of chromosomes within the confines of the nuclear compartment (Webster, Witkin et al. 2009, Jaspersen and Ghosh 2012).

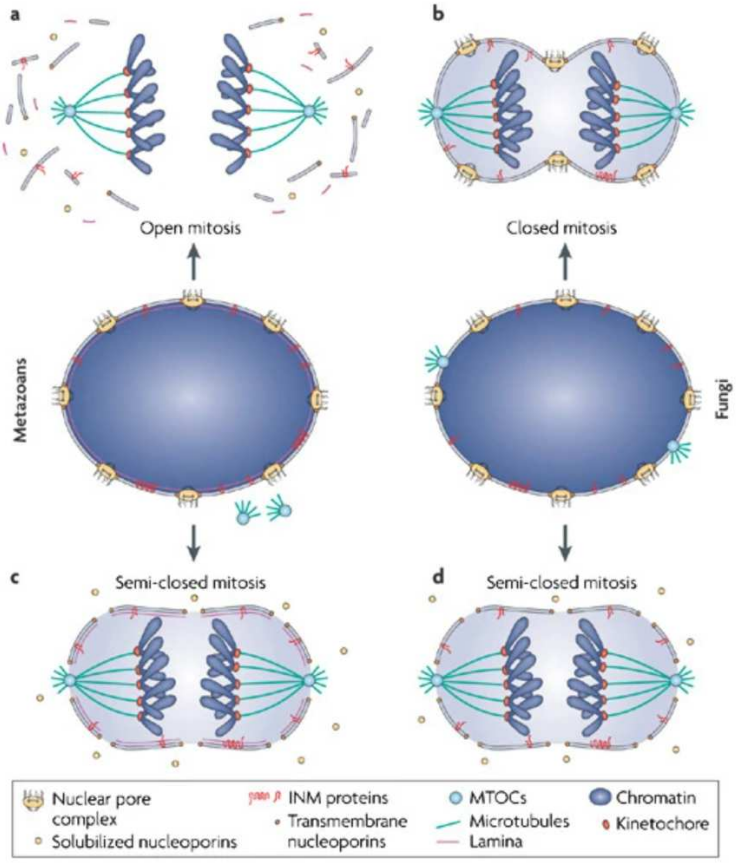

Figure 3. Schematic showing open, closed and semi closed mitosis in metazoans and fungi (Güttinger, Laurell et al. 2009).

1.3 The Nuclear Envelope

The nuclear envelope is one of the defining features of eukaryotic cells. It physically separates the cytoplasm from the nucleoplasm (Franke, Scheer et al. 1981). It is composed of a double membrane known as the inner nuclear membrane (INM) and the outer nuclear membrane (ONM), enclosing a perinuclear space (Afzelius 1955). The INM contains a distinct proteome that associates with the chromatin and the nuclear lamina (McKeon, Kirschner et al. 1986, Solovei, Wang et al. 2013, Pawar and Kutay 2021).

The ONM is continuous with both the smooth and rough endoplasmic reticulum (ER) which contains ribosomes. The perinuclear space is consequently continuous with the ER lumen (Gerace and Burke 1988). The nuclear envelope contains a number of macromolecular structures including the nuclear pore complex and, in the case of yeast, the spindle pole body.

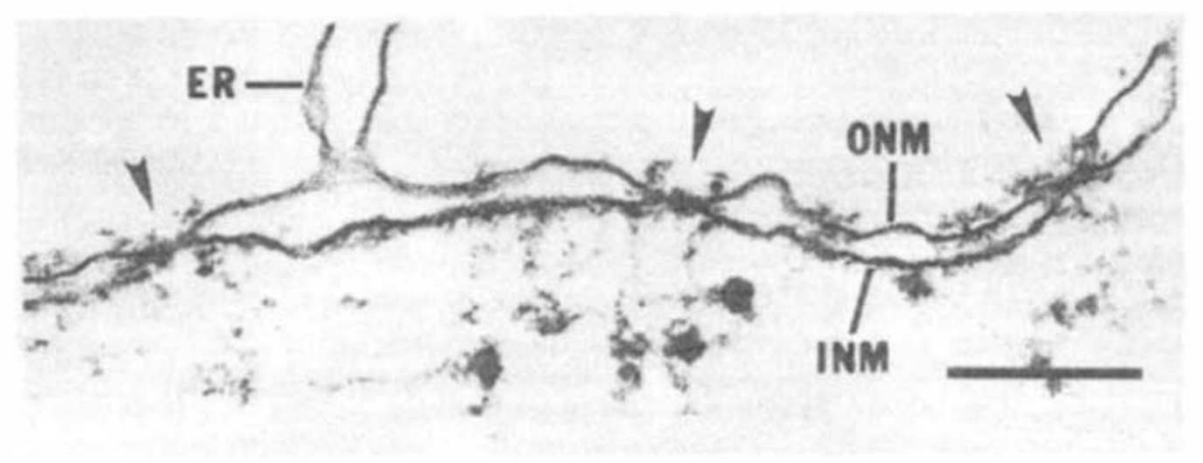

Figure 4. Electron micrograph of the nuclear envelope from *Xenopus laevis* oocyte, showing the INM, ONM, ER and the NPCs (arrowheads) (Gerace and Burke 1988).

1.3.1 The nuclear pore complex

The nuclear pore complex (NPC) is one of the two macromolecular complexes found in the nuclear envelope, the other being the spindle pole body. These NPCs appear in the form of discontinuities in the nuclear envelope, and are involved in nucleocytoplasmic transport. They were first identified in 1949 using electron microscopy (Callan, Randall et al. 1949). Since then, scientists have identified their eight-fold octagonal symmetry (Gall 1967). They are formed at the sites of INM and ONM fusion, and allow bidirectional exchange of materials between the nucleus and the cytoplasm via free diffusion and active transport.

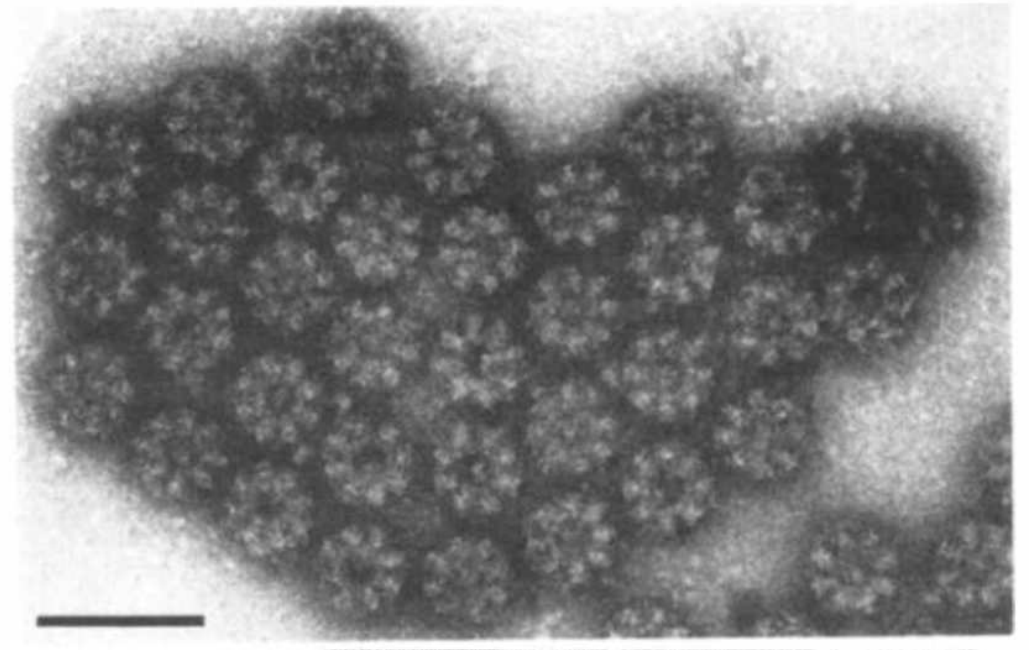

Figure 5. EM image of NPCs from *Xenopus laevis* oocyte, clearly showing eight-fold symmetry. Scale bar: 0.2 μm (Gerace and Burke 1988).

NPCs regulate bidirectional transport in two ways: passive diffusion and facilitated diffusion. Molecules smaller than 40 kDa can translocate freely via passive diffusion (Paine, Moore et al. 1975, Timney, Raveh et al. 2016). To actively ferry cargo across the NE through the NPCs, soluble nuclear transport receptors (NTRs) are used (Moore and Blobel 1993, Görlich, Prehn et al. 1994). These NTRs recognize their cargo by virtue of short amino acid sequences that are called nuclear localization signals (NLS) or nuclear export signal (NES) (Kalderon, Richardson et al. 1984, Wen, Meinkotht et al. 1995). NTRs circulate between the nucleus and the cytoplasm and have the ability to bind to FG Nups allowing the NTR-cargo complexes to penetrate the permeability barrier (Görlich and Kutay 1999, Stewart 2007). Most of the NTRs belong to the karyopherin family of proteins. They are conserved from yeast to humans, and divided into three groups: importins, exportins and biportins. Importins work by binding the cargoes in the cytoplasm, and once inside the nucleus release their cargo upon binding with RanGTP (Chook and Blobel 1999). For export, exportins cooperatively bind cargoes and RanGTP in the nucleus. Upon translocation to the cytoplasm via the NPC, the cargo is released upon hydrolysis of RanGTP to RanGDP (Kaláb, Solc et al. 2011).

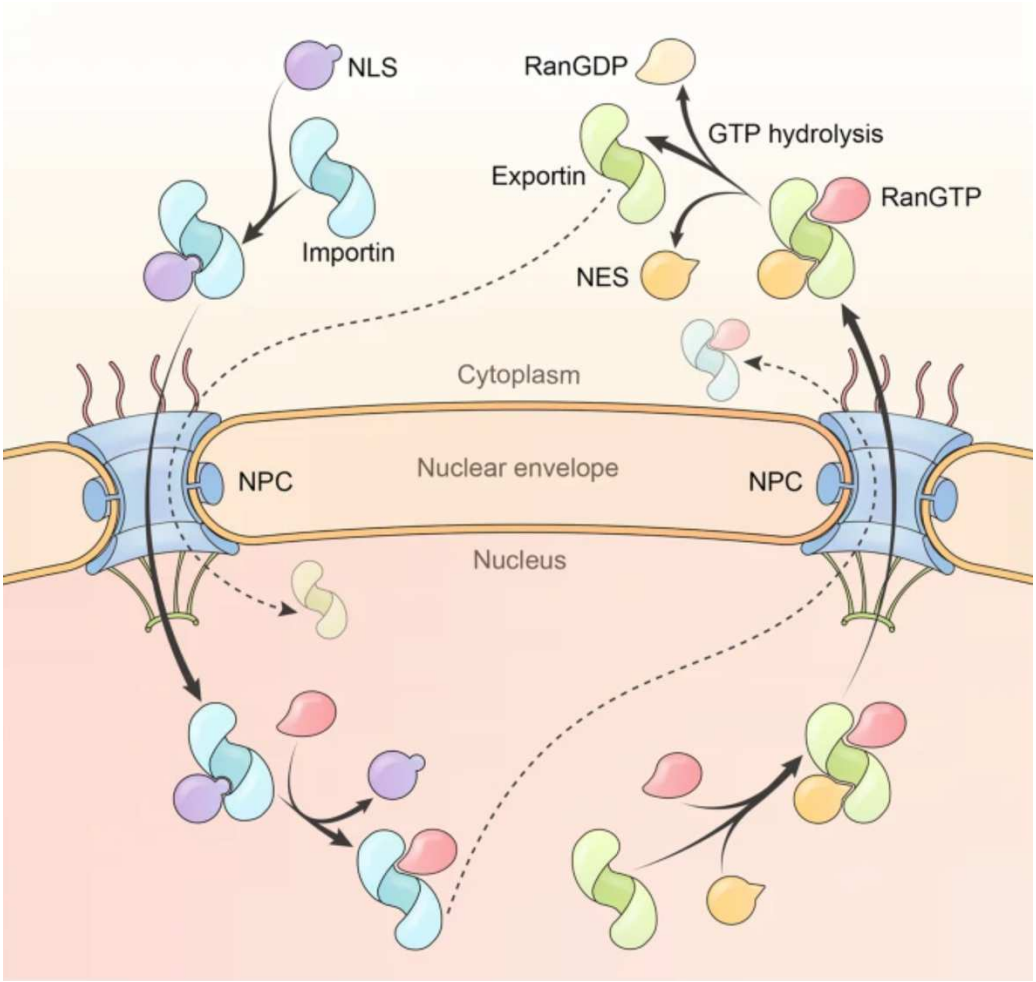

Figure 6. Import and export pathways of cargoes carrying NLS & NES, respectively (Yang, Guo et al. 2023).

The yeast NPC has a molecular weight of approximately 60 MDa, in contrast to 120 MDa in humans. They are formed of about 30 different specialized proteins called the nucleoporins (Nups) in 8-32 copies per NPC. There are three different kinds of Nups that have been identified according to their function, namely; FG Nups, scaffold Nups, and transmembrane Nups. The FG Nups contain phenylalanine-glycine repeats and line the central transport channel and create a permeability barrier. The scaffold Nups are structural in nature, whereas the transmembrane Nups anchor the NPC to the nuclear envelope (Strambio-De-Castillia, Niepel et al. 2010). These Nups come together in the form of different subcomplexes that constitute a mature NPC. These complexes include inner ring, cytoplasmic ring, nuclear ring, cytoplasmic filaments and nuclear filaments (Hurt and Beck 2015, Schwartz 2016).

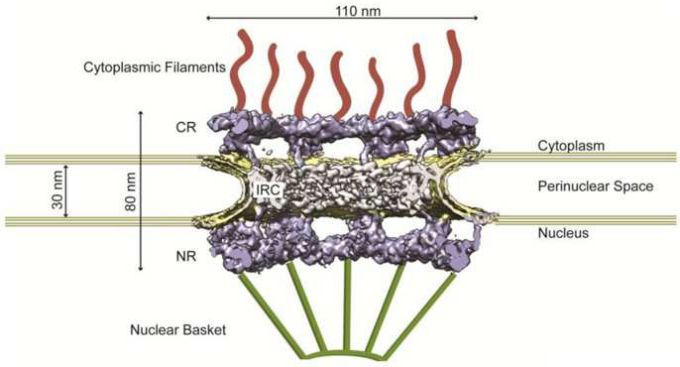

Figure 7. Overview of the nuclear pore complex embedded in the nuclear envelope (Schwartz 2016).

The NPCs are known to have non-canonical functions apart from nuclear transport based on their association with a number of cellular structures in the cytoplasm and the nucleus. The nuclear basket is involved in maintaining chromatin stability and handling, transcription coupled mRNA export, DNA repair, and gene regulation (Akhtar and Gasser 2007, Towbin, Meister et al. 2009, Nakano, Funasaka et al. 2010). The cytoplasmic filaments, on the other hand are linked to protein synthesis (Stewart 2007, Joseph and Dasso 2008).

To fully understand the relationship between NPC organization and nuclear function, it is essential to understand how this macromolecular structure is assembled. In metazoans, NPC assembly is cell cycle regulated and occurs during interphase as well as at the end of mitosis. Both these pathways are distinct from each other as biogenesis during interphase occurs in an intact nuclear envelope, whereas the NPCs are reassembled into the newly forming NE at the end of mitosis (Anderson and Hetzer 2007, Dultz and Ellenberg 2010). Studies have demonstrated that the post-mitotic pathway occurs by radial dilation of membrane openings. In contrast, interphase pathway requires fusion of the outer and inner nuclear membranes (Otsuka, Bui et al. 2016, Otsuka, Steyer et al. 2018). Lower eukaryotes, such as certain fungi like *S. cerevisiae* and *S. pombe* yeast, undergo closed mitosis, therefore NPC assembly only takes place via the interphase pathway.

1.3.2 Post-mitotic pathway

Towards the end of anaphase, membranes of the ER start to flatten on the chromatin to start the reformation of the nuclear envelope. Consequently, the NPCs start reassembly from subcomplexes on the newly forming nuclear envelope. It has been reported that the nucleoporin ELYS associates with the decondensed chromatin and triggers the assembly process (Galy, Askjaer et al. 2006, Rasala, Orjalo et al. 2006, Franz, Walczak et al. 2007).

ELYS further recruits the Nup107-Nup106 complex and the transmembrane nucleoporins Ndc1 and Pom121. Subsequently, the Nup93 complex is integrated in a step-by-step process, starting with the binding of the nucleoporin Nup53 to Ndc1, followed by the recruitment of Nup155 and Nup93. Nup62 complex is then recruited via Nup93, made up of FG-nucleoporins Nup62, Nup58 and Nup54. Lastly, the nuclear basket and the nuclear filaments are recruited to give rise to a mature functional NPC (Hawryluk-Gara, Shibuya et al. 2005, Dultz, Zanin et al. 2008, Vollmer, Schooley et al. 2012, Eisenhardt, Redolfi et al. 2014). The post-mitotic pathway supports the formation of ~2000 NPCs in about 3 minutes and the whole assembly process is completed in about 15-20 minutes (Otsuka, Steyer et al. 2018, Otsuka, Tempkin et al. 2023).

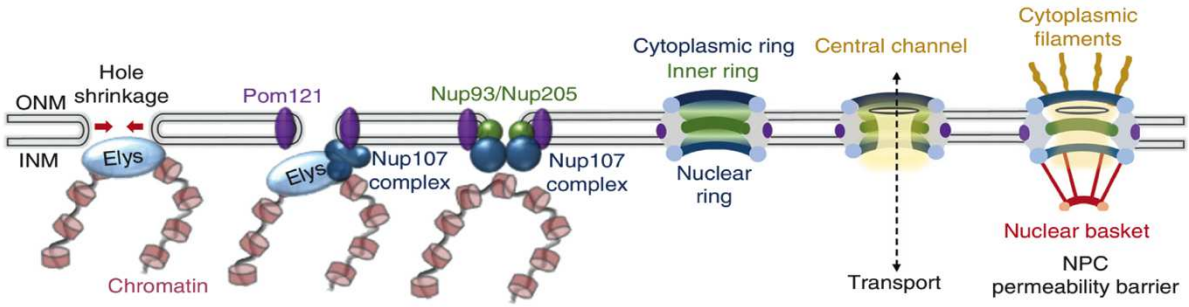

Figure 8. Schematic showing steps involved in the post-mitotic NPC assembly pathway (Raices and D'Angelo 2022).

1.3.3 Interphase pathway

During interphase, as the nucleus grows, NPCs continue to be assembled to maintain homeostasis for the next cell division. Organisms who undergo closed mitosis, like budding yeast, only utilize the interphase pathway for NPC biogenesis. Interphase assembly is slower compared to post-mitotic assembly, as it takes about 40-60 minutes (Otsuka, Tempkin et al. 2023), it is more sporadic and requires formation of a new discontinuity in the nuclear envelope. The most widely accepted model for interphase assembly describes an inside-out mechanism of membrane fusion. The initial step is the formation of a "pre-NPC" underneath the inner nuclear membrane. Insertion of this pre-NPC into the inner nuclear membrane leads to evagination of the INM towards the ONM, resulting in their fusion (Otsuka, Bui et al. 2016, Weberruss and Antonin 2016). Deformation of the membranes for fusion requires concerted actions of curved membrane binding proteins, amphipathic helices, and/or conical lipids (Antonin, Ellenberg et al. 2008, Rothballer and Kutay 2013). This model is supported by findings that show that Nup133, by virtue of its curvature-sensing domain, is required only for interphase assembly. Additionally, Pom121 which is a transmembrane nucleoporin has

a role specifically in interphase assembly, as it depletion disrupts the recruitment of the Nup107/160 complex (Doucet, Talamas et al. 2010, Funakoshi, Clever et al. 2011, Talamas and Hetzer 2011). A similar role has been proposed for Nup153, which binds to the inner nuclear membrane leading to the recruitment of the Y-complex (Vollmer, Lorenz et al. 2015). A recent study has shown that in vertebrates, the initiation of assembly starts with the recruitment of transmembrane Nups like Pom121 at the INM, proceeded by components of the nuclear basket like Nup153 and Tpr. Outer and inner ring Nups then assemble later (Otsuka, Tempkin et al. 2023). In yeast cells however, outer and inner ring Nups assemble during early stages of assembly, and the basket components come later (Onischenko, Noor et al. 2020).

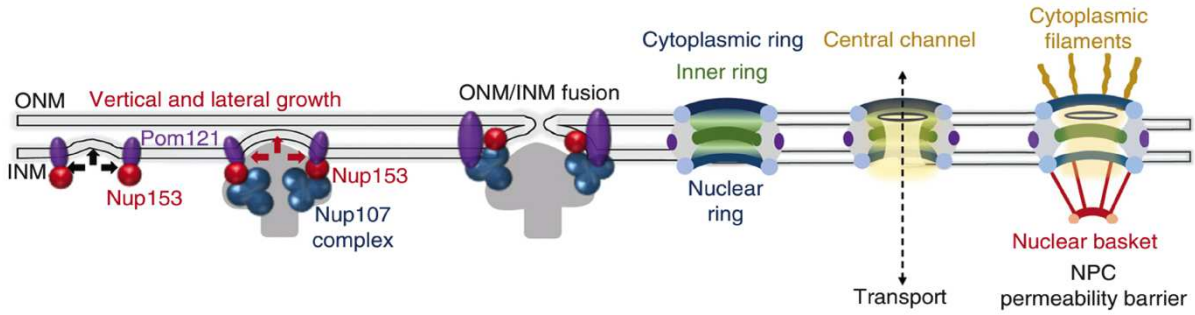

Figure 9. Interphase or *de novo* NPC assembly pathway (Raices and D'Angelo 2022).

1.3.4 Membrane remodeling during interphase assembly

It is clear that NPC biogenesis requires extensive membrane remodeling so that the INM and ONM can fuse. Membrane remodeling events are a part of normal cellular physiology, however in the case of NPCs it requires long-term stabilization as NPCs are very stable and long-lived structures. Some of the factors that make membrane deformations not only possible but also stable are transmembrane proteins, amphipathic helices, reticulons, scaffold Nups, GLFG repeats and lipids. They are discussed in detail below.

Lipids and their physical nature are a major factor contributing to membrane deformations. These membranes are made up of a bilayer of lipids which contain a head group, fatty acid tails and a backbone (van Meer, Voelker et al. 2008, van Meer and de Kroon 2011). The shape of the lipids and the saturation level of their fatty acid tails play a major role in determining the level of membrane packing (Figure 10A-B) (Drin and Antonny 2010, Shen, Pirruccello et al. 2012, Antonny, Vanni et al. 2015). Packing defects impact the ability of membrane deforming proteins, such as amphipathic helices, to access the bilayer.

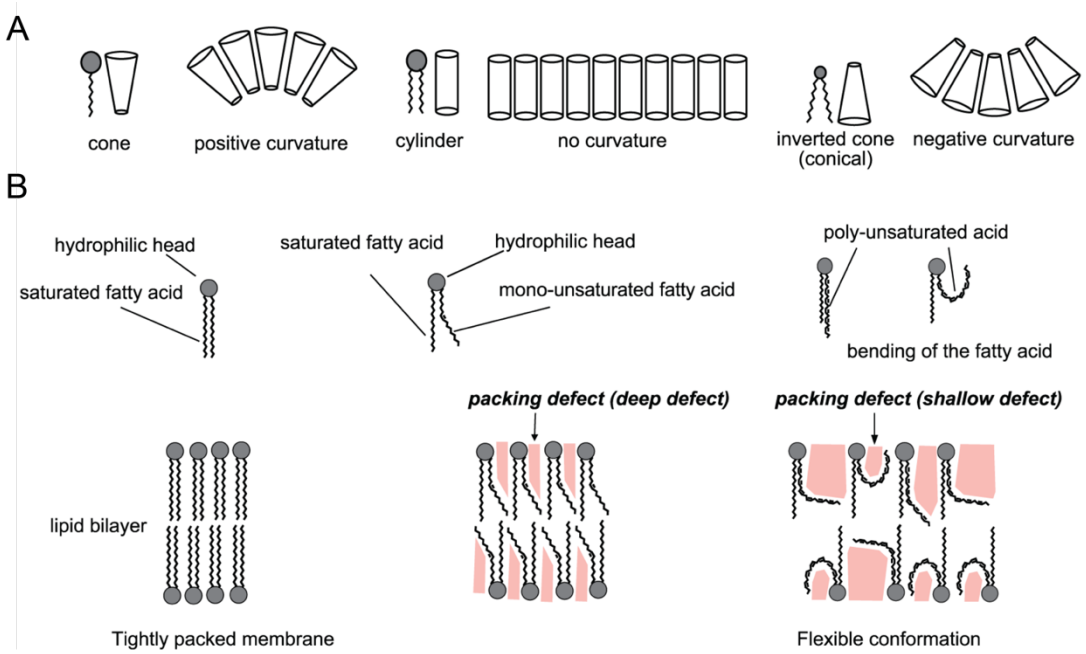

Figure 10. Illustration of how the shape and level of saturation of lipids impacts lipid packing and ultimately membrane curvature (Kitamata, Inaba et al. 2020).

Selective transfer of lipids between the leaflets of the bilayer has also been implicated in curvature induction (Farge and Devaux 1992, Farge, Ojcius et al. 1999). One such example is cholesterol which has a role in formation of high-curvature clathrin-coated buds (Subtil, Gaidarov et al. 1999). It does so by potentially translocating to the budding face of the bilayer and bending the membrane (Figure 11).

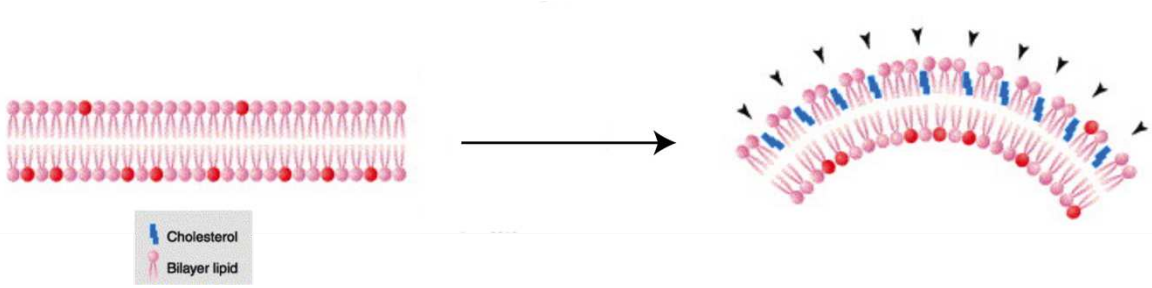

Figure 11. Integration of cholesterol molecules in the lipid bilayer decreases membrane rigidity and assists in membrane bending (Farsad and Camilli 2003).

As mentioned before, a number of membrane deforming proteins interact with the bilayer. The lipid headgroups by virtue of their charge are able to bind to membrane deforming proteins. The fatty acid tails are accessible to amphipathic helices which are found buried in the bilayer and thus prone to deformation.

Amphipathic helices are regions of proteins that fold into a helical structure when they come in contact with a polar/non-polar surface and are present in a number of stably folded proteins. These helices present a hydrophobic face and a polar face. This feature allows the helix to lay down parallel to the membranes and anchor the proteins. Studies

have revealed that amphipathic helices also have a role in sensing membrane curvature (Drin, Casella et al. 2007) and membrane remodeling (Gallop, Jao et al. 2006, Masuda, Takeda et al. 2006). One hypothesis that explains how amphipathic helices might be able to deform membrane is the bilayer-couple hypothesis, according to which curvature can be induced in a membrane when there is relative increase in the surface area of one the leaflets of the bilayer (Sheetz, Painter et al. 1976). Compounds with amphipathic properties are able to intercalate into bilayer leaflets and deform them (Sheetz and Singer 1974).

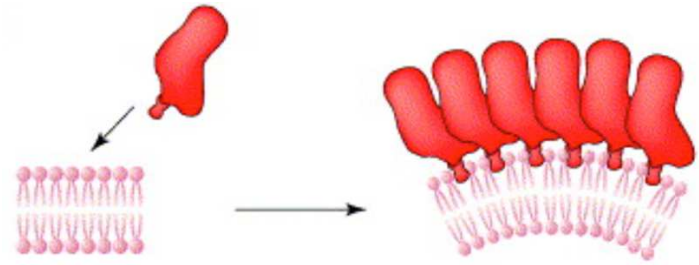

Figure 12. Membrane deformation by insertion of amphipathic helices into the bilayer (Farsad and Camilli 2003).

These amphipathic helices also have the ability to sense membrane curvature by exploiting lipid packing defects (Kitamata, Inaba et al. 2020, Pajtinka and Vácha 2024).

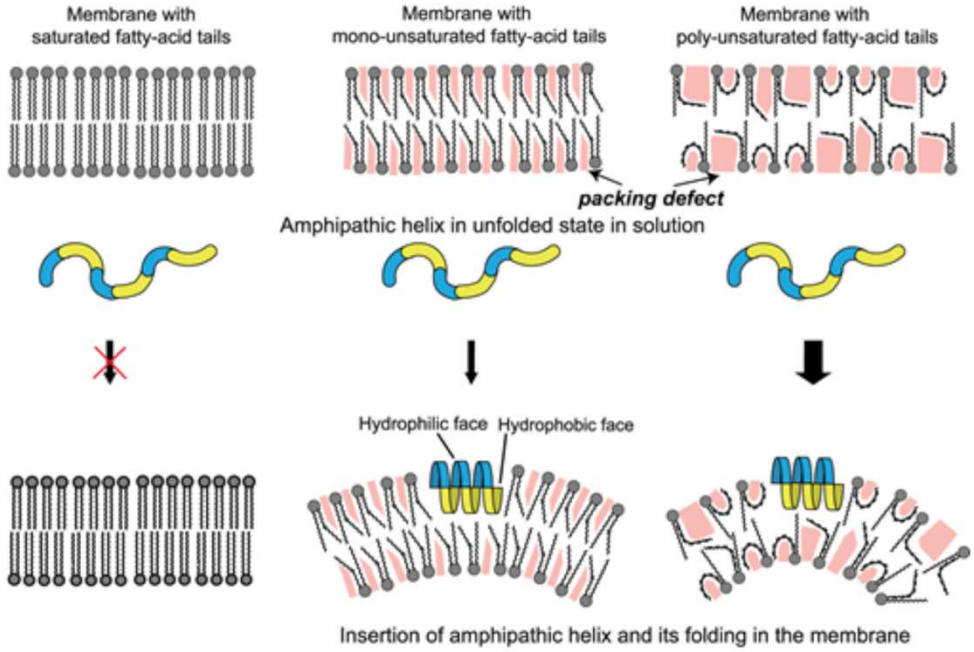

Figure 13. Impact of lipid packing on insertion of amphipathic helices and induction of membrane curvature (Kitamata, Inaba et al. 2020).

A number of nucleoporins contain amphipathic helices e.g., scNup60 and scNup1, and are reported to induce nuclear envelope deformation (Mészáros, Cibulka et al. 2015). A

metazoan ortholog of these two proteins, Nup153, also gives rise to a similar phenotype (Mészáros, Cibulka et al. 2015). In addition, certain amphipathic lipid packing sensor (ALPS) motifs in Nup120, Nup133 and Nup170 in budding yeast have been identified which can potentially deform as well as stabilize curved membranes (Stankunas and Köhler 2023).

Integral membrane proteins are important nucleoporins and are potential candidates for INM-ONM fusion. Ndc1 is one such protein. It is an essential gene and has a role in insertion of both the SPB and NPC into the nuclear envelope (Lau, Giddings et al. 2004). Pom121 is another transmembrane nucleoporin that is involved in early stages of biogenesis. SUN domain proteins, such as *SUN1*, interact with Pom121 to regulate assembly and distribution of NPCs in the nuclear envelope (Talamas and Hetzer 2011). SUN proteins have large luminal domains that have the potential to bridge the gap between the INM-ONM, thereby aiding fusion. Similarly, Heh1 and Heh2 are known to interact with transmembrane nucleoporins such as Nup152 via their luminal domains (Yewdell, Colombi et al. 2011).

Another set of related transmembrane proteins, Apq12, Brr6, and Brl1 have been implicated in NPC biogenesis. *BRR6* and *BRL1* are both essential genes. Temperature sensitive mutants revealed defects in assembly in the form of herniations (assembly intermediates with defects in membrane fusion), and changes in lipid composition (Lone, Atkinson et al. 2015, Zhang, Neuner et al. 2018). They interact with the non-essential *APQ12* to regulate lipid homeostasis for the biogenesis to occur (Scarcelli, Hodge et al. 2007).

Scaffold Nups form the core of the NPC and consists of the outer and inner rings. Research has shown that these scaffold Nups are made up of β-propellers and α-solenoid-like folds (Brohawn, Leksa et al. 2008). The Y-complex, which is composed of 7 core scaffold Nups, is one such example. Research has shown that that clathrin/adaptin complexes, COPI complexes, COPII complexes, and the Y-complex exhibit a shared molecular architecture (Devos, Dokudovskaya et al. 2004, Brohawn, Leksa et al. 2008, DeGrasse, DuBois et al. 2009). This similarity may have originated through a divergent evolutionary pathway as both vesicle coating proteins and scaffold Nups are involved in membrane bending and stabilizing functions. Moreover, the Y-complex also includes known members of the vesicle coat complex like Sec13 and Seh1 (Devos, Dokudovskaya et al. 2004).

FG repeats containing nucleoporins also have an important role in stabilization of the NPC. GLFG Nups have been shown to interact directly with a number of scaffold Nups. Additionally, they have a critical role in stabilizing interactions within the NPC scaffold (Shulga and Goldfarb 2003, Onischenko, Tang et al. 2017). Nup188 and Nup116 via its GLFG repeats, have been shown to act in a redundant manner to bridge the symmetrical core and cytoplasmic components of the NPC (Onischenko, Tang et al. 2017). This interaction is vital in completing the assembly process.

Reticulons represent a broad and varied collection of membrane-associated proteins present across the eukaryotic kingdom. Each member of this family features a carboxy-terminal reticulon homology domain characterized by two hydrophobic regions flanking a hydrophilic loop spanning 60-70 amino acids (Oertle, Klinger et al. 2003). Reticulons primarily localize to the endoplasmic reticulum, and there is evidence suggesting their involvement in processes such as endoplasmic reticulum-Golgi trafficking, vesicle formation, and membrane morphogenesis (Voeltz, Prinz et al. 2006). Deletion of *RTN1* and *YOP1* results in formation of cluster of NPC like structures (Dawson, Lazarus et al. 2009). Moreover, Rtn1/Yop1 have been shown to interact with the Y-complex, linker Nups and Poms, indicating a role of these membrane deforming proteins in stability of the membrane during biogenesis. Similarly, *LNP1* (implicated in regulation of the structure of ER tubules) deletion in combination with *RTN1* deletion is known to cause NPC clustering. Furthermore, *LNP1* shows genetic interactions with nucleoporins that have association with the ER as well, for example, *POM33*, *PER33*, and members of the Y-complex, pointing towards a role of Lnp1 in stabilizing new nuclear pores (Casey, Chen et al. 2015).

1.3.5 The spindle pole body

The spindle pole body (SPB) is the microtubule organizing center (MTOC) in fungi. It is the functional equivalent of the centrosome in animals. The primary function of the microtubule organizing center is nucleation of microtubules, which give rise to the mitotic spindle. The mitotic spindle facilitates the segregation of chromosomes during mitosis and meiosis.

The budding yeast SPB is embedded in the nuclear envelope and appears as a layered cylindrical structure (Byers and Goetsch 1975, O'Toole, Winey et al. 1999). It consists of ~18 proteins, which give rise to a structure that is 150 nm in height and 80-160 nm in diameter (Jaspersen and Winey 2004). There are 3 main structural components, the

outer plaque, the inner plaque and the central plaque. The outer plaque, which is located on the cytoplasmic face, nucleates cytoplasmic microtubules. Facing the nucleoplasm is the inner plaque, and it nucleates nuclear microtubules. The central plaque embeds the SPB as it spans the nuclear envelope (Robinow and Marak 1966, Moens and Rapport 1971, Byers and Goetsch 1975). Two additional layers have also been described, called the intermediate layer 1 (IL1) and intermediate layer (IL2), both located between the outer and the central plaques. Another structure associated with the SPB is the half bridge. It is also a multi layered electron dense region next to the SPB (Adams and Kilmartin 1999). It is essentially an extension of the central plaque, and the site where the new SPB assembles. It also has a role in nucleation of cytoplasmic microtubules (Jaspersen and Winey 2004).

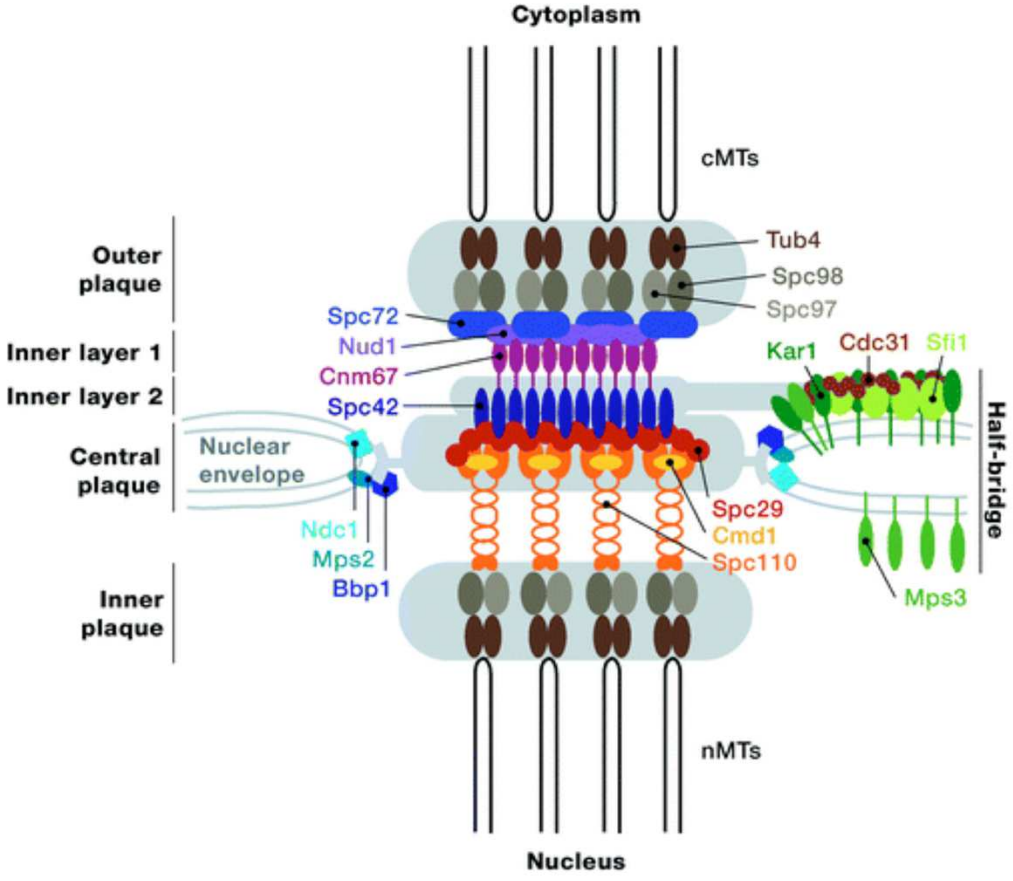

Figure 14. Structure of the *S. cerevisiae* spindle pole body (Jaspersen and Winey 2004).

The budding yeast spindle pole body is composed of ~18 proteins. Spc42 is the main component of the central plaque (Bullitt, Rout et al. 1997). It interacts with Spc29 (central core component) and the C-terminus of Spc110 (an inner plaque protein) via its N-terminus (Adams and Kilmartin 1999, Elliott, Knop et al. 1999). Spc110 binds to calmodulin (Cmd1) which is involved in regulating Spc29 and Spc110 interactions. Spc42

also interacts with the C-terminus of Cnm67, a protein implicated in maintaining the spacing between the IL1 and IL2 (Schaerer, Morgan et al. 2001, Muller, Snydsman et al. 2005). Cnm67 binds to the outer plaque protein Nud1 via its N-terminus which in turn recruits Spc72 (Gruneberg, Campbell et al. 2000). In order to associate with the microtubules (MTs), the SPB interacts with the γ-tubulin complex, composed of Spc97, Spc98 and Tub4, which is recruited to the SPB via Spc72 and Spc110 (Knop, Pereira et al. 1997, Knop and Schiebel 1997, Sundberg and Davis 1997).

2. Aims

Nuclear pore complexes (NPCs) are conserved assemblies in eukaryotic cells that facilitate transport of macromolecules across the nuclear envelope (NE). Through distinct mechanisms, NPCs assemble at the end of mitosis and during interphase. Interphase NPC assembly starts with the deposition of NPC proteins (Nups) on the nuclear side of the inner nuclear envelope (INM), followed by its deformation towards the outer nuclear membrane (ONM). Subsequently, INM and ONM fuse by an unclear mechanism.

In this study I will address how the two nuclear membranes fuse during the interphase pathway. I will use *S. cerevisiae* (budding yeast) as a model organism as NPC assembly in budding yeast only follows the interphase pathway making it an ideal model for this study. Previous data suggests that three interacting integral membrane proteins, Apq12 and the paralogues Brl1 and Brr6, promote NE fusion during NPC assembly in organisms with closed mitosis (Tamm, Grallert et al. 2011, Zhang, Neuner et al. 2018). Brl1 localizes preferentially to the INM, whereas Brr6 and Apq12 are enriched at both the INM and ONM. Importantly, Apq12, Brl1 and Brr6 interact and transiently associate with NPC assembly intermediates. *apq12Δ* and conditional *brl1* and *brr6* mutants start NPC biogenesis by depositing Nups at the INM but NE fusion fails, yielding INM deformations called herniations. These are structurally similar to herniations in *nup116Δ* cells, which arise because Nup116 has a scaffolding function during NPC assembly (Allegretti, Zimmerli et al. 2020). Interestingly, *BRL1* overexpression completely rescues the NE fusion defect in *nup116Δ* cells (Zhang, Neuner et al. 2018), indicating that Brl1 functions in the NE fusion process downstream of *NUP116*.

So, in this study, I will focus on functional characterization of Apq12, Brl1 and Brr6. Further I will analyze the role of these three proteins in regulating the integrity of the nuclear envelope. Finally, the function of the Apq12, Brl1, and Brr6 module during interphase NPC assembly, particularly their amphipathic helices in facilitating the fusion of the INM and ONM will be investigated.

This study aims to elucidate the functional mechanisms of Apq12, Brl1, and Brr6, particularly their amphipathic helices, and their contribution to a more complete understanding of INM-ONM fusion during interphase NPC assembly.

3. Results

Part of the following results are published in Zhang, Khan et al. 2021 and Vitale, Khan et al. 2022. Acquisition and processing of all electron microscopy data was done by Dr. Annett Neuner. Float-up assays and MST analysis were done in collaboration with Dr. Kerstin Rink from Prof. Dr. Thomas Söllner's lab in BZH. Lipid mass spectrometry was done by Prof. Dr. Britta Brügger's lab in BZH.

"A short perinuclear amphipathic α-helix in Apq12 promotes nuclear pore complex biogenesis" - (Zhang, Khan et al. 2021)

3.1 Functional characterization of Apq12

Apq12 is a transmembrane protein carrying two transmembrane domains; TM1 and TM2 (Figure 15A). To dissect the molecular role of Apq12 in NPC biogenesis, functional characterization of Apq12 subdomains was performed. The AmphipaSeek program predicted the presence of an amphipathic helix (AαH) between the two transmembrane domains of Apq12 (Figure 15A-B). The helix exhibits distinct characters, with two positively charged amino acids (Lysine & Arginine) present on the hydrophilic face and hydrophobic residues on the opposite side of the helix (Figure 15B).

The hydrophobic amino acids present in the amphipathic helix (Figure 15B, yellow) have the ability to interact with lipids carrying aliphatic chains, whereas the hydrophilic residues (Figure 15B, blue) interact with polar-apolar lipids. Consistent with these facts, it was observed that a synthetic Apq12 peptide (AαH), labelled with Atto488 was able to bind to giant unilamellar vesicles (GUVs) of 1-10 μm diameter (Figure 15C). I also introduced mutations in the amphipathic helix to disrupt its hydrophobic moment, from 0.595 to 0.054. The Atto488 labelled mutant peptide (AαH-m) was unable to bind to GUVs, as was the Atto488 dye used as a control (Figure 15C).

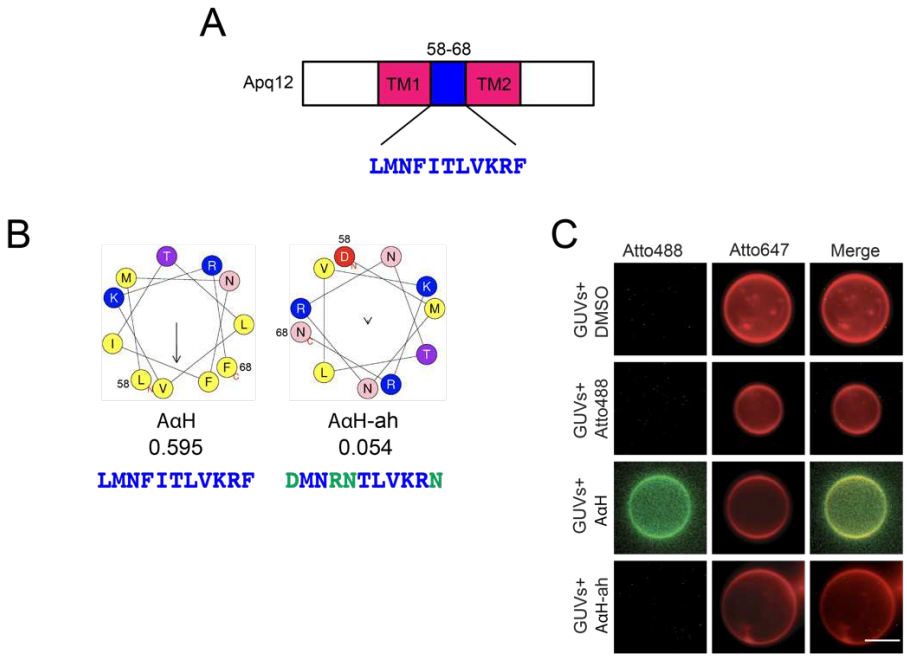

Figure 15. Apq12 contains an amphipathic helix. **(A)** Domain organization of Apq12. The two transmembrane domains, TM1 and TM2, and an amphipathic helix, AαH, are indicated. **(B)** HeliQuest prediction of AαH and AαH-ah along with their hydrophobic moments. Mutated amino acids in AαH-ah are indicated in green. **(C)** In vitro binding of Atto647 labelled GUVs to Atto488 labelled synthetic AαH and AαH-ah peptides. Atto488 dye and DMSO are used as controls. Scale bar: 5 μm.

Figure taken and adapted from (Zhang, Khan et al. 2021).

To further analyze the binding efficiency of the AαH peptide, small unilamellar vesicles (SUVs; 80-120 nm diameter) were used. Bound peptide was separated from unbound peptide using a nycodenz gradient. It was also observed that the AαH peptide showed a higher binding efficiency to nuclear envelope (NE) derived SUVs compared to plasma membrane (PM) derived SUVs (Figure 15A). The AαH-ah peptide and the Atto488 dye were not able to bind to the SUVs. Similarly, the peptide alone was not able to float through the gradient (Figure 16A).

Further quantification of the binding of AαH peptide with the SUVs was done using microscale thermophoresis (MST) (Figure 16B). The AαH peptide bound the NE-lipid derived SUVs with a K_D of 16 ± 0.91 μM. The decrease in binding of the AαH peptide to PM-lipids derived SUVs was indicated by an increased K_D of 58.9 ± 5.35 μM. Consistent with previous results, the AαH-ah peptide failed to bind the SUVs with a measurable K_D. The results suggest that Apq12 AαH is membrane active and its binding to liposomes depends on its amphipathic nature, as well as the lipid composition of the liposomes.

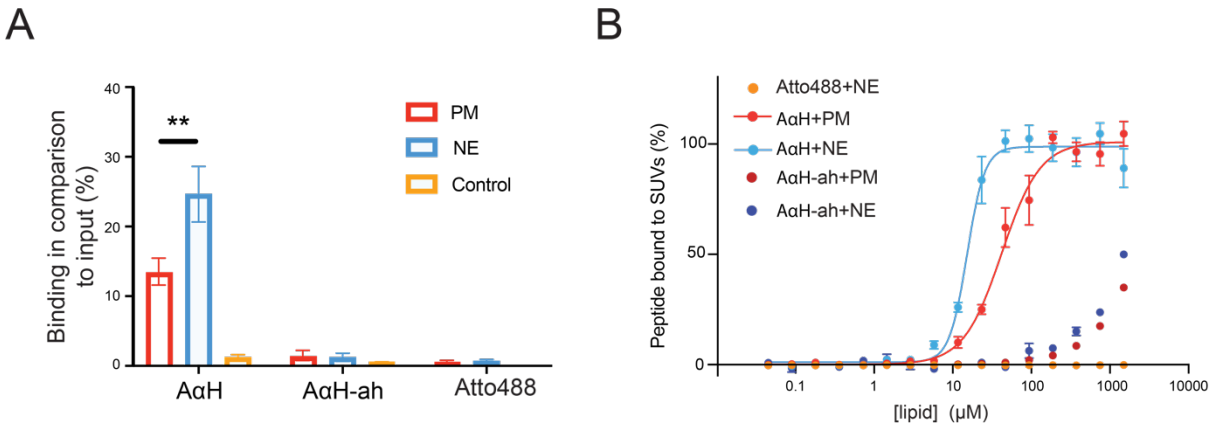

Figure 16. MST measurements. **(A)** The binding of liposomes to AαH and AαH-ah peptides was measured in float-up assay by comparing to the input. n=3. **(B)** Liposomes of different compositions were titrated against AαH and AαH-ah labelled with Atto0488 dye and Atto488 dye alone as a control. K_D value of the interaction was calculated after normalizing the data to the amount of bound peptide using the Hill equation. n=3. Values are presented as means ± s.e.m. **p<0.01.

Figure taken and adapted from (Zhang, Khan et al. 2021).

3.2 Subcellular localization and topological analysis of Apq12

Next, I wanted to analyze, whether the AαH is important for the function of Apq12. Because *apq12Δ* mutants have a cold sensitive growth defect (Scarcelli, Hodge et al. 2007), I tested *APQ12*, *apq12Δ and apq12-ah* (Figure 15B) for temperature dependent growth defects. Similar to *apq12Δ*, *apq12-ah* failed to grow at 16˚C, and showed restricted growth at 23˚C (Figure 17A). These results show that the integrity of the amphipathic helix is important for proper growth at lower temperatures.

Further, I analyzed if the subcellular localization of Apq12 is dependent on its amphipathic helix. yeGFP tagged Apq12 localized to the nuclear envelope and the peripheral endoplasmic reticulum (ER) (Figure 17B), consistent with previous data (Lone, Atkinson et al. 2015). Notably, *apq12-ah* also displayed a similar localization pattern (Figure 17B). Thus, it can be concluded that the AαH is not necessary for the subcellular localization of Apq12. In addition, immuno-electron microscopy (EM) was performed using anti-GFP antibodies to take a deeper look into the localization patterns. Interestingly, in addition to confirming the NE/ER localization of Apq12 and Apq12-ah (Figure 17C), it showed that Apq12 and Apq12-ah only associated with a subset of NPCs, 10% and 15% respectively (Figure 17D). This may point to a transient interaction between Apq12 and assembling NPCs.

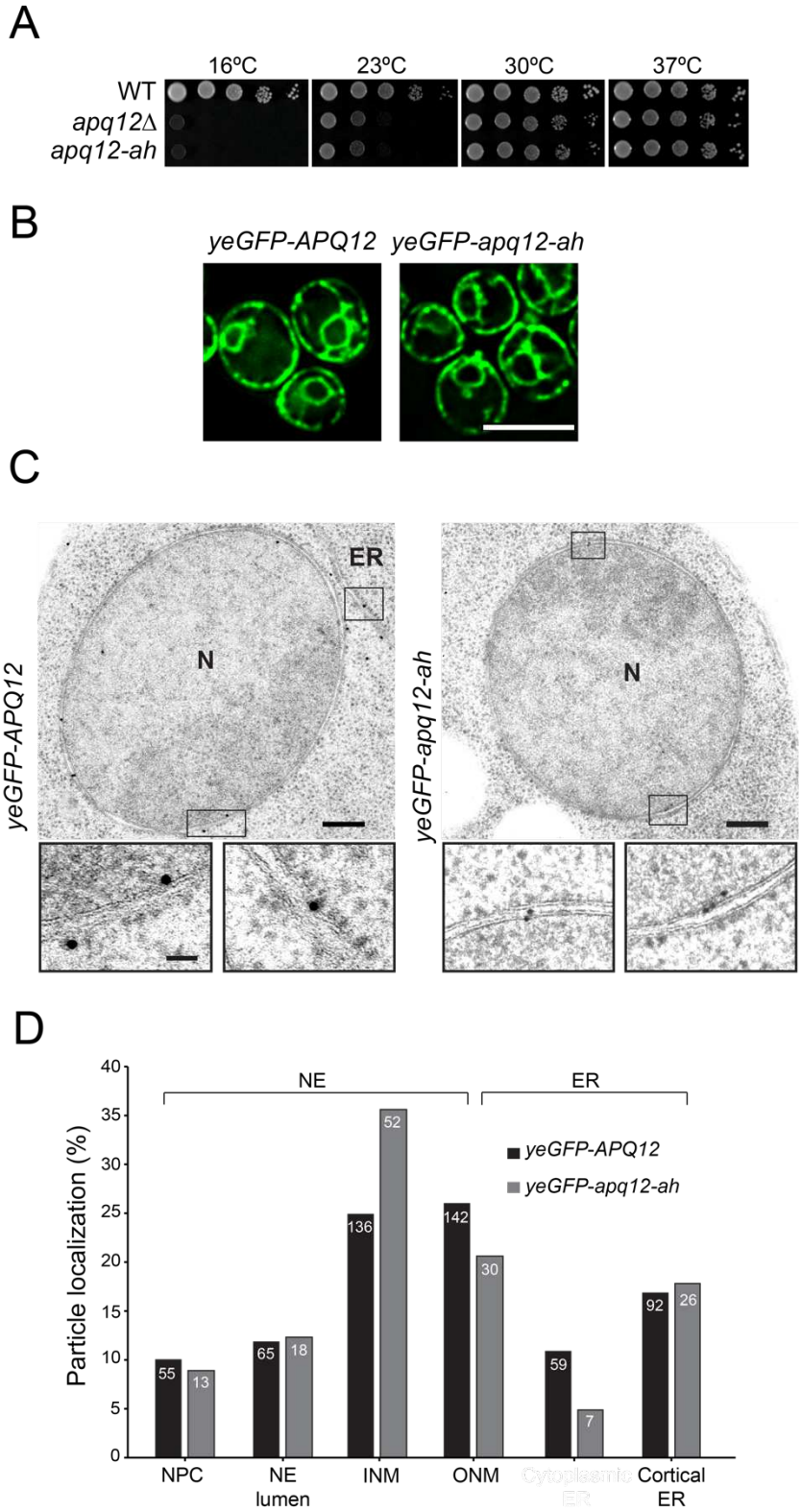

Figure 17. Apq12 localizes to the NE and ER. **(A)** Growth test of *APQ12, apq12Δ,* and *apq12-ah* on YPD plates. Incubation was done at the indicated temperatures. **(B)** Fluorescence microscopy images of yeGFP-Apq12 and yeGFP-Apq12-ah carrying cells. Scale bar: 5 μm. **(C)** Immuno-EM images of yeGFP-Apq12 and yeGFP-Apq12-ah carrying cells. 10 nm gold particles were used. Rectangles indicate the enlargements. N, nucleus; ER, endoplasmic reticulum. Scale bar: 200 nm & 50 nm (enlargements). **(D)** Quantification of data from (C). Number of gold particles analyzed is indicated. NE, nuclear envelope.

Figure taken and adapted from (Zhang, Khan et al. 2021).

To understand the topology of Apq12 comprehensively, and whether the AαH has a role in maintaining this topology, I used two approaches. In the first approach, I took advantage of the split-GFP system (Smoyer, Katta et al. 2016). The split-GFP system, as the name indicates, splits the GFP into two fragments, which can be fused with the proteins of interest. Functional GFP is only reconstituted when the two fragments, or the proteins of interest have an overlapping localization. Co-expression of Apq12-GFP_{1-10} and GFP_{1-10}-Apq12 with ER and ONM localized GFP_{11}-mCherry-Scs2TM resulted in reconstitution of GFP as can be seen by the NE and cortical ER staining (Figure 18A). Similarly, co-expression with nuclear GFP_{11}-mCherry-Pus1 also restored GFP at the NE (Figure 18A). No GFP signal was seen when Mps3-GFP_{1-10} was co-expressed with GFP_{11}-mCherry-Scs2TM and GFP_{11}-mCherry-Pus1, consistent with the fact that the C-terminus of Mps3 is located in the perinuclear space. These data indicate that the N and C-termini of Apq12 are facing either the cytoplasm or the nucleoplasm depending on ER/ONM or INM localization of Apq12 respectively. Similar results were obtained for Apq12-ah (Figure 18A).

In the second approach, I used the biotinylation of the N and C-termini of Apq12 with the histidine-biotin-histidine (HBH) tag by biotin ligases. Biotin ligases are not present in the perinuclear space. Both the N and C-termini of Apq12 of Apq12-ah showed biotinylation confirming their cytoplasmic and nucleoplasmic localization (Figure 18B). Pom152, that carries a perinuclear C-terminus showed biotinylation only at the N-terminus.

These findings give conclusive evidence that the N and C-termini of Apq12 are located in the cytosol and the nucleoplasm, whereas the AαH lies in the perinuclear space bridging the two TMs (Figure 18C).

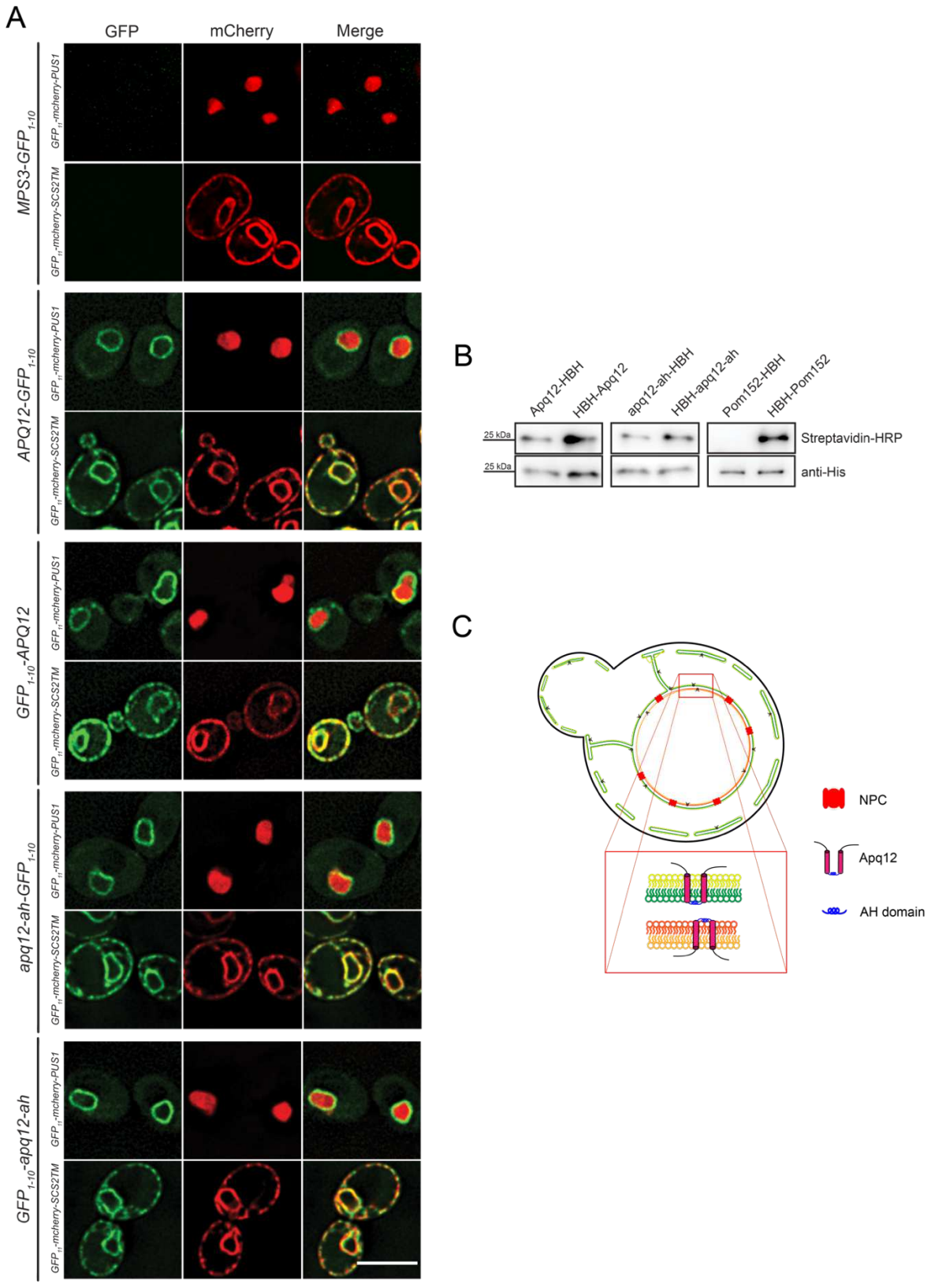

Figure 18. Apq12 AαH is located in the perinuclear space. **(A)** Images of strains carrying GFP_{1-10} tagged Apq12 and Apq12-ah and ONM/ER (GFP11-mCherry-Scs2TM) and nuclear (GFP_{11}-mCherry-Pus1) reporters. Mps3-GFP_{1-10} is used as a negative control. Scale bar: 5 μm. **(B)** Western blot of analysis of in vivo biotinylation of the indicated strains. Pom152 is used as a control. **(C)** Model of Apq12 localization and topology.

Figure taken and adapted from (Zhang, Khan et al. 2021).

3.3 Role of Apq12 AαH in regulating NE integrity, NPC biogenesis and lipid homeostasis

To understand the effects of the loss of Apq12 on the NE and the NPCs, EM was performed on wildtype, *apq12Δ*, and *apq12-ah* mutants. Results showed that at 37˚C *apq12Δ* and *apq12-ah* mutants had accumulated herniations (Figure 19B-E). NE invaginations appeared as a major phenotype at 23˚C, whereas herniations, NE breakdown and invaginations were frequent at 16˚C (Figure 19B-E). This NE rupture can explain why *apq12Δ* and *apq12-ah* mutants are lethal at 16˚C. In contrast, *APQ12* wildtype cells displayed intact spherical nuclei (Figure 19A).

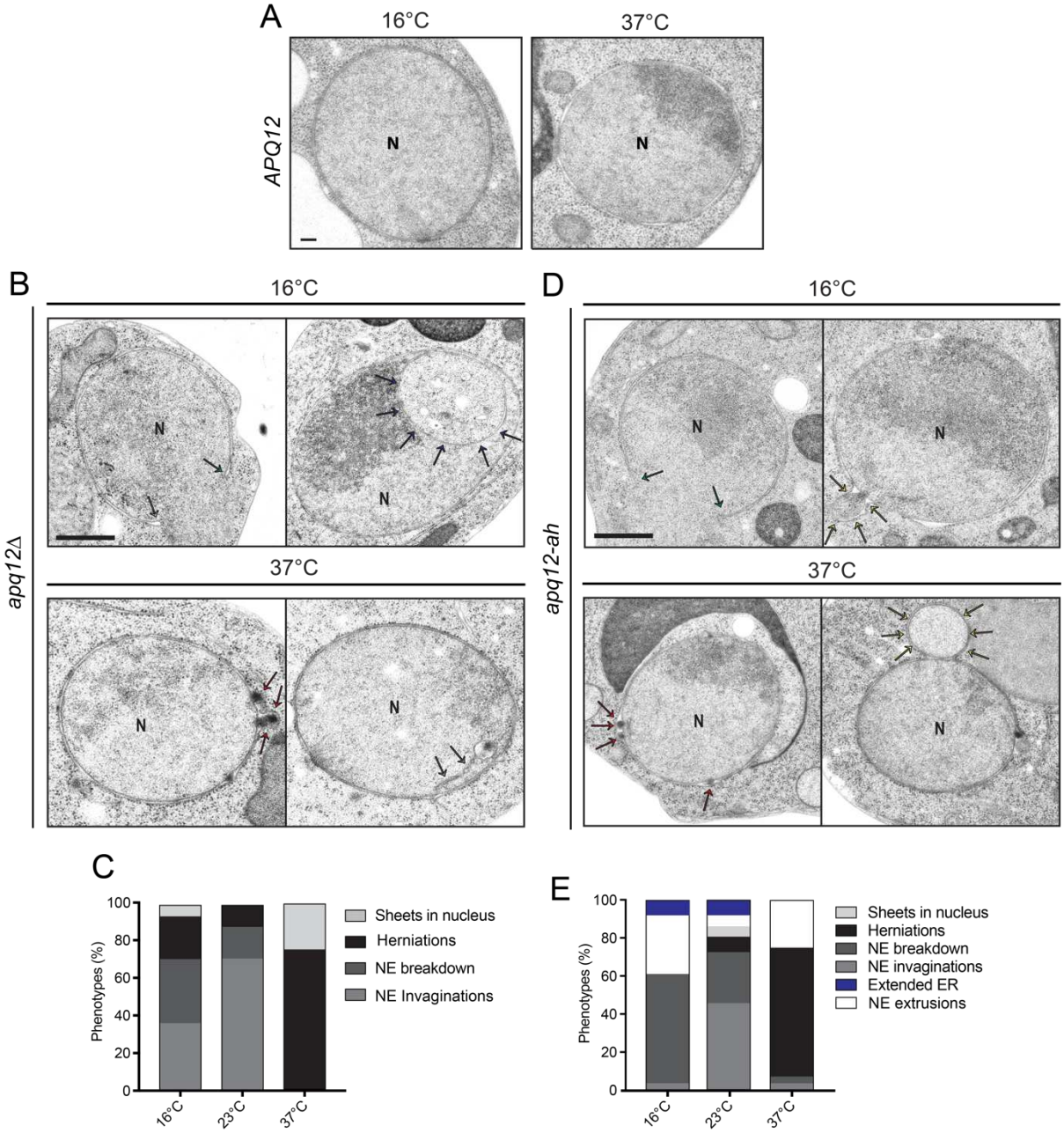

Figure 19. Phenotypic analysis of *apq12Δ* and *apq12-ah* mutants. **(A)** EM images of WT *APQ12* cells grown at indicated temperatures. Scale bar: 100 nm. **(B)** Electron micrographs of *apq12Δ* mutants. Arrows indicate the color-coded phenotype. Scale bar: 500 nm. **(C)** Quantification of data from (B). n=57/37˚C, 40/23˚C, 44/16˚C. **(D)** Electron micrographs of *apq12-ah* mutants at indicated temperatures. Scale bar: 500 nm. **(E)** Quantification of data from (D). n=28/37˚C, 39/23˚C, 27/16˚C. N, nucleus.

Figure taken and adapted from (Zhang, Khan et al. 2021).

Previous research has implicated Apq12 in lipid homeostasis (Tamm, Grallert et al. 2011) which can explain the NE and NPC defects in Apq12 mutants. I therefore performed lipid mass spectrometry in collaboration with Prof. Britta Brügger, BZH, to investigate how the lipid content and composition in *apq12Δ* and *apq12-ah* mutants change in response to different temperatures in comparison to the wildtype. Results indicated that in both

apq12Δ, and *apq12-ah* mutants, there was a shift in lipid composition from membrane lipids to storage lipids relative to the wildtype (Figure 20A-B). Moreover, there was an increase in saturated lipids as is evident from the decrease in the number of double bonds and increase in chain length (Figure 20C-D), causing decreased membrane fluidity and therefore explaining the NE breakdown at lower temperatures in *apq12Δ* and *apq12-ah* mutants.

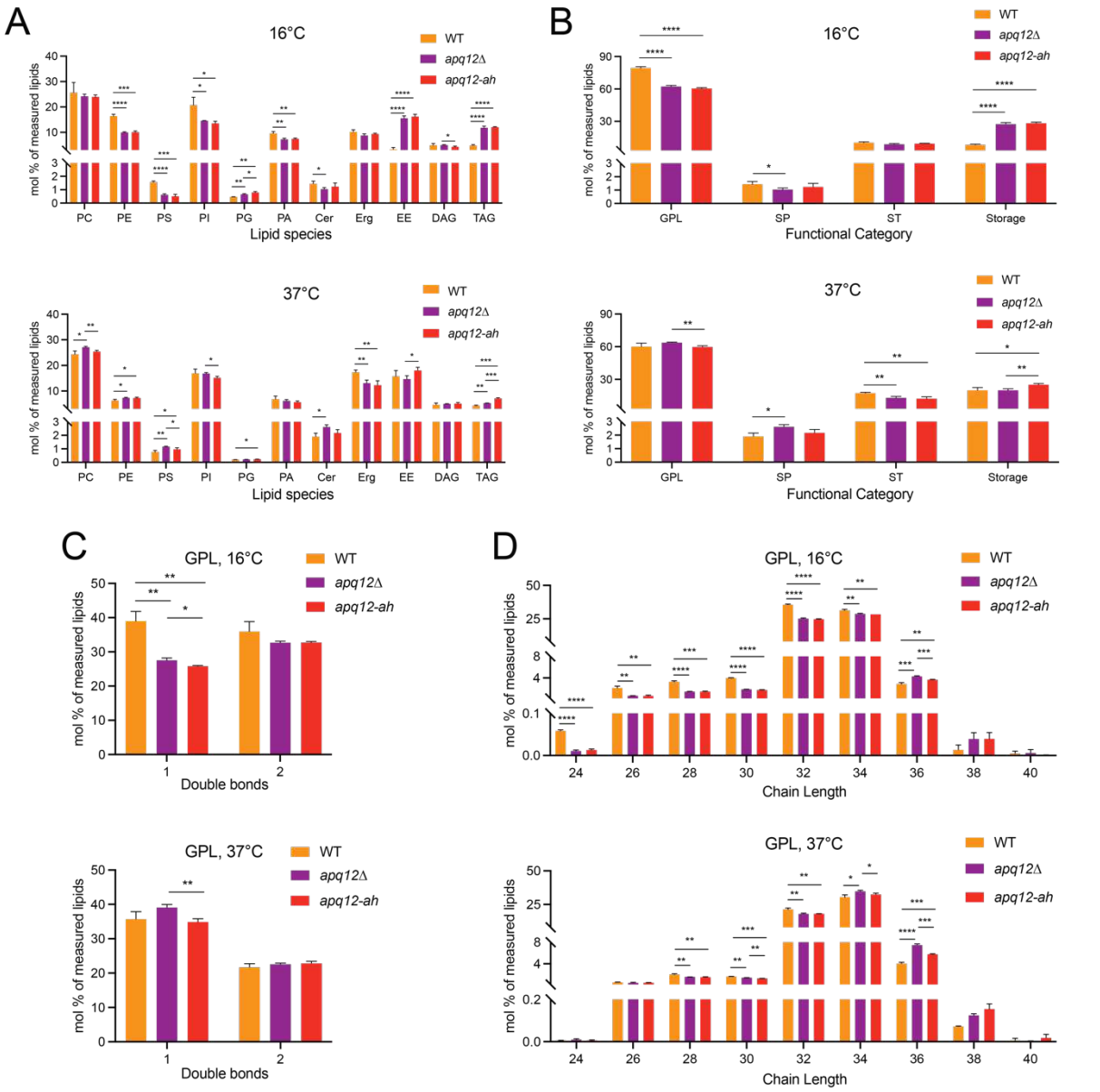

Figure 20. Lipid analysis of *APQ12*, *apq12Δ* and *apq12-ah* cells incubated at 16˚C and 37˚C for 18 and 2 hours, respectively. **(A)** Graphs showing lipid species in mol% of measured lipids. **(B)** Plots of functional categories of lipids; glycerophospholipids and glycerolipids (GPL), sphingolipids (SP), sterols (ST), and storage lipids. **(C)** Graphs showing the number of double bonds in GPL. **(D)** Plots showing GPL chain lengths. n=3. Values are presented as means ± SD. *p<0.05, **p<0.01, ***p<0.001, ****p<0.0001.

Figure taken and adapted from (Zhang, Khan et al. 2021).

3.4 Over-expression of *APQ12* disrupts the localization of ER proteins and NPC biogenesis factors

To further understand the function of Apq12, I over-expressed it under the galactose inducible *GAL1* promoter. Growth analysis showed that overexpression of *APQ12* was toxic for cells, as cells failed to grow on galactose medium (Figure 21A). Over-expression of other integral membrane proteins such as *BRL1* and *BRR6* did not show such growth toxicity.

To look at the impact of this *APQ12* over-expression on the NE structure and function, I used yeast strains containing yeGFP tagged *BRL1* and *BRR6,* which are NPC biogenesis factors (Figure 21B). Before induction of over-expression of *APQ12*, the yeGFP signal from Brl1 and Brr6 showed uniform distribution along the NE and ER. Upon induction, it was seen that overexpression of Apq12 resulted in dense clustering of both Brl1 and Brr6 signal (Figure 21B-D). These clusters were devoid of NPCs, as can be seen by the overlay of Nup85-tdTomato and yeGFP-Brr6 and yeGFP-Brl1 and the line scans of yeGFP and tdTomato signals (Figure 21B-E). Control cells containing an empty vector, showed smooth NE staining with no clustering of the yeGFP-Brl1 and yeGFP-Brr6, before and after induction of expression.

I next analyzed Sec63-yeGFP and Ole1-yeGFP, NE/ER proteins, in response to *APQ12* over-expression. Similar to yeGFP-Brl1 and yeGFP-Brr6, the Sec63-yeGFP and Ole1-yeGFP signal clustered upon Apq12 over-expression (Figure 21F). Control cells however maintained the smooth distribution of both Sec63 and Ole1 signals.

Taken together, these results show that upon over-expression not only is Apq12 toxic, but it also impacts subcellular localization of NPC biogenesis factors; Brl1/Brr6, and NE/ER proteins; Sec63/Ole1.

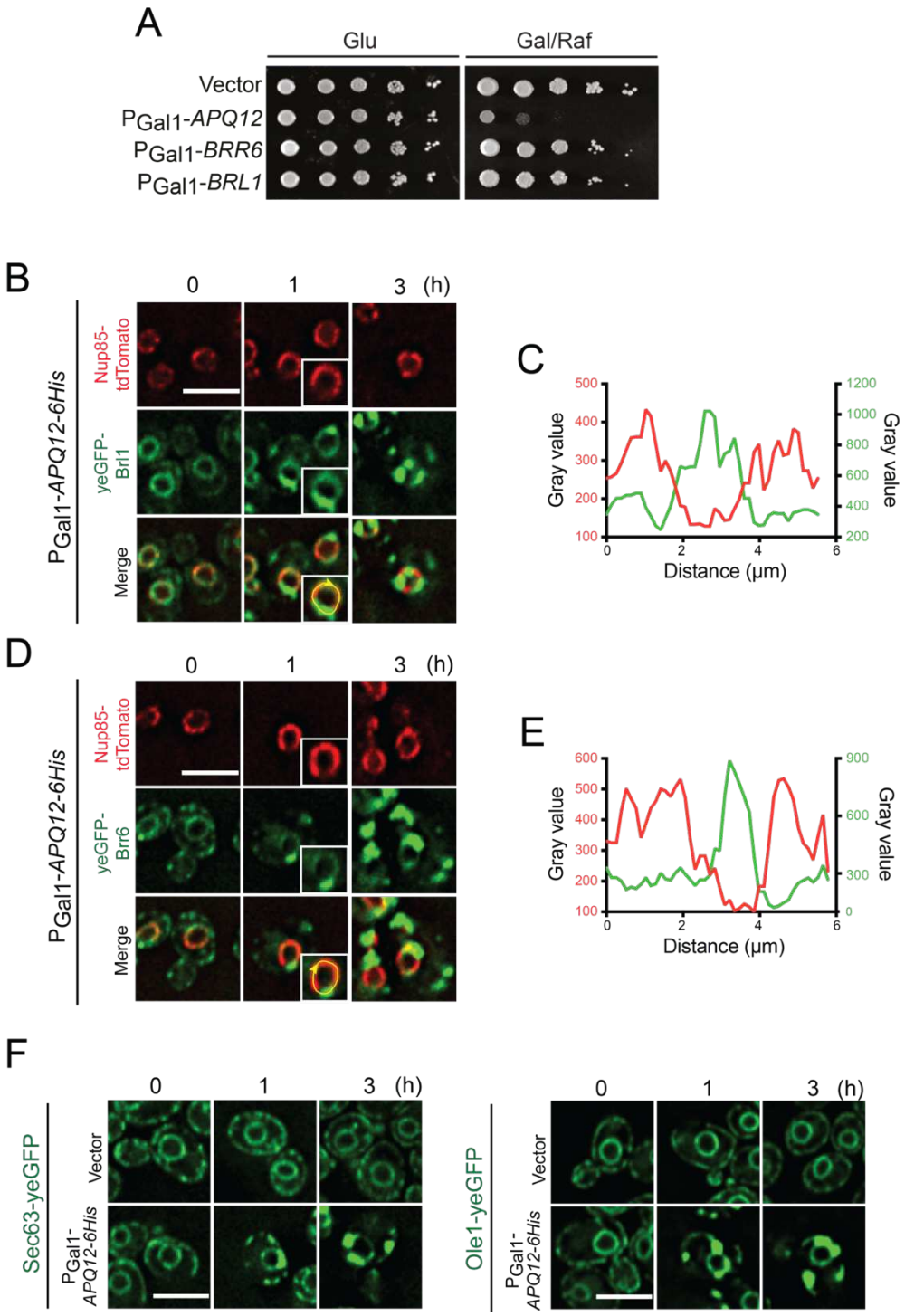

Figure 21. *APQ12* over-expression causes mislocalization of NE/ER proteins. **(A)** Wildtype cells with vector control, *APQ12, BRR6* and *BRL1* under the *GAL1* promoter were spotted onto glucose and galactose/raffinose plates in 10-fold serial dilutions and incubated at 30˚C. **(B)** Fluorescence images of *APQ12* over expression in *yeGFP-BRL1 NUP85-tdTomato* background at indicated time points. **(C)** Line scan of the yeGFP and tdTomato signals of the indicated cell in (B). **(D)** Fluorescence images of over-expression of *APQ12* in cells carrying *yeGFP-BRR6-NUP85-tdTomato* at indicated time points. **(E)** Line scan of the yeGFP and tdTomato signals of the indicated cells in (D). **(F)** Sec63-yeGFP and Ole1-yeGFP carrying cells imaged at indicated times after induction of over-expression of vector control and *APQ12*. Scale bars: 5 μm.

Figure taken and adapted from (Zhang, Khan et al. 2021).

3.5 The Apq12 amphipathic helix has a role in toxicity associated with over-expression

To further dissect the role of the amphipathic helix, I asked whether mutations in the helix can lead to deformation of the NE. First, over-expression of *apq12-ah* was less toxic than its wildtype counterpart (Figure 22A), even though the expression level of both the proteins was somewhat similar (Figure 22B). Second, consistent with the decrease in toxicity of *apq12-ah*, clusters of yeGFP-Brl1 and yeGFP-Brr6 appeared later and were less pronounced compared to the over-expression of wildtype *APQ12* (Figure 22C-D). Therefore, it can be concluded that the AαH of Apq12 has an important role in the proper functioning of Apq12.

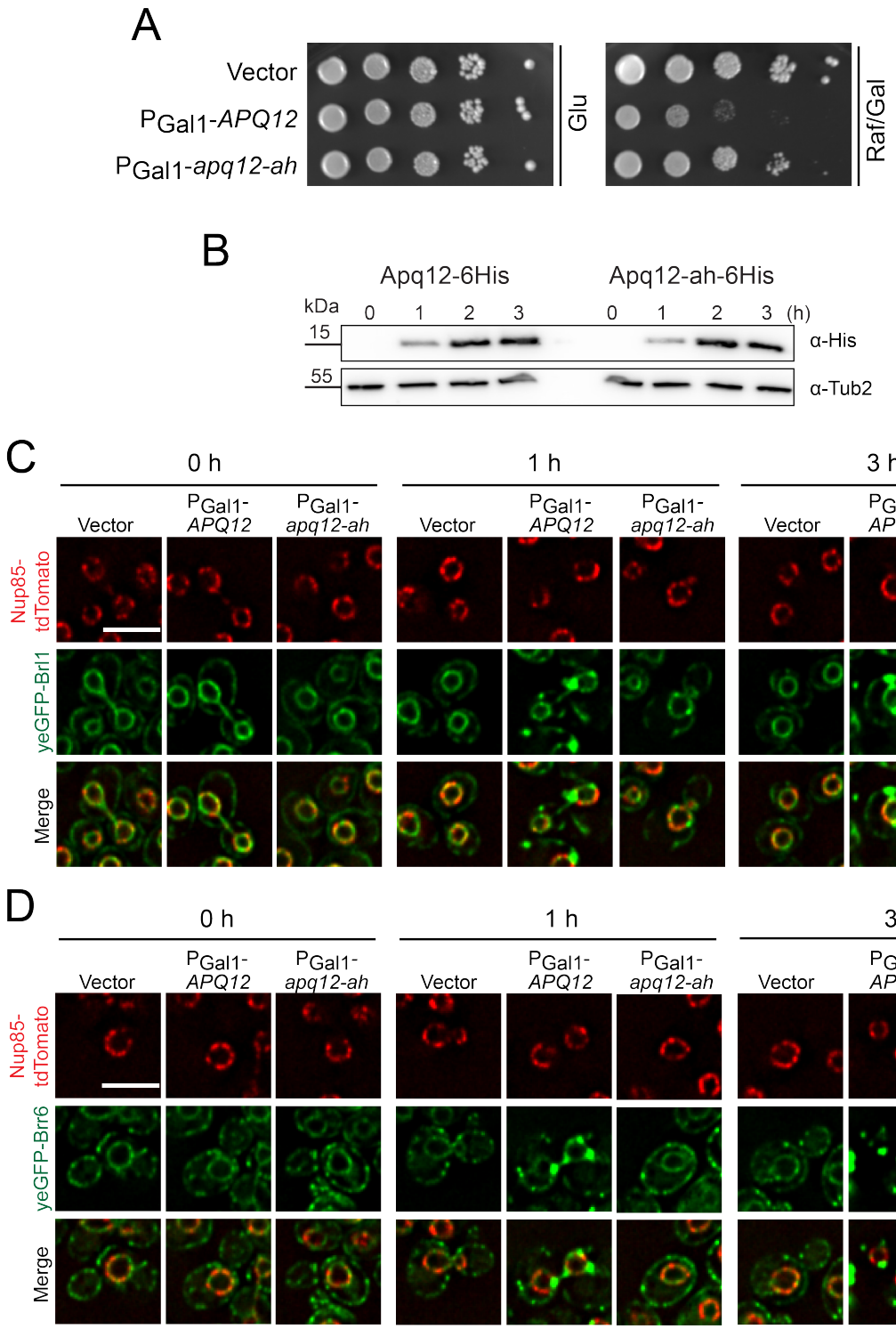

Figure 22. Apq12 AαH has a role in membrane remodeling. **(A)** Spot assay of vector control, *APQ12* and *apq12-ah* under the *GAL1* promoter on glucose and galactose/raffinose plates incubated at 30˚C. **(B)** Western blot showing expression levels of *APQ12-6HIS* and *apq12-ah-6HIS* after galactose induction using anti-His antibodies. Tub2 (yeast beta-tubulin) is used as a loading control. **(C-D)** Time course of vector control, *APQ12* and *apq12-ah* over-expression in cells carrying *yeGFP-BRL1 NUP85-tdTomato* and *yeGFP-BRR6 NUP85-tdTomato*. Scale bars: 5 µm

Figure taken and adapted from (Zhang, Khan et al. 2021).

3.6 Apq12 AαH has a role in maintaining the integrity of the NE and ER

According to above mentioned data it is clear that over-expression of *APQ12* leads to changes in the ONM and the ER. To understand how these changes take place, EM analysis of cells over-expressing *APQ12* and *apq12-ah* was done (Figure 23A-C). Samples were taken at 0, 0.5, 1 and 3 hours after over-expression. At 0 hours after induction of expression of *APQ12*, The NE showed regular spherical morphology (Figure 23A). 0.5 hours after induction, there was an increase in the number of extensions emanating from the ONM/ER (Figure 23B-C). 1 and 3 hours after induction, the major phenotype was ONM encircled vesicles often filled with granular material, possibly ribosomes (Figure 23B-C). The INM remained largely intact until 3 hours post-induction, when it also began to deform, forming small buds protruding into the lumen of the ONM-derived vesicles (Figure 23B-C). In contrast, the over-expression of *apq12-ah* showed a less severe phenotype, consistent with previous data (Figure 23B-C). Only after 3 hours of induction of *apq12-ah* over-expression, the proliferation of the ONM was observed. A quantification of the phenotypes observed at different time points after induction of over-expression of *APQ12* and apq12-ah provides a detailed comparison (Figure 23C).

As seen in Figure 23B, the *APQ12* over-expression induced ONM vesicles contain granular material. To look at the source of these granules, I used an NLS-mRFP as a marker for the nucleoplasm, Rpl25-yeGFP as a ribosomal/cytosolic marker (Figure 23D). Upon induction of over-expression of *APQ12*, yeGFP-Brl1 formed distinct clusters, which were devoid of the NLS-mRFP signal as can be seen in the merged image (Figure 23D). Whereas, Rpl25-yeGFP signal overlapped with the clusters derived from the ER marker, dsRED-HDEL upon over-expression of *APQ12* (Figure 23D). Together this data shows that these ONM derived vesicles contain cytoplasmic material, most probably ribosomes.

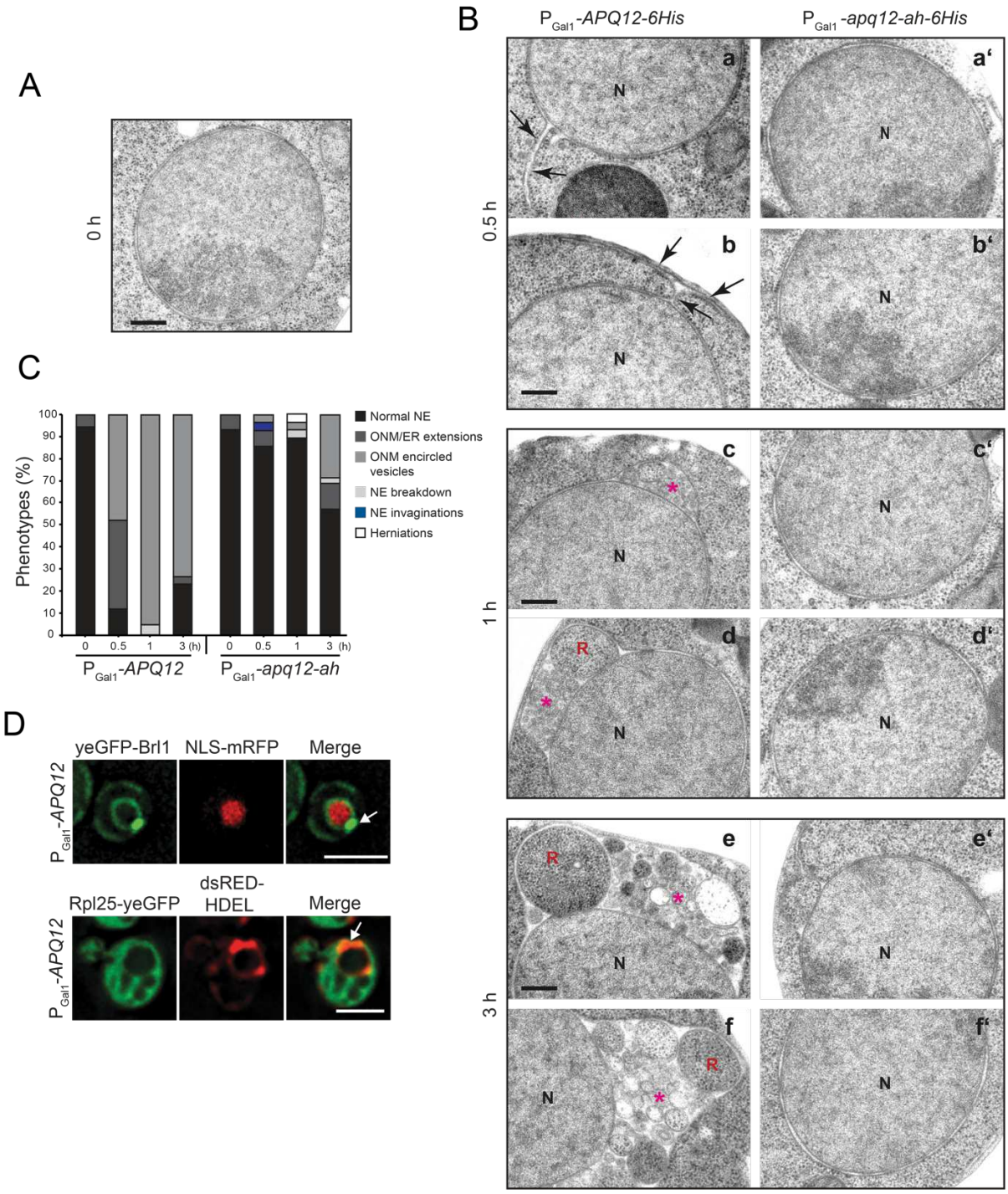

Figure 23. Apq12 causes hyper-proliferation of ER and ONM upon over-expression. **(A)** Electron micrograph of a wildtype cell with vector control. Scale bar: 250 nm. **(B)** EM images of cells expressing *APQ12* and *apq12-ah* at indicated times after induction. Arrows point to over-proliferated membranes. Asterisks indicate ONM encircled vesicles. R: ribosome like particles, N: Nucleus. Scale bar: 200 nm. **(C)** Quantification of phenotypes from (C). n=25. **(D)** Over-expression of *APQ12* in cells carrying *yeGFP-BRL1* and nuclear marker *NLS-mRFP* (upper pane), and ribosomal marker *RPL25-yeGFP* and membrane marker *dsRED-HDEL* (bottom panel) for 3 hours. Scale bars: 3 μm.

Figure taken and adapted from (Zhang, Khan et al. 2021).

I next wanted to analyze the distribution pattern of Apq12-yeGFP and Apq12-ah-yeGFP in response to over-expression. In addition to decorating the NE and ER, the Apq12-

yeGFP signal accumulated at the sites of NE/ER extensions after only 40 minutes of overexpression (Figure 24A). In contrast, Apq12-ah-yeGFP only localized to the NE and ER and did not accumulate even after 60 minutes of over-expression, consistent with the fact that *apq12-ah* does not cause membrane over-proliferation upon overexpression (Figure 24B). This data was corroborated by immuno-EM analysis which detected Apq12-yeGFP signal at the NE extensions and ONM derived vesicles (Figure 24C). Thus, it can be concluded that Apq12 induces membrane proliferation by accumulating at ONM/ER sites in an AαH dependent manner.

In summary, over-expression of *APQ12* leads to formation ONM extensions. These extensions may fold back and fuse with the NE giving rise to vesicles derived from the ONM containing cytoplasmic material (Figure 24D).

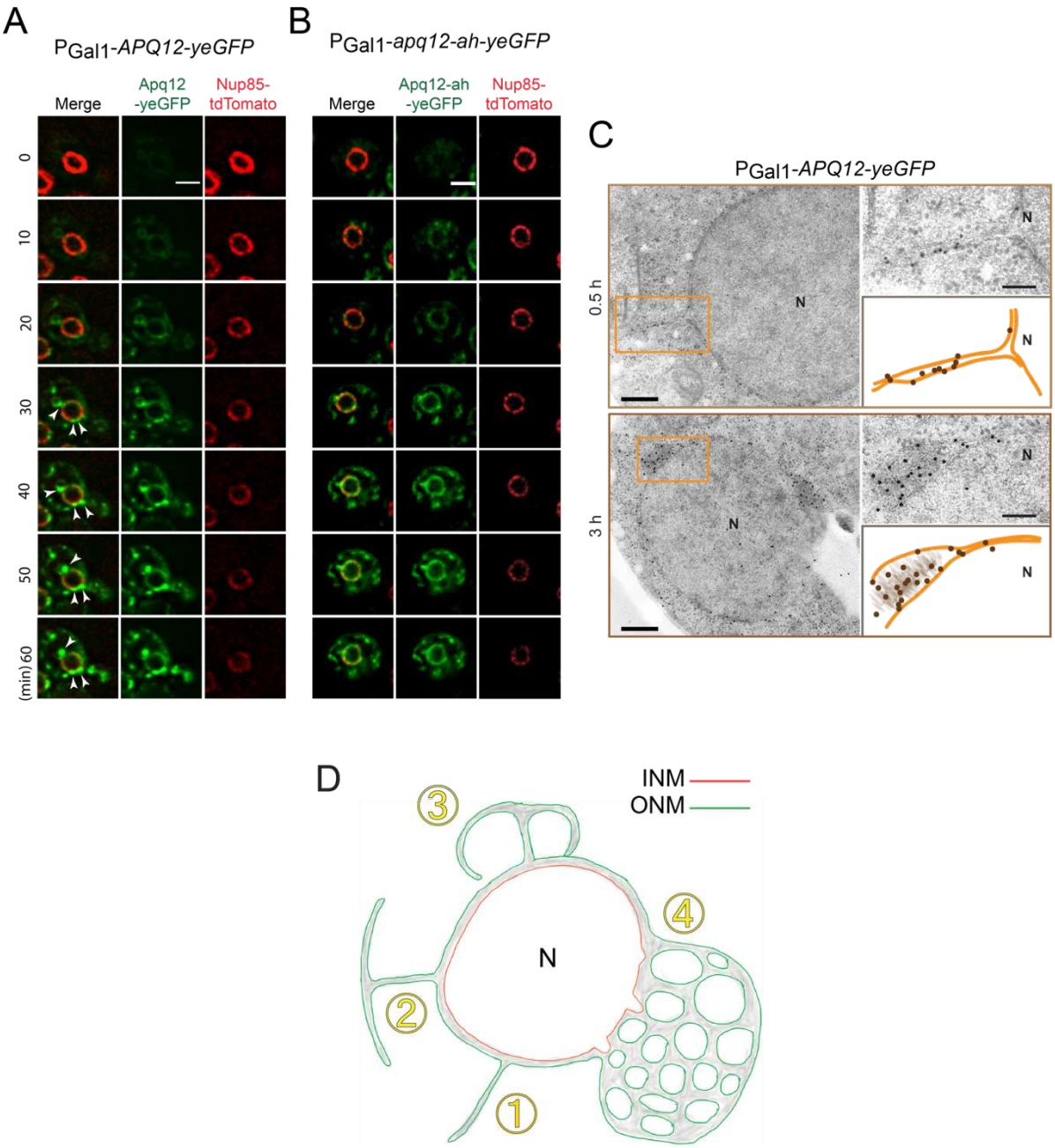

Figure 24. Apq12 localizes to ONM/ER extensions. **(A)** Live-cell imaging of *APQ12-yeGFP* being over-expressed in cells carrying *NUP85-tdTomato* marker. Arrowheads point to ONM/ER extensions. Scale bar: 3 μm. **(B)** Live-cell imaging of *apq12-ah-yeGFP* overexpression in *NUP85-tdTomato* background. Scale bar: 3 μm. **(C)** Immuno-EM images of cells over-expressing *APQ12-yeGFP* for indicated times, using 10 nm gold particles. Magnifications of indicated regions along with cartoons are shown on the left. Scale bars: 250 nm & 50 nm (enlargements). **(D)** Predicted model of membrane hyper-proliferation upon *APQ12* over-expression.

Figure taken and adapted from (Zhang, Khan et al. 2021).

3.7 PA accumulation at the NE is dependent on Apq12

As previously mentioned, Apq12 has been implicated in lipid regulation in the cell (Tamm, Grallert et al. 2011). In order to look at local lipid changes upon *APQ12* and *apq12-ah* over-expression, I utilized lipid sensors (Romanauska and Köhler 2018). These sensors make use of the budding yeast Opi1 transcription factor's phosphatidic acid (PA) recognizing domain, with or without a nuclear localization signal (NLS), fused with mCherry for detection. The nuclear sensor NLS-Q2-mCherry and the cytoplasmic sensor Q2-mCherry detect PA at the INM and ONM, respectively. At 0 hours after induction of *APQ12*, the Q2-mCherry signal localized to the plasma membrane and weakly to the nucleus (Figure 25A-B). 1 hour after over-expression of *APQ12*, the Q2-mCherry sensor, not only accumulated along the NE, it also colocalized with the yeGFP-Brl1 clusters. Similar results were obtained at 3-hour time point. On the other hand, upon over-expression of *apq12-ah*, the Q2-mCherry sensor maintained its plasma membrane localization and did not stain the NE even after 3 hours (Figure 25A-B). Analysis of the nuclear sensor NLS-Q2-mCherry showed uniform nuclear staining at 0 hours after induction (Figure 25C-D). By 1 hour after induction of *APQ12*, NLS-Q2-mCherry already showed enrichment at the NE, specifically at the sites of yeGFP-Brl1 clusters. In contrast, over-expression of *apq12-ah* did not redistribute the NLS-Q2-mCherry sensor to the nuclear rim as it maintained a smooth nucleoplasmic staining (Figure 25C-D). This data highlights that not only does Apq12 induce enrichment of PA at the NE, but the AαH is also required for this step.

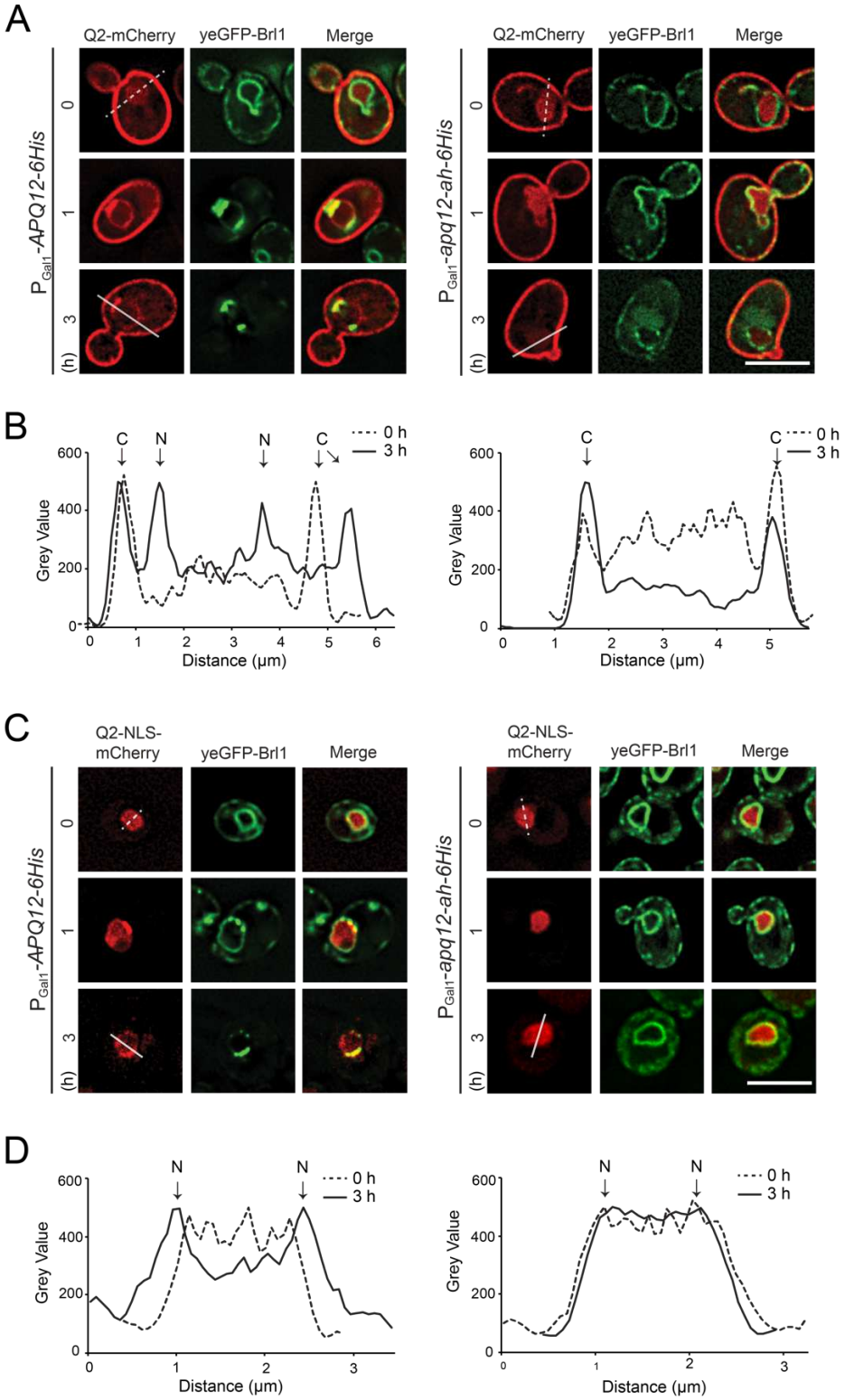

Figure 25. *APQ12* overexpression induces PA accumulation at the NE in an AαH dependent manner. **(A)** Over-expression of *APQ12* and *apq12-ah* in cells carrying Q2-mCherry PA sensor and yeGFP-Brl1 marker. Images were taken at indicated at the time points. Scale bar: 5 μm. **(B)** Plot profiles of mCherry signal along the indicated lines. Arrows point to nuclear (N) and cytoplasmic (C) peaks. **(C)** Over-expression of *APQ12* and *apq12-ah* in cells carrying the nuclear NLS-Q2-mCherry PA sensor and yeGFP-Brl1 marker. Images were obtained at indicated time points. Scale bar: 5 μm. **(D)** Plot profiles of mCherry signal along the lines shown. Arrows indicate nuclear (N) peaks.

Figure taken and adapted from (Zhang, Khan et al. 2021).

3.8 Association of Apq12 with NPCs is independent of its AαH

The fact that Apq12 only associates with a subset of NPCs (Figure 17D), indicates that it might act in a manner similar to Brl1 and Brr6, such that it only interacts with newly assembled/assembling NPCs but not mature NPCs. To test this, I made use of temperature dependent degrons of Brl1 and Brr6 (*td-brl1* and *td-brr6*) that accumulate herniations or NPC assembly intermediates at 37˚C (Zhang, Neuner et al. 2018), and analyzed at the localization of Apq12 and Apq12-ah. Results showed that yeGFP-Apq12 colocalized with the Nup85-tdTomato foci which represent herniations in both *td-brl1* and *td-brr6* cells, but not in the wildtype cells (Figure 26A). A higher Pearson correlation coefficient is also indicative of the observed phenotype (Figure 26B). A similar trend was seen in the case of yeGFP-Apq12-ah, where the Nup85-tdTomato signal showed a level of correlation with yeGFP-Apq12-ah in *td-brl1* and *td-brr6* cells (Figure 26C-D). Immuno-EM analysis further confirmed that both Apq12 and Apq12-ah were enriched at the sites of herniations (Figure 26E). To rule out the possibility that the enrichment of Apq12 is not a secondary outcome of increased surface area of the herniations compared to the surrounding NE, a quantitative assessment, to determine the number of gold particles relative to the length of membrane along the NE compared to herniations, was done. Results revealed that there were less than 1 gold particles/μm of the NE in wildtype as well as *td-brr6* and *td-brl1* cells, whereas this number increase to 5 gold particles/μm along herniations (Figure 26F). Together, this data clearly indicates an enrichment of Apq12 at NPC assembly intermediates, and this enrichment is not dependent on its AαH.

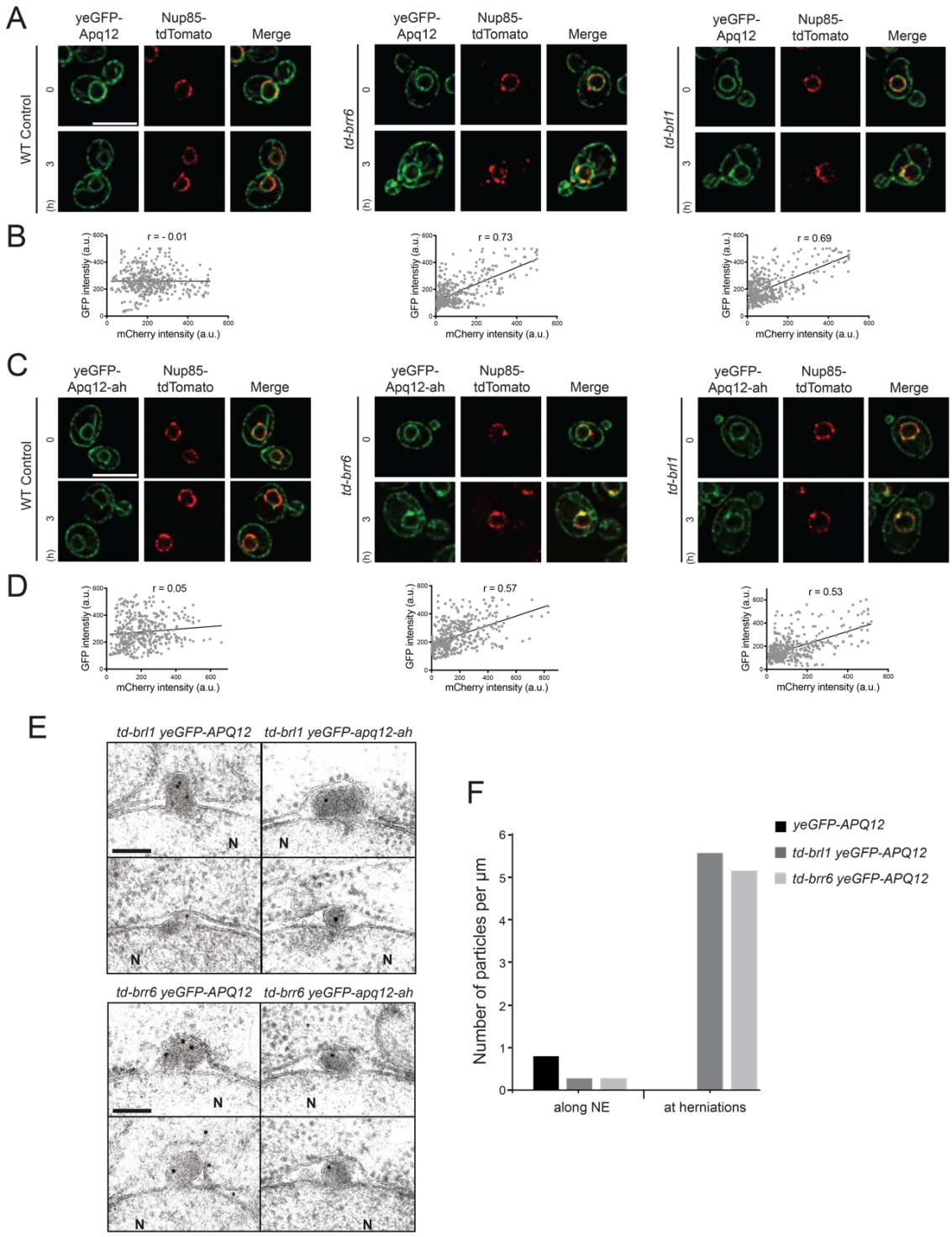

Figure 26. Apq12 interacts with NPC biogenesis intermediates. **(A)** Wildtype, *td-brl1* and *td-brr6* cells carrying *APQ12-yeGFP* and *NUP85-tdTomato* NPC marker imaged at 0 and 3 hours after galactose induction at 37˚C. Scale bar: 5 µm. **(B)** Pearson correlation coefficient (r) of mCherry and yeGFP signals along the NE of cells shown in the insets. **(C)** Wildtype, *td-brl1* and *td-brr6* cells carrying *apq12-ah-yeGFP and NUP85-tdTomato* NPC marker imaged at 0 and 3 hours after galactose induction at 37˚C. Scale bar: 5 µm. **(D)** Pearson correlation coefficient (r) of mCherry and yeGFP signals along the NE of cells shown in the insets. **(E)** Immuno-electron micrographs of *td-brl1* and *td-brr6* cells carrying *APQ12-yeGFP* or *apq12-ah-yeGFP*, incubated at 37˚C after addition of galactose, using anti-GFP antibodies and 10 nm gold particles. Scale bar: 100 nm. **(F)** Quantification of number of gold particles/µm of the NE. 24 particles were analyzed for *yeGFP-APQ12*, 32 for *td-brl1 yeGFP-APQ12* and 39 for *td-brr6 yeGFP-APQ12.*

Figure taken and adapted from (Zhang, Khan et al. 2021).

3.9 Apq12 regulates the interaction of Brl1 and Brr6 in an AαH dependent manner

Previous research has shown that there are physical and genetic interactions between *APQ12, BRL1* and *BRR6* (Scarcelli, Hodge et al. 2007, Hodge, Choudhary et al. 2010, Lone, Atkinson et al. 2015). The expression of Brl1 increased in response to deletion (*apq12Δ*) and mutation (*apq12-ah*) of *APQ12* compared to the wildtype (Figure 27A). The increase was more pronounced in the case of *apq12Δ* compared to *apq12-ah* (Figure 27A-B). Similarly, expression of *BRR6-yeGFP* increased in response to *apq12-ah* mutation (Figure 27C-D). *BRR6-yeGFP*, however, was lethal in combination with *apq12Δ* and therefore could not be tested. Analysis of localization of Brl1-yeGFP and Brr6-yeGFP in response to *apq12-ah* mutation revealed that although the localization pattern of both proteins remained similar to the wildtype condition, the signal intensity was increased in case of *apq12-ah* (Figure 27E). This is consistent with the protein expression data in Figure 27A-D. I further wanted to study whether the increase in expression of *BRL1* and *BRR6* in response to *apq12-ah* resulted in an increased interaction between the proteins. Brr6-yeGFP was pulled down and the immunoprecipitate was probed for Brl1 and Apq12-6HA/Apq12-ah-6HA in a co-IP experiment (Figure 27F). Results indicated that the interaction between Brl1 and Brr6 increased in cells expressing *apq12-ah* compared to *APQ12*. Interaction between Brr6 and Apq12 also increased in *apq12-ah* compared to *APQ12* (Figure 27F-G). Thus, the amphipathic helix of Apq12 has a role in regulating the interaction between Ap12, Brl1 and Brr6.

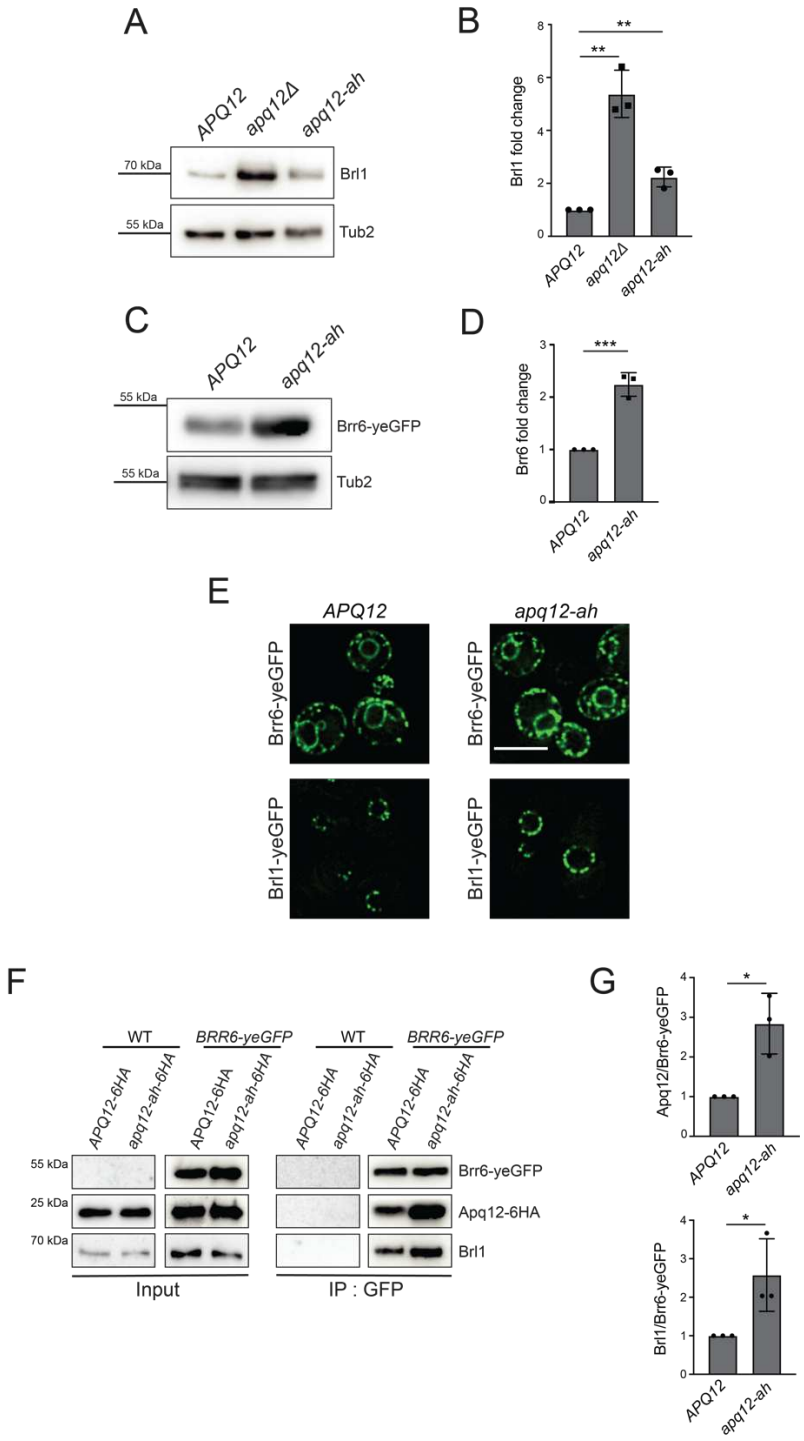

Figure 27. Apq12 regulates the interaction between Brr6 and Brl1 via its amphipathic helix. **(A)** Western blot of Brl1 expression in *APQ12*, *apq12Δ* and *apq12-ah*, using anti-Brl1 antibody. Tub2 is used as a loading control. **(B)** Quantification of (A) with normalization to Tub2. Data are presented as mean ± SD n=3 **p<0.01. **(C)** Immunoblot of Brr6-yeGFP levels with anti-GFP antibody in *APQ12* and *apq12-ah* background and Tub2 as a loading control. **(D)** Quantification of data from (C) after normalization to Tub2. Data are presented as mean ± SD n=3 **p<0.001. **(E)** Fluorescence images of cells expressing Brr6-yeGFP or Brl1-yeGFP in *APQ12* and *apq12-ah* background. Scale bar: 5 μm. **(F)** Co-IP using anti-GFP antibodies from *APQ12-6HA* and *apq12-ah-6HA* cells. Anti-GFP antibodies were used for detection of Brr6-yeGFP, anti-HA antibodies for Apq12-6HA/Apq12-ah-6HA and anti-Brl1 antibodies for Brl1. **(G)** Quantification of (F). Ratios between Apq12 and Brr6 and Brl1 and Brr6 are shown. Data is presented as mean ± SD. n=3. Two-tailed t-test *p<0.05, **p<0.01, ***p<0.001, ****p<0.0001

Figure taken and adapted from (Zhang, Khan et al. 2021).

"A perinuclear α-helix with amphipathic features in Brl1 promotes NPC assembly" - (Vitale, Khan et al. 2022)

3.10 Characterization of the PNS region of Brl1

Brl1, an essential protein, interacts with Apq12, as depicted in Figure 27. Both of these genes also exhibit genetic interactions with *NUP116*, which encodes an FG nucleoporin and plays a scaffolding role during interphase assembly of NPCs (Scarcelli, Hodge et al. 2007, Onischenko, Tang et al. 2017, Zhang, Neuner et al. 2018). Overexpression of *BRL1* suppresses the herniations observed in *nup116Δ* (Zhang, Neuner et al. 2018), leading us to believe that *BRL1*, especially its perinuclear space (PNS) region, has a role in INM/ONM fusion during the assembly of NPCs. AlphaFold protein structure database (Jumper, Evans et al. 2021) predicts two distinct structural elements: an alpha helix (aa 386-403), confirmed to be amphipathic (AαH) in nature by HeliQuest (Figure 28C) (Gautier, Douguet et al. 2008), and an antiparallel helix bundle (aa 321-372) stabilized by two disulfide bridges (DAH) (Figure 28A-B). The AαH and DAH are flanked by two transmembrane domains: TM1 (aa 300-320) and TM2 (aa 408-428) (Figure 28A-B).

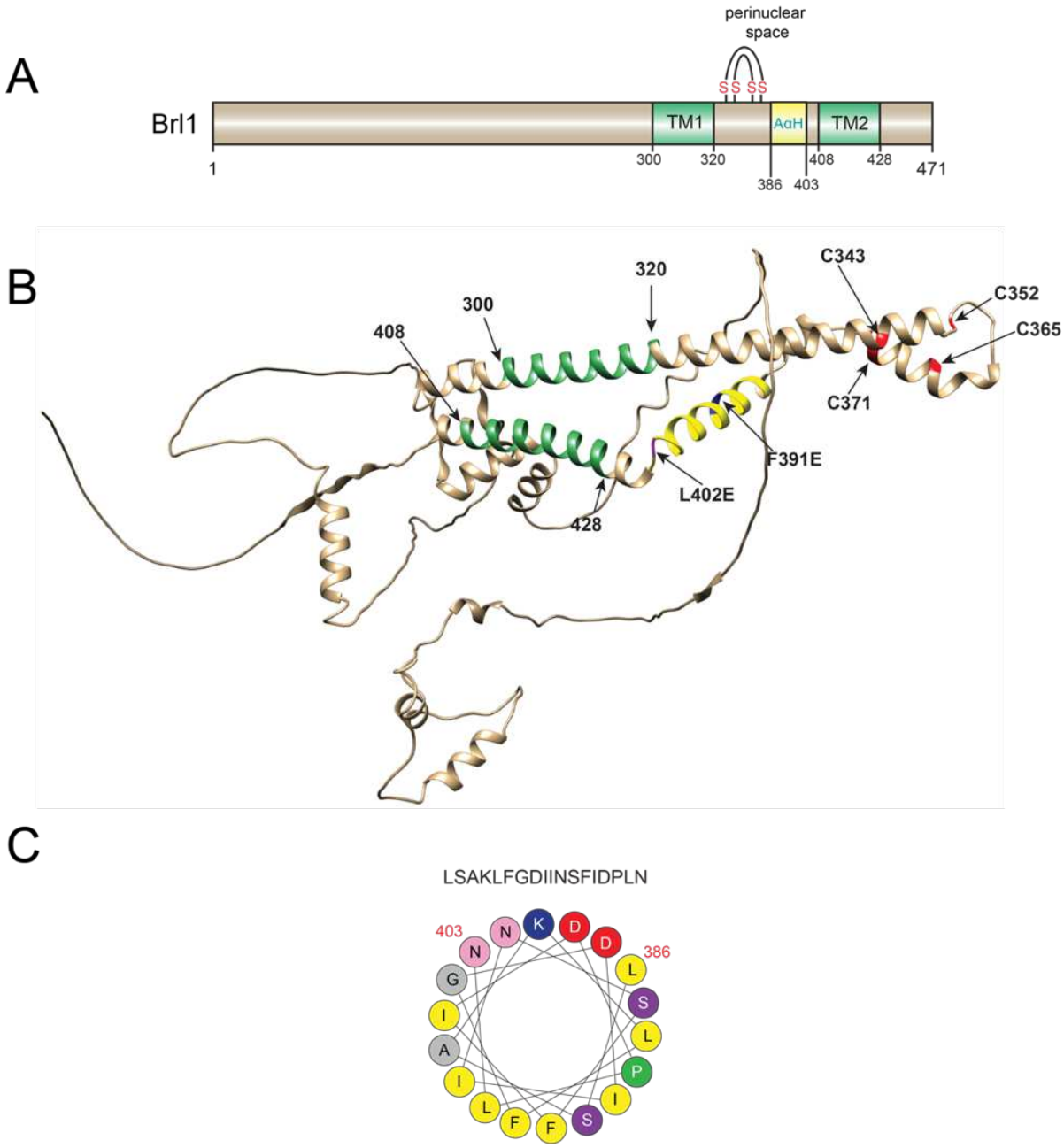

Figure 28. Domain organization of Brl1. **(A)** Schematic of Brl1 showing an amphipathic helix (AαH) and 2 disulfide bonds in between 2 transmembrane (TM) domains. **(B)** Predicted AlphaFold structure of Brl1. TMs are shown in green and the AαH in yellow. The 4 cysteines are shown in red. **(C)** The AαH predicted by HeliQuest (Gautier, Douguet et al. 2008).

Figure taken and adapted from (Vitale, Khan et al. 2022).

Comparison of AlphaFold predictions of Brl1/Brr6-like proteins from *Saccharomyces cerevisiae*, *Schizosaccharomyces pombe*, *Candida albicans* and *Plasmodium falciparum*, indicates that the AαH and the DAH are conserved motifs in organisms with closed mitosis (Figure 29A-D).

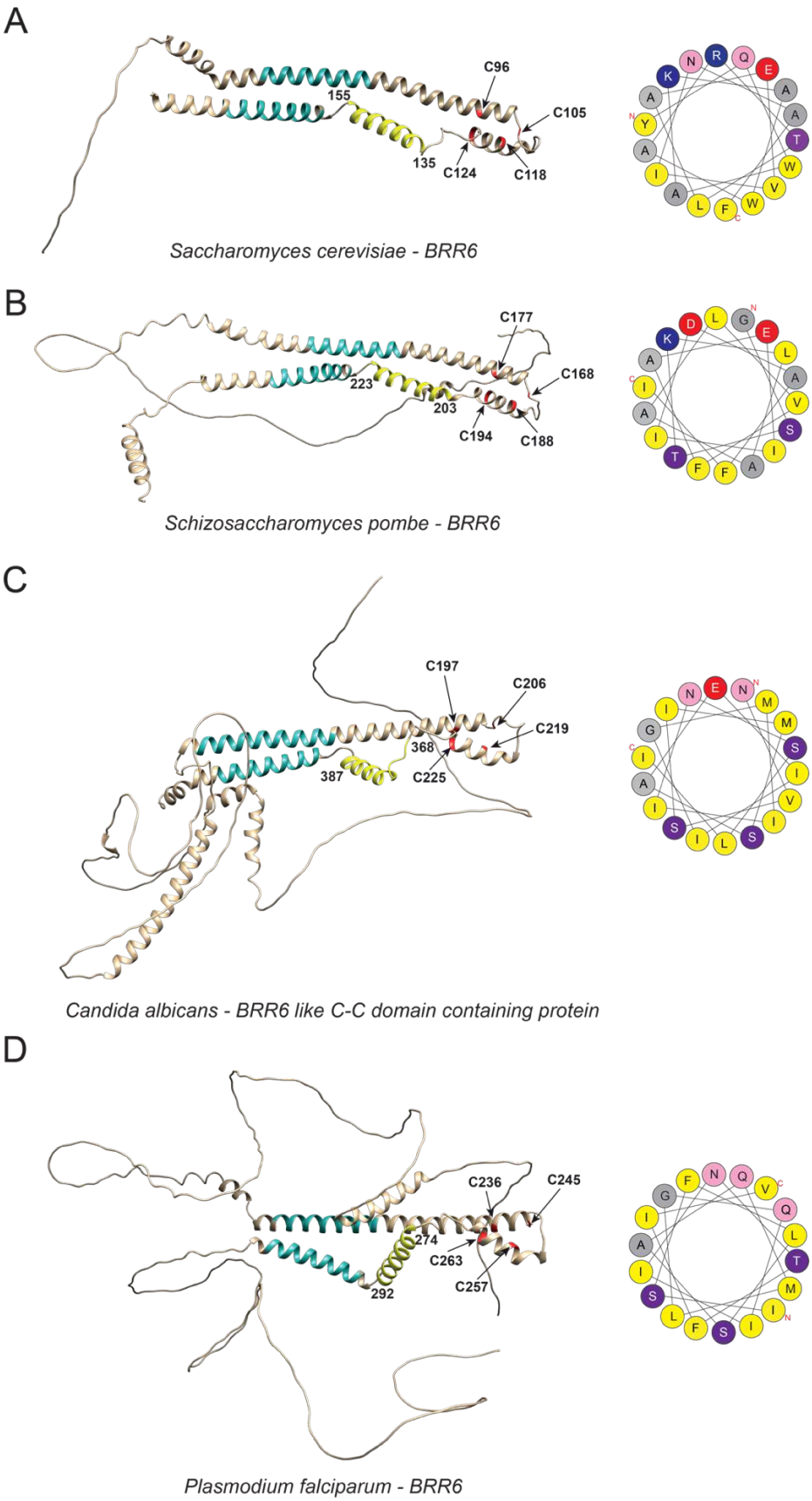

Figure 29. (A-D) Domain organization of Brl1/Brr6 like proteins from indicated organisms as predicted by AlphaFold Protein Structure Database (left). HeliQuest predictions of their respective AαHs (right).

Figure taken and adapted from (Vitale, Khan et al. 2022).

To test the importance of the predicted AαH, I introduced point mutations: F391E, L402E and F391P (Figure 30A) to disrupt its amphipathic nature. First, I observed that the AαH fused with yeGFP has the ability to localize to NE/ER, similar to Brl1. However, mutation in this AαH led to a loss of this localization (Figure 30B). Analysis of these mutants by plasmid shuffle approach showed that these mutations cause cell death (Figure 30C). I also analyzed mutations of conserved residues in Brl1/Brr6-like proteins (Gardner, O'Toole et al. 2021) in the DAH (Figure 30D). While most of the mutations had no impact on cell viability, the C343Y mutation showed a temperature sensitive phenotype at 37˚C and the C365S and C371S double mutant showed reduced growth at 30˚C and 37˚C (Figure 30E). Taken together, the AαH of Brl1 is essential for its function, as mutations in it lead to loss of cell viability.

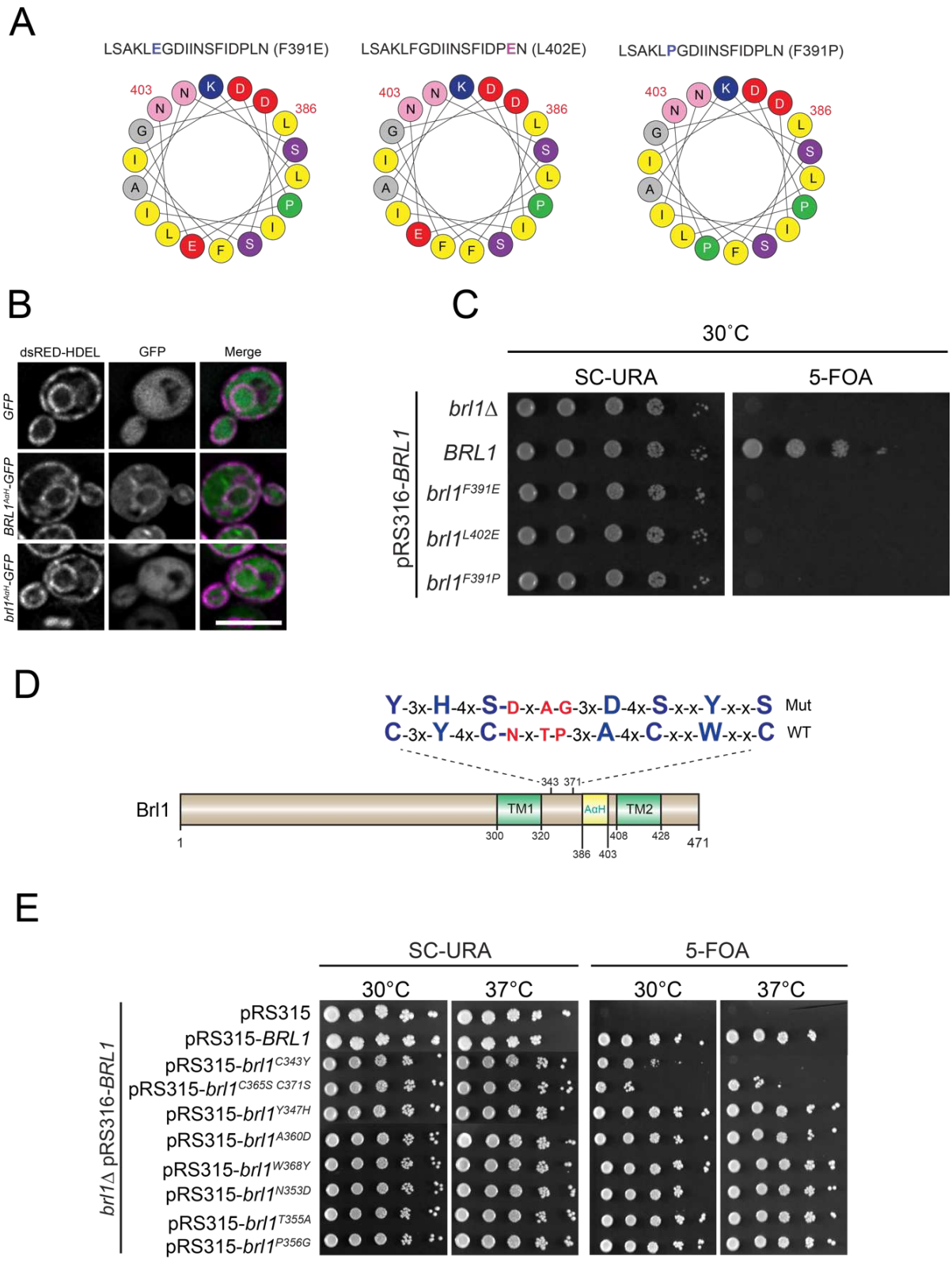

Figure 30. The Brl1 AαH is essential for its function. **(A)** HeliQuest predictions of point mutations in AαH; AαH^{F391E}, AαH^{L402E}, AαH^{F391P}. **(B)** *BRL1-AαH-yeGFP and brl1^{F391E}-AαH-yeGFP* expressed in *dsRED-HDEL* background. Scale bars: 5 µm. **(C)** Spot assay for growth of *BRL1*, *brl1^{F391E}*, *brl1^{L402E}* and *brl1^{F391P}* on SC-Ura and 5-FOA medium at 30˚C. **(D)** Schematic showing DAH mutations in Brl1. **(E)** Growth test of *BRL1* DAH mutants on SC-Ura and 5-FOA plates at 30˚C and 37˚C.

Figure taken and adapted from (Vitale, Khan et al. 2022).

3.11 Overexpression of *BRL1* helix mutants deforms the NE

I then tested how over-expression of *BRL1* mutants affects the cells. *Brl1^{F391E}*, *Brl1^{F391P}* and *Brl1^{L402E}* mutants expressed under the *GAL1* promoter proved to be toxic for cells (Figure 31A). *BRL1*, *APQ12* and *apq12-ah* were used as controls. On the other hand, over expression of the DAH mutants did not affect the growth of cells, except the C343Y and C365Y C371Y disulfide bond mutants, which showed mild toxicity (Figure 31B). I then combined the AαH mutant F391E with the DAH mutants to test whether the toxicity associated with *brl1^{F391E}* is dependent on the DAH. Results showed that over-expression of *brl1^{F391E}* combined with DAH mutants was still toxic (Figure 31B) indicating that DAH is not important for the function of the AαH.

Next, I tested whether Brl1 competes with Brl1^{F391E}. Co-overexpression of *BRL1* and *brl1^{F391E}* under the *GAL1* promoter resulted in partial rescue of the toxic phenotype associated with *brl1^{F391E}* overexpression (Figure 31C).

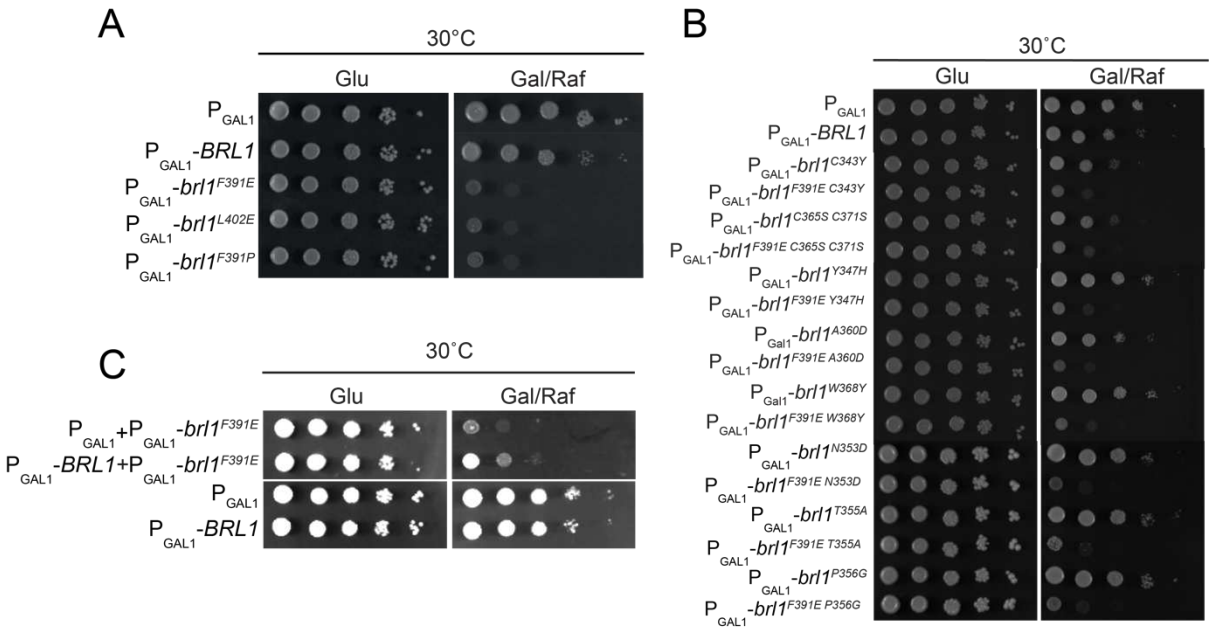

Figure 31. Overexpression of Brl1 AαH mutants is toxic for cells. **(A)** Cells with *BRL1*, *BRL1^{F391E}*, *BRL1^{L402E}* and *BRL1^{F391P}* under the *GAL1* promoter were spotted onto glucose and galactose/raffinose plates and incubated at 30˚C. **(B)** Growth assay of DAH mutants and DAH AαH double mutants under the *GAL1* promoter at 30˚C. **(C)** Growth assay of vector control and *brl1^{F391E}*, and *BRL1* and *brl1^{F391E}* over-expression at 30˚C.

Figure taken and adapted from (Vitale, Khan et al. 2022).

To look at the morphology of the cells, I used the dsRED-HDEL NE/ER reporter. Petal-like structures were observed on the NE in response to *brl1^{F391E}*, *brl1^{L402E}* and *brl1^{F391P}* over-expression (Figure 32A). This phenotype was observed as early as 1 hour after the induction of expression and became increasingly stronger (Figure 32B). DAH mutants did

not produce this phenotype except the C343Y mutant (Figure 32A), consistent with previous data. However, when combined with the F391E mutation, the NE again deformed and showed petal-like structures (Figure 32A). I then wanted to analyze the localization of *brl1*^{F391E} by tagging it with yeGFP and over-expressing it in a strain carrying the dsRED-HDEL reporter. Brl1^{F391E}-yeGFP localized to the NE and to a lesser extent (Figure 32C). This is in contrast to Brl1-yeGFP which localized to both the NE and ER to a similar extent. Notably, Brl1^{F391E} also accumulated at the petal like structures as indicated by its colocalization with the dsRED-HDEL reporter (Figure 32C).

Together these results show that over-expression of AαH mutants deforms the NE.

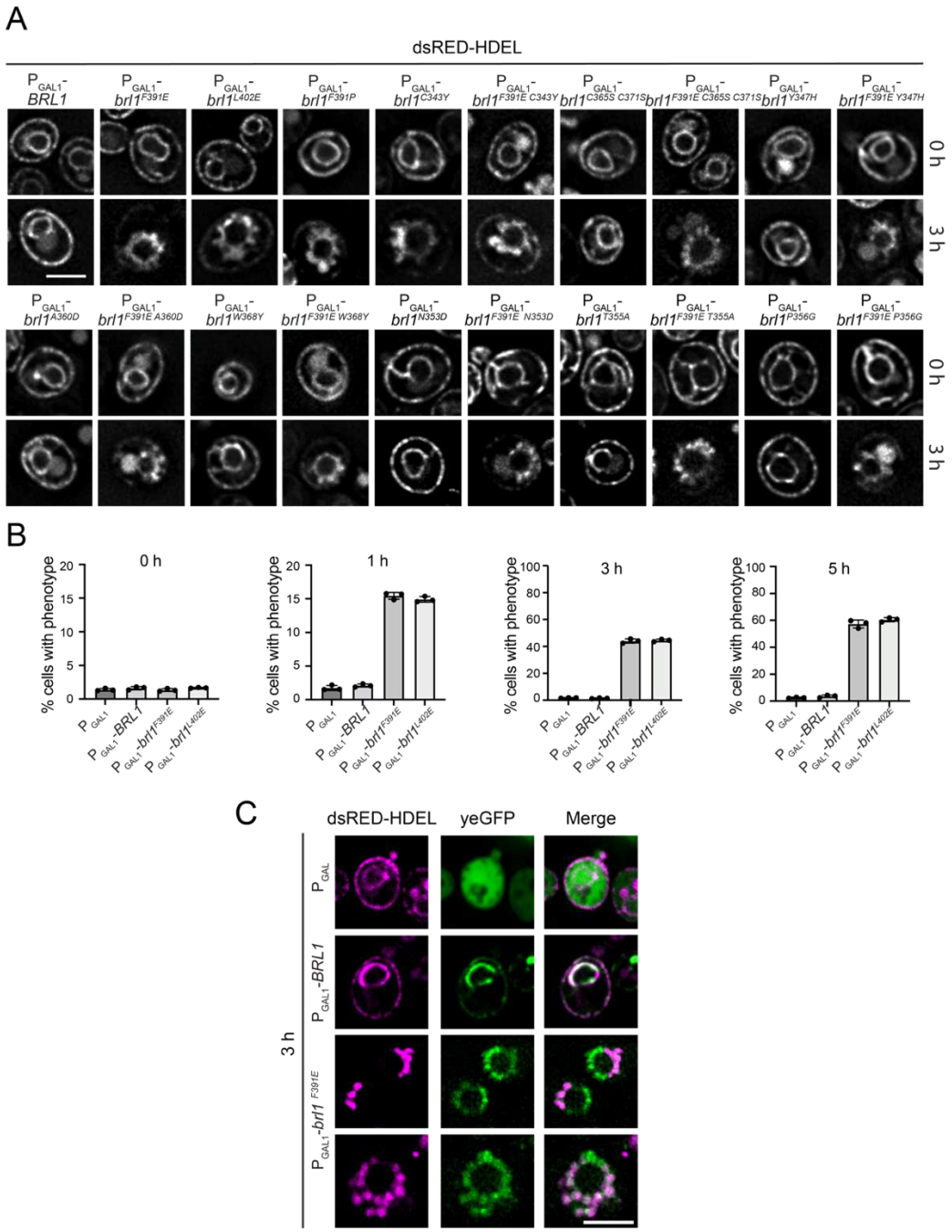

Figure 32. Overexpression of Brl1 AαH mutants causes membrane deformations. **(A)** Fluorescence images of *BRL1*, AαH mutants and DAH AαH double mutants. Constructs were over-expressed for 3 hours in dsRED-HDEL marker carrying cells. Scale bar: 3 µm. **(B)** Quantification of petal-like phenotype from (A) after 0, 1, 3 and 5 hours over-expression. **(C)** Fluorescence images of *yeGFP*, *BRL1-yeGFP* and *brl1^{F391E}-yeGFP* over-expression in *dsRED-HDEL* background. Scale bar: 5 µm.

Figure taken and adapted from (Vitale, Khan et al. 2022).

3.12 Over-expression of *brl1^{F391E}* leads to growth of the INM and ONM

To take a deeper look at the petal like structures observed upon over-expression of *brl1^{F391E}*, EM analysis was done. Data confirmed the phenotype observed by fluorescence microscopy. The petals appeared to be large ONM/INM deformations directed toward the

cytoplasm and open toward the nucleus (Figure 33A). These petals sometimes contained layers of double membranes. Some of these structures also detached from the nucleus and localized in the cytoplasm (Figure 33B). The NE, however, looked intact in response to *BRL1* over-expression, except in some cases where membrane sheets were observed in the nucleus after 5 hours, in line with published data (Figure 33A) (Zhang, Neuner et al. 2018).

I further wanted to analyze the content of these petal-like structures, using Rpl25-yeGFP and NLS-mRFP as cytoplasmic and nucleoplasmic markers, respectively. Fluorescence microscopy analysis showed that dsRED-HDEL labelled petals produced upon over-expression of $brl1^{F391E}$ were devoid of Rpl25-yeGFP signal (Figure 33C). Interestingly, the petal-like structures contained NLS-mRFP signal (Figure 33C), suggesting the presence of nuclear material within these NE extensions.

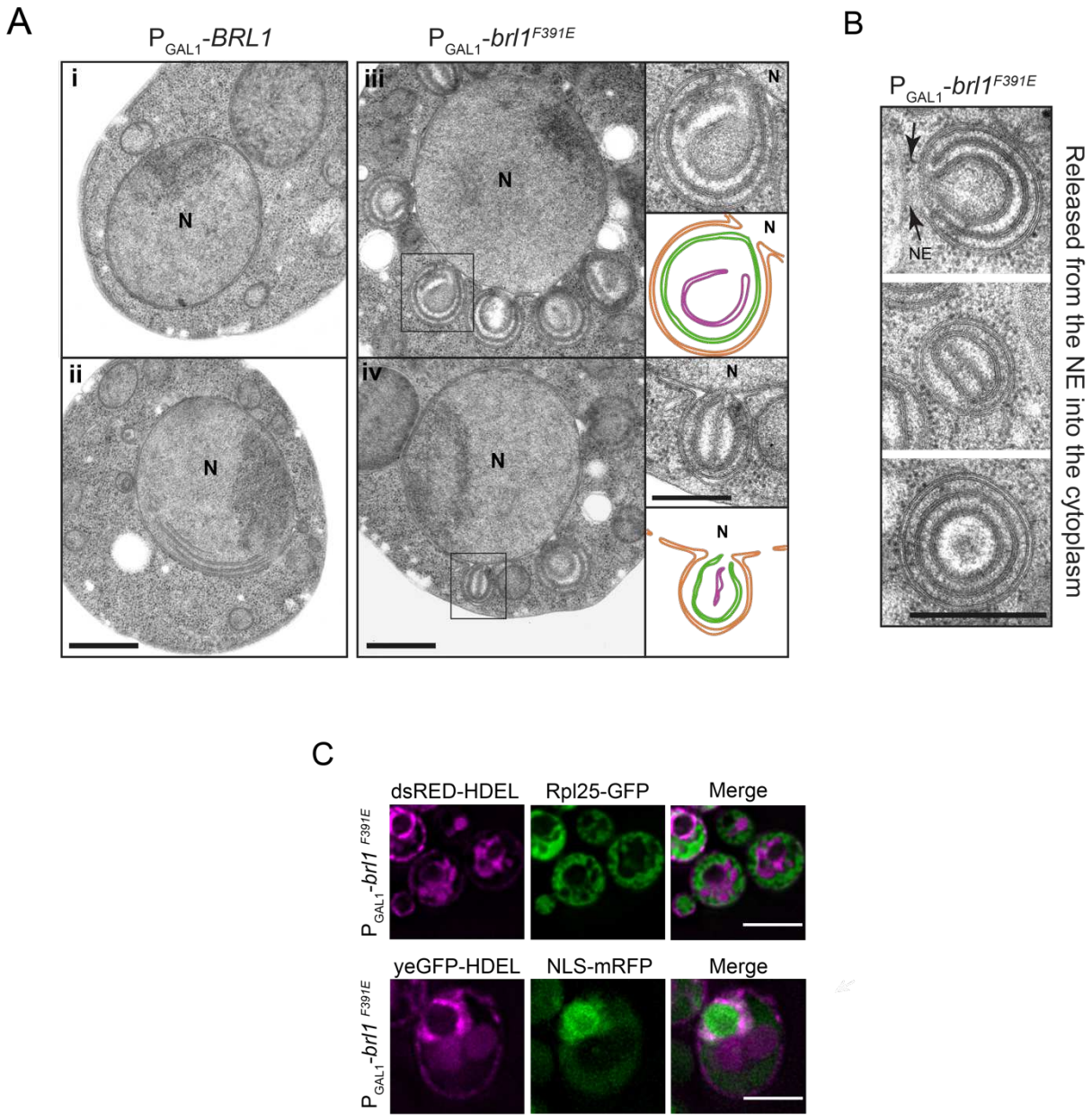

Figure 33. *brl1^{F391E}* over-expression induces the formation of petal-like structures. **(A)** Electron micrographs of cells over-expressing *BRL1* and *brl1^{F391E}* for 5 hours (left). Enlargements and cartoons of boxed regions (right). N: nucleus. Scale bar: 500 nm. **(B)** Example images of petal-like structures detached from the nucleus. Scale bar: 400 nm. **(C)** Fluorescence images of cells carrying membrane marker dsRED-HDEL and ribosomal marker Rpl25-yeGFP (top) and membrane marker yeGFP-HDEL and nuclear marker NLS-mRFP (bottom) over-expressing *brl1^{F391E}*. Scale bar: 5 µm.

Figure taken and adapted from (Vitale, Khan et al. 2022).

3.13 Localization of cytoplasmic nucleoporins is affected by *brl1^{F391E}* over-expression

Next, I analyzed the localization of nucleoporins in relation to the deformation phenotype of the NE. Nucleoporins from the Y-complex (Nup133, Nup84), Nup82 complex and cytoplasmic Nups (Nup159, Nup82, Nsp1, Nup116, Nup42) were examined. The over-expression of *BRL1-yeGFP* had no impact on the distribution of any of the tested Nups

(Figure 34A-B). However, cytoplasmic Nups (Nup159, Nsp1, Nup42) showed a disturbed localization upon over-expression of *brl1^{F391E}-yeGFP* (Figure 34A-B). Not only was their distribution no longer smooth, but they also colocalized with the *brl1^{F391E}* signal at the petal-like structures in 43% (Nup159), 35% (Nsp1), and 74% (Nup42) of the cells. No detectable change was observed in the distribution of other Nups tested (Figure 34A-B).

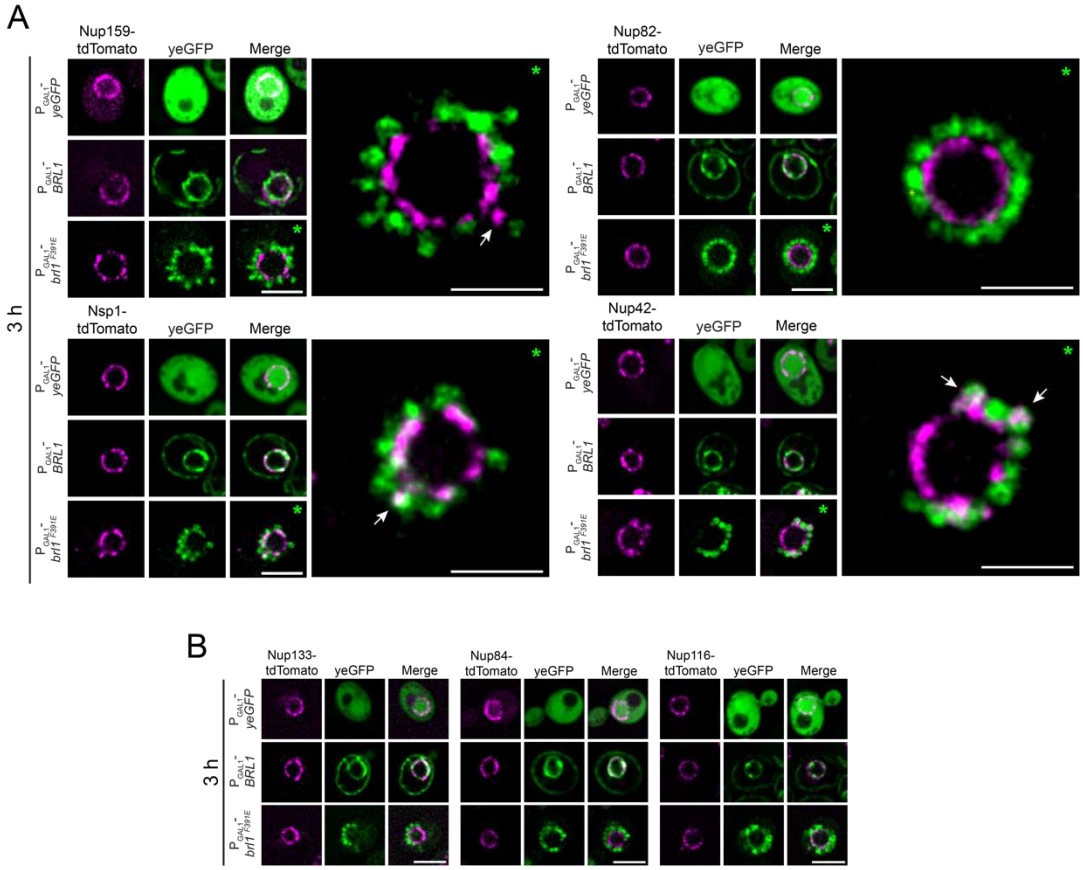

Figure 34. Over expression of *brl1^{F391E}* affects Nsp1, Nup159 and Nup42. **(A)** Florescence microscopy images of cells carrying *NUP159-yeGFP, NUP82-tdTomato*, *NSP1-tdTomato* and *NUP42-tdTomato* tags over-expressing vector control, *BRL1* and *brl1^{F391E}*. Asterisks indicate 5-fold enlargements. Arrows point to mislocalized signal. Scale bars: 5 μm, 2 μm (enlargements). **(B)** Over-expression of vector control, BRL1 and *brl1^{F391E}* in cells with *NUP133-tdTomato*, *NUP84-tdTomato* and *NUP116-tdTomato* tags. Scale bars: 5 μm.

Figure taken and adapted from (Vitale, Khan et al. 2022).

To confirm that only a subset of nucleoporins is affected upon over-expression of *brl1^{F391E}*, I compared the distribution of Nup159-yeGFP with Nup82-tdTomato and Nup116-tdTomato in the same cell. While Nup82 and Nup116 displayed uniform distribution, Nup159 showed clustering when *brl1^{F391E}* was over-expressed (Figure 35A). This effect can also be observed in the accompanying line scans.

I then wanted to examine whether *brl1^{F391E}* over-expression blocks NPCs assembly. To that end, I used the recombination-induced tag exchange (RITE) system (Terweij, van

Welsem et al. 2013). This system allows exchange of tags by Cre mediated recombination enabling differentiation between new and old proteins. I tagged Nup188, an inner ring nup, with the RITE cassette switching it from mCherry to yeGFP fluorophore. Results showed that Nup188-yeGFP was still incorporated into the NPCs upon over-expression of *brl1*^{F391E} similar to *BRL1* (Figure 35B).

In conclusion, *brl1*^{F391E} over-expression affects a subset of cytoplasmic nucleoporins; Nup159, Nup42 and Nsp1. Furthermore, it does not block the assembly of NPC cores.

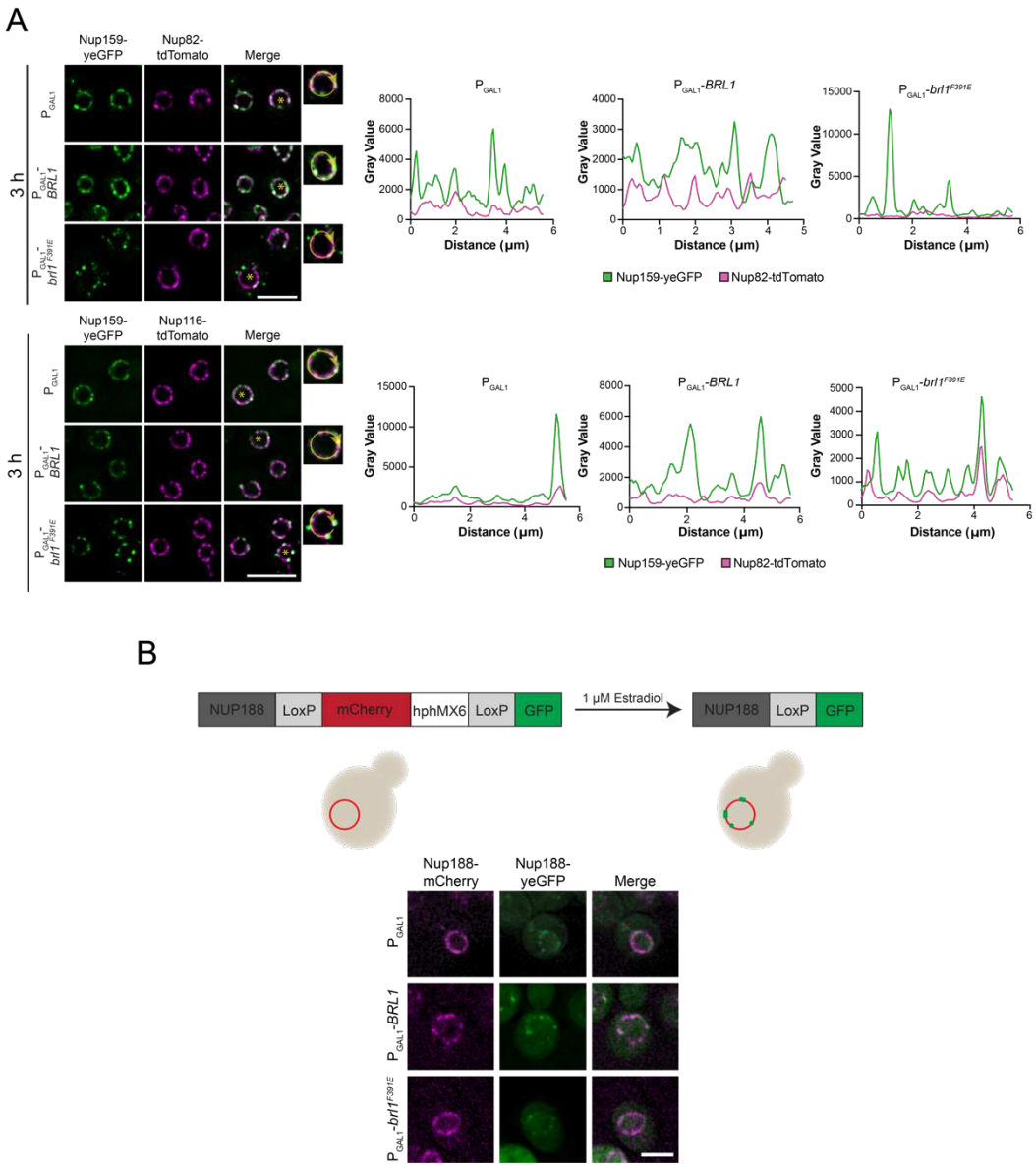

Figure 35. *brl1*^{F391E} over-expression affects a subset of nucleoporins. **(A)** Fluorescence images of cells expressing vector control, *BRL1* and *brl1*^{F391E} in cells with *NUP159-yeGFP, NUP82-tdTomato* and *NUP159-yeGFP, NUP116-tdTomato* backgrounds. Line scans of tdTomato and yeGFP signals of indicated cells. Scale bars: 5 μm. **(B)** Principle of the RITE assay (top). Fluorescence images of *NUP188-LoxP-mCherry-LoxP-yeGFP* cells carrying vector control, *BRL1* and *brl1*^{F391E}, 2 hours after galactose and estradiol induction (bottom). Scale bars: 5 μm.

Figure taken and adapted from (Vitale, Khan et al. 2022).

3.14 The petal-like structures are NPC assembly intermediates

Data from Figure 34 shows that certain Nups accumulate at the petal-like structures. This could mean that these structures are NPCs that failed to complete the assembly process possibly due to a fusion defect between the INM and ONM, necessary for the formation of a mature NPC, resulting in continuous expansion of the membranes. To test this, immuno-EM was performed to look at the localization of Nsp1 and Brl1-yeGFP. Results showed Nsp1 signal inside and at the base of the petal-like structures as well as Brl1^{F391E}-yeGFP localized to these structures, in line with published data that Brl1 associates with NPC assembly intermediates (Zhang, Neuner et al. 2018) (Figure 36A). To further validate the results, I used the MAB414 antibody that recognizes a subset of FG nucleoporins to look at the localization of Nups. Consistent with previous results, MAB414 antibody localized Nups to the base of the petal-like structures (Figure 36B), confirming the hypothesis that these structures are NPC assembly intermediates.

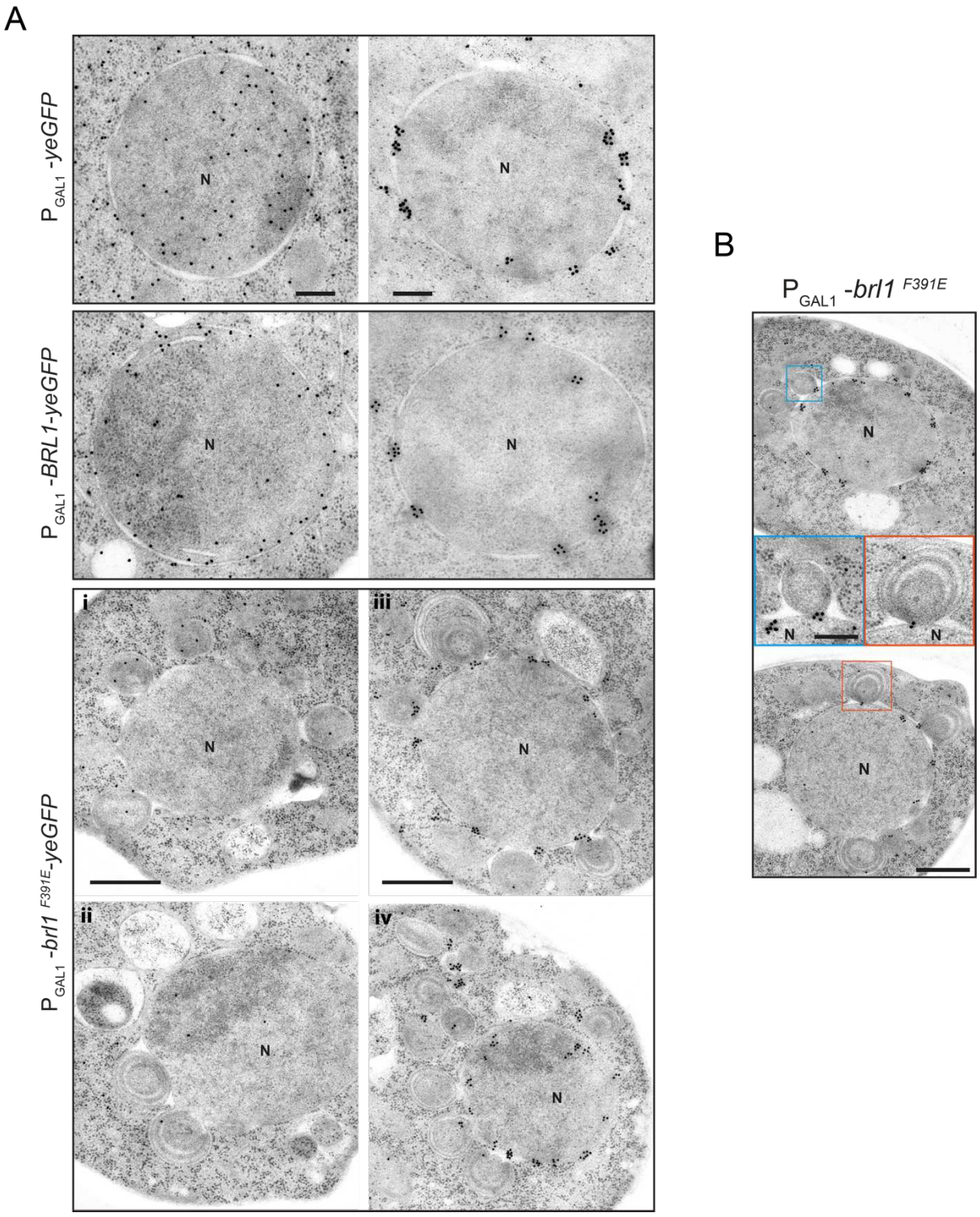

Figure 36. Nsp1 localizes to the petal-like structures. **(A)** Immuno-EM images of cells over-expressing vector control, *BRL1-yeGFP* and *brl1^{F391E}-yeGFP* for 3 hours and stained for anti-GFP (left) and anti-Nsp1 (right) antibodies. Scale bars: 500 nm. **(B)** Immuno-EM images of cells over-expressing *brl1^{F391E}* and stained for MAB414 antibody. Scale bars: 200 nm.

Figure taken and adapted from (Vitale, Khan et al. 2022).

“Multifunctional Role of Brr6 in nuclear pore complex biogenesis”

3.15 Brr6 has a role in the fusion of the NE

Brl1 shares structural and somewhat functional similarities with Brr6. Previous data has shown that Brr6 localizes to both the INM and ONM and a cold sensitive mutant *brr6-1* causes mislocalization of some nucleoporins and NE abnormalities (Hodge, Choudhary et al. 2010, Zhang, Neuner et al. 2018). Keeping these facts in mind, I wanted to further understand its function by anlayzing several randomly isolated *ts* mutants of Brr6. These mutants carried mutations in the perinuclear space region, including the cysteine residues, and the amphipathic helix (Figure 37A). EM analysis of these mutants incubated at hours for 37˚C revealed accumulation of a large number of herniations of varying sizes (Figure 37A), indicating a role of Brr6 in the fusion of INM and ONM.

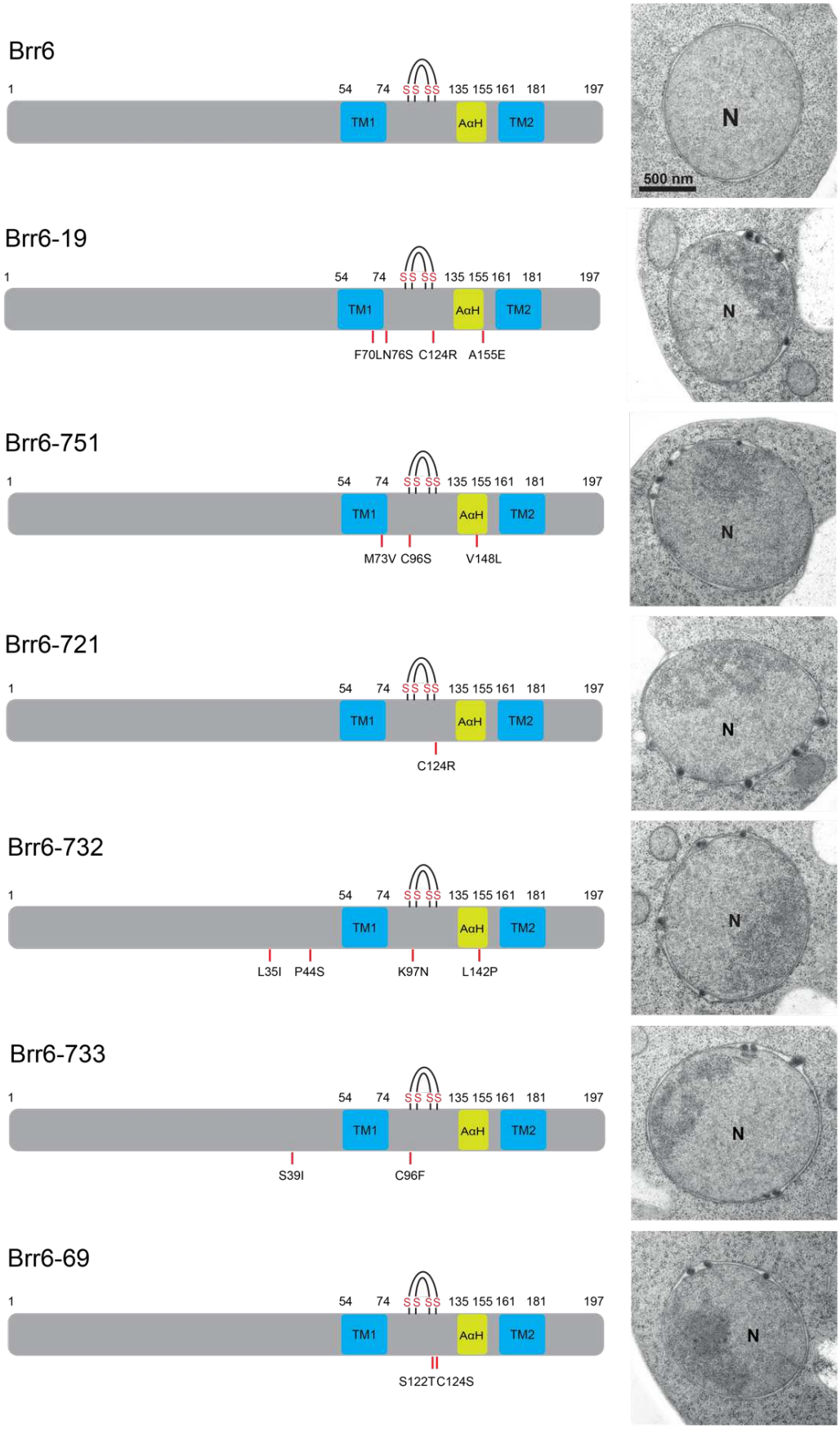

Figure 37. *brr6-ts* mutants with mutations in the PNS accumulate herniations. Electron micrographs of *BRR6* and different *brr6-ts* mutants (right) after 3 hour incubation at 37˚C. Scale bars: 500 nm. Schematic showing the mutations (left).

From previous work, it is known that *BRL1* over-expression is able to rescue the herniation phenotype of *nup116Δ* (Zhang, Neuner et al. 2018). However, it is not known whether the formation of herniations is a reversible process. To test this, I expressed *BRR6* under the *GALS* promoter in the *brr6-732* ts mutant, which accumulates herniations at restrictive temperature. In control cells, empty vector was expressed. Overnight cultures were shifted to 37˚C for 3 hours to induce herniations and then shifted back to 23˚C with the induction of *BRR6* expression for 4 hours (Figure 38A). Results showed that at 37˚C both the control and experimental sample showed similar number of herniations (Figure 38B-C). When shifted to 23˚C upon induction of expression, the cells expressing *BRR6* showed a significant decrease in the number of herniations compared to the vector control (Figure 38B-C). The vector control does show a slight decrease in the number of herniations at 23˚C, however this decrease is not significant. This indicates that *BRR6* can actively repair/reverse herniations.

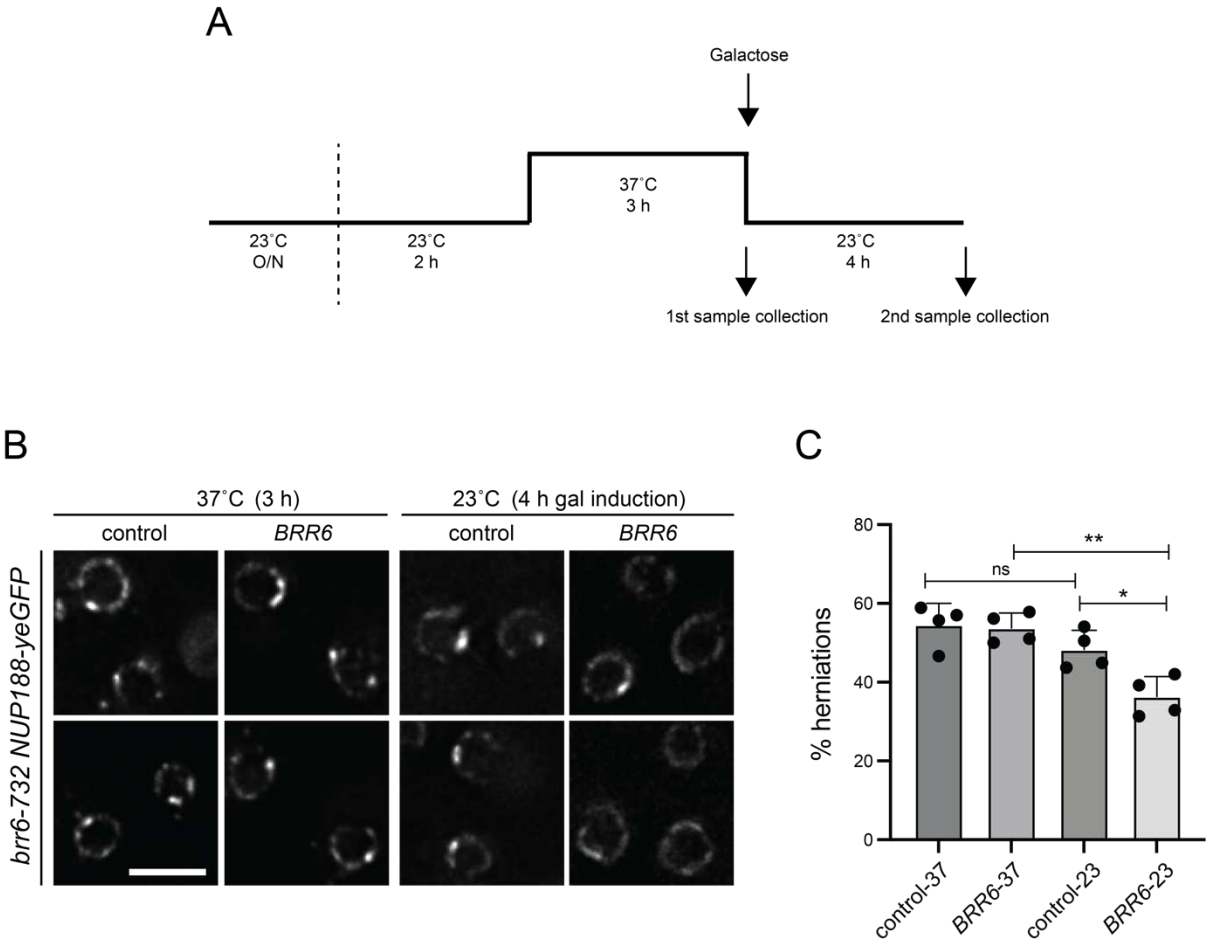

Figure 38. *BRR6* is able to repair herniations. **(A)** Timeline of the experimental strategy. **(B)** Fluorescence images of *brr6-732* ts-mutant carrying *NUP188-yeGFP* marker, incubated with indicated plasmids under the *GAL-S* promoter. Scale bar: 3 μm. **(C)** Quantification of herniations from (B). Data is presented as mean ± SD. n=4. Two-tailed t-test *p<0.05, **p<0.01, ***p<0.001, ****p<0.0001

3.16 Brr6 carries a membrane active AαH

As shown earlier, the domain organization of Brr6 is similar to Brl1. It contains 2 transmembrane domains that flank the perinuclear space region carrying an amphipathic helix (predicted by HeliQuest) and 2 disulfide bonds (Figure 39A-C). The AαH, when fused with yeGFP, localized to the NE and ER similar to full length Brr6 (Figure 39D). Upon introducing helix disrupting F152E mutation in the AαH, the fusion protein showed a severely reduced NE/ER staining and localized mostly to the cytoplasm and nucleus (Figure 39C-D).

I then tested whether the amphipathic helix is essential for the function of Brr6. Using a plasmid shuffle approach, I tested the viability of AαH point mutants L145E and F152E. The F152E mutant failed to grow on 5-FOA plates whereas the L145E mutant showed a growth defect compared to wildtype *BRR6* (Figure 39E).

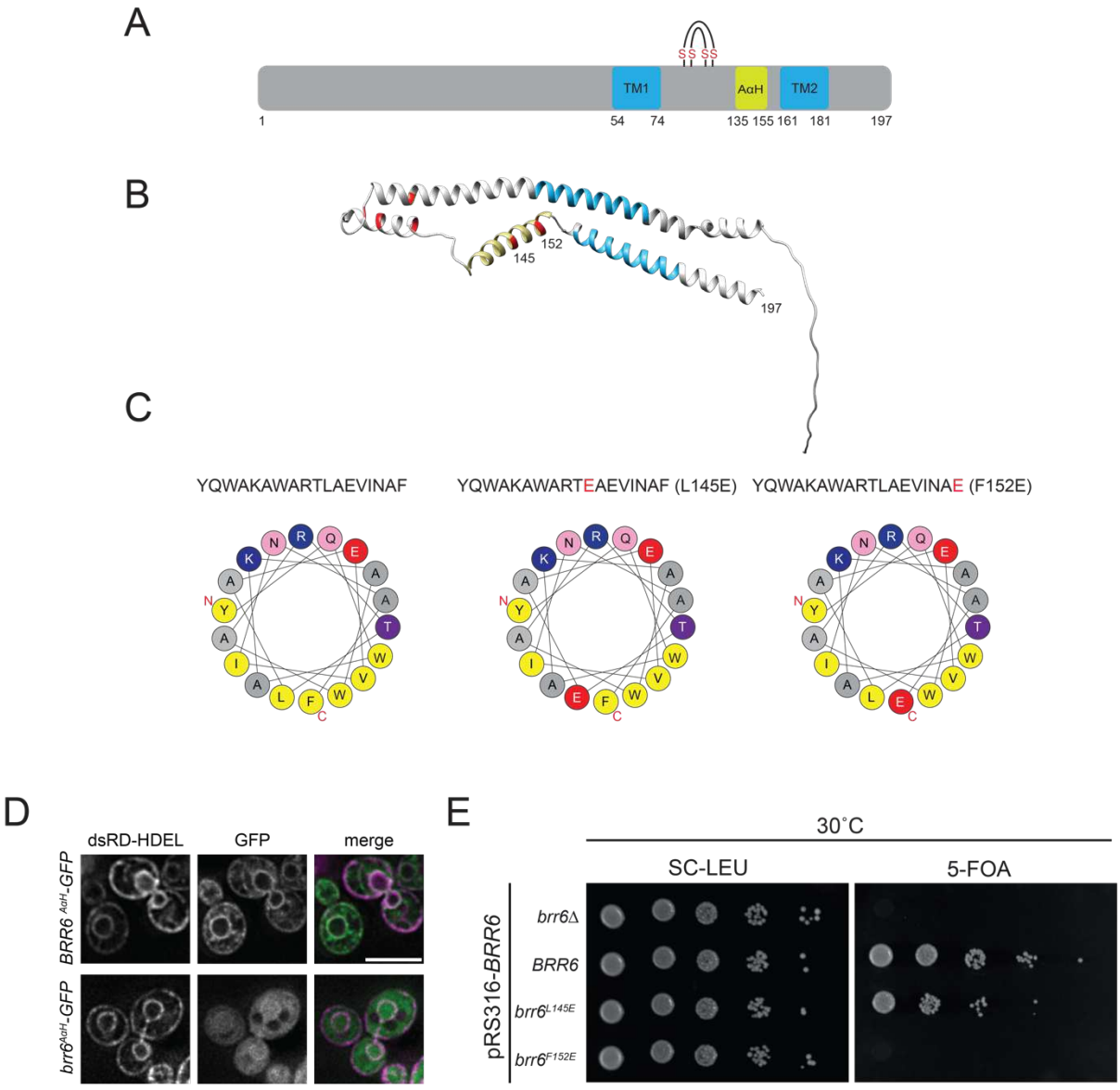

Figure 39. Membrane active Brr6 AαH is important for its function. **(A)** Domain organization of Brr6. Two TMs (blue), disulfide bonds (red) and AαH (green) are shown. **(B)** Predicted AlphaFold structure of Brr6. The amphipathic helix is in yellow, with point mutations highlighted in red. The four cysteine residues are also shown in red. **(C)** HeliQuest predictions of Brr6 AαH, Brr6^{L145E} AαH and Brr6^{F152E} AαH. **(D)** *BRR6-AαH-yeGFP and brr6^{L1454E}-AαH-yeGFP* expressed in *dsRED-HDEL* background. Scale bars: 5 µm. **(E)** Growth test of *BRR6*, *brr6^{L145E}*, and *brr6^{F152E}* using a plasmid shuffle approach. Tenfold serial dilutions were spotted onto SC-Leu and 5-FOA plates and incubated at 30˚C.

To analyze how over-expression of these mutants affects the cells, I over-expressed *brr6^{L145E}* and *brr6^{F152E}* under the *GAL1* promoter. Results showed that both the mutants are toxic for cells upon over-expression (Figure 40A). The control cells, carrying *BRR6*, grew well upon galactose induction. Upon co-overexpression of *BRR6* and *brr6^{L145E}*, the toxic effect was rescued which means that Brr6 competes with Brr6^{L145E} (Figure 40B). To analyze how these mutants localize and affect the NE/ER membranes, Brr6 and Brr6^{F152E} were tagged with yeGFP and over-expressed in cells carrying the dsRED-HDEL

membrane marker. Brr6^{F152E} displayed the same subcellular localization as Brr6 when over-expressed, and did not affect the NE and ER (Figure 40C).

These results show that Brr6 carries a membrane active AαH, important for its correct localization. Moreover, this helix is important for the function of Brr6 and mutations cause toxicity upon over-expression.

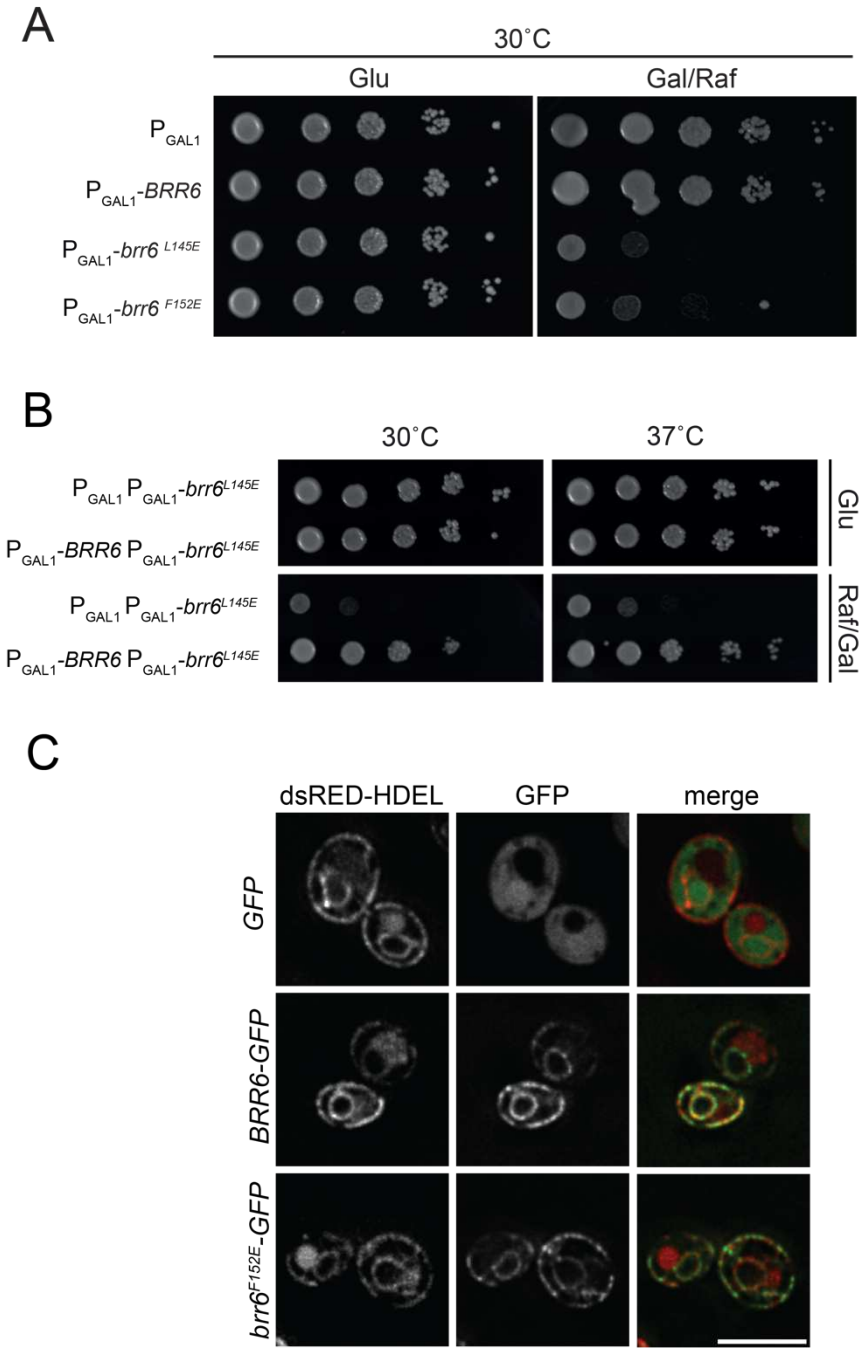

Figure 40. Over-expression of *BRR6* mutants is toxic. **(A)** WT cells with control plasmid or *BRR6*, *brr6^{L145E}* and *brr6^{F152E}* were spotted in 10-fold serial dilutions onto glucose (Glu) and galactose/raffinose (Gal/Raf) plates at 30°C. **(B)** Spot assay for growth of cells containing vector control and *brr6^{L145E}* or *BRR6* and *brr6^{L145E}* on glucose and galactose/raffinose plates. **(C)** Over-expression of *BRR6-yeGFP* and *brr6^{L145E}-yeGFP* in *dsRED-HDEL* background. Scale bar: 5 μm.

3.17 Incorporation of nucleoporins into NPCs requires Brr6 AαH

To look at how the NPCs are affected by mutations in Brr6, I over-expressed the *brr6*^{L145E} and *brr6*^{F152E} mutants under the *GAL1* promoter and looked at different fluorescently tagged nucleoporins. To control the experiment, Brr6 was also over-expressed. Results showed that for the majority of nucleoporins, their distribution was affected when *brr6*^{L145E} and *brr6*^{F152E} were over-expressed (Figure 41B-C). Instead of showing a smooth NE staining they accumulated in clusters on the NE and close to the NE, as can be seen in the case of Nsp1-tdTomato and Nup159-yeGFP. Notably, transmembrane nucleoporins, such as Ndc1, Pom152, and Pom34, remained unaffected (Figure 41B-C). Over-expression of *BRR6* did not affect the Nup localization. Line scan analysis of the fluorescent signals of representative Nups Nup159-yeGFP and Pom152-tdTomato also confirmed their observed distribution patterns (Figure 41C). Further quantification revealed at least 3 different groups of Nups based on the severity of the phenotype: strongly affected Nups including Nsp1, Nup82, Nup42, Nup159, Nup133, Nup60, Gle2 and Nup49, moderately affected Nups including Nup116, Gle1, Nup84, Nup120, Nic96, Nup85 and Nup170, and unaffected Nups including Nup2, Pom152, Ndc1 and Pom34. (Figure 41D). Notably, over-expression of the L145E mutant showed a much stronger phenotype than the F152E mutant.

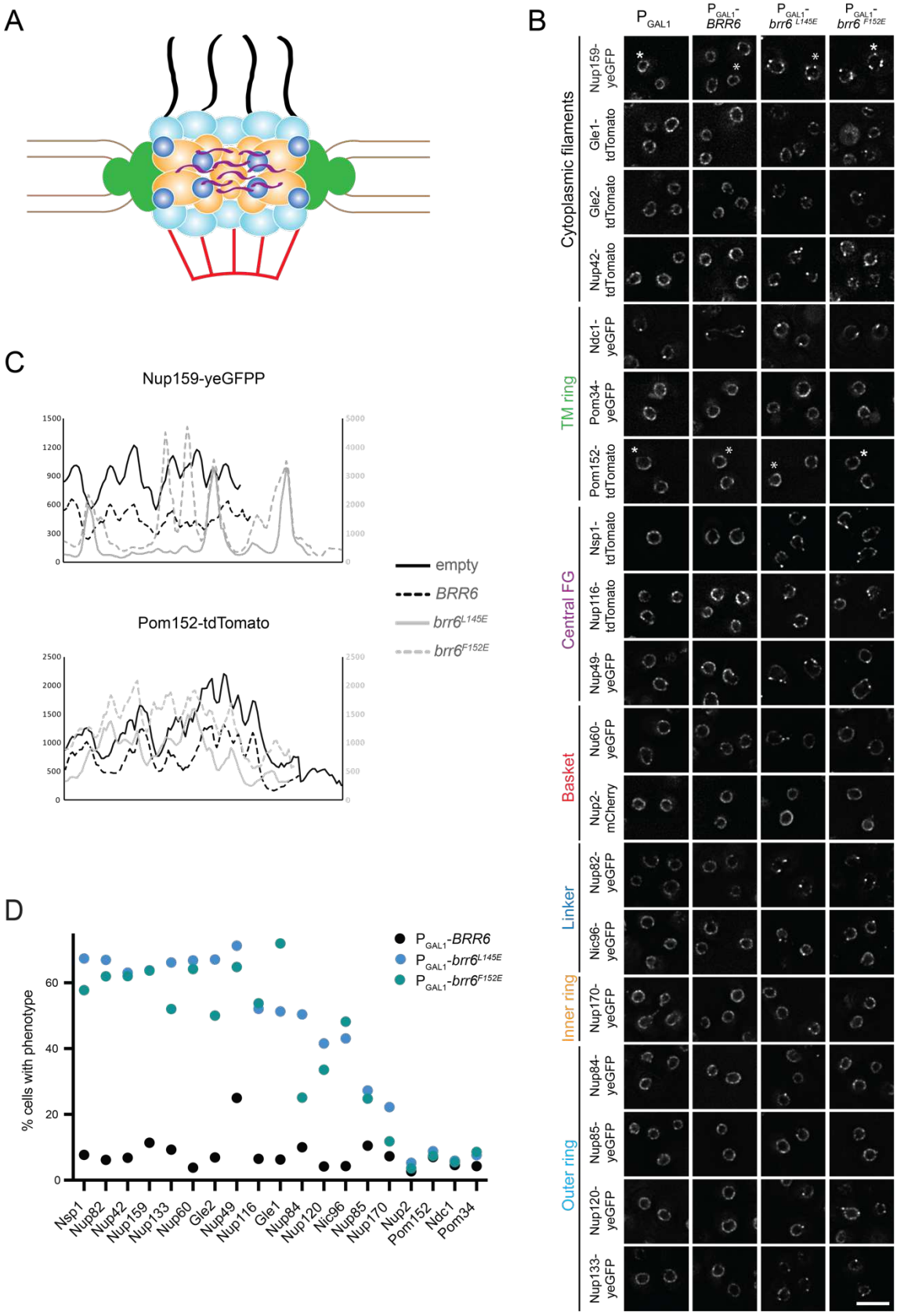

Figure 41. Overexpression of *brr6*^{L145E} affects localization of nucleoporins. **(A)** Schematic of an NPC embedded in the NE. **(B)** *BRR6*, *brr6*^{L145} and *brr6*^{F152E} were overexpressed for 3 h in cells carrying different fluorescently tagged components of the NPC. Scale bar: 5 µm. **(C)** Scans of Pom152-tdTomato and Nup159-yeGFP signals along the NE of cells with indicated plasmids. **(D)** Quantification of data from (B). More than 150 cells were counted for each sample.

Next, the over-expression phenotype of *brr6*^{L145E} and *brr6*^{F152E} was analyzed by immuno-EM using anti-Nsp1 antibodies as Nsp1 is one of the nucleoporins that is strongly affected. Unlike *brr6(ts)* and *brl1*$^{A\alpha H}$ mutants, no herniations were observed upon over-expression of the *brr6*^{L145E} mutant. Looking at the signal from the anti-Nsp1 antibody, two conclusions can be drawn. First, Overexpression of *brr6L145E* and *brr6F152E* mutants resulted in a predominantly INM-localized Nsp1 signal, unlike wildtype *BRR6* where the signal distributes equally between the INM and ONM (Figure 42A-B). Second, large accumulations of Nsp1 signal can be seen at NE, that are sometimes located outside the nucleus (Figure 42A-B). These results indicate that Brr6 AαH also has a role in proper recruitment and distribution of nucleoporins which is distinct from that of Brl1.

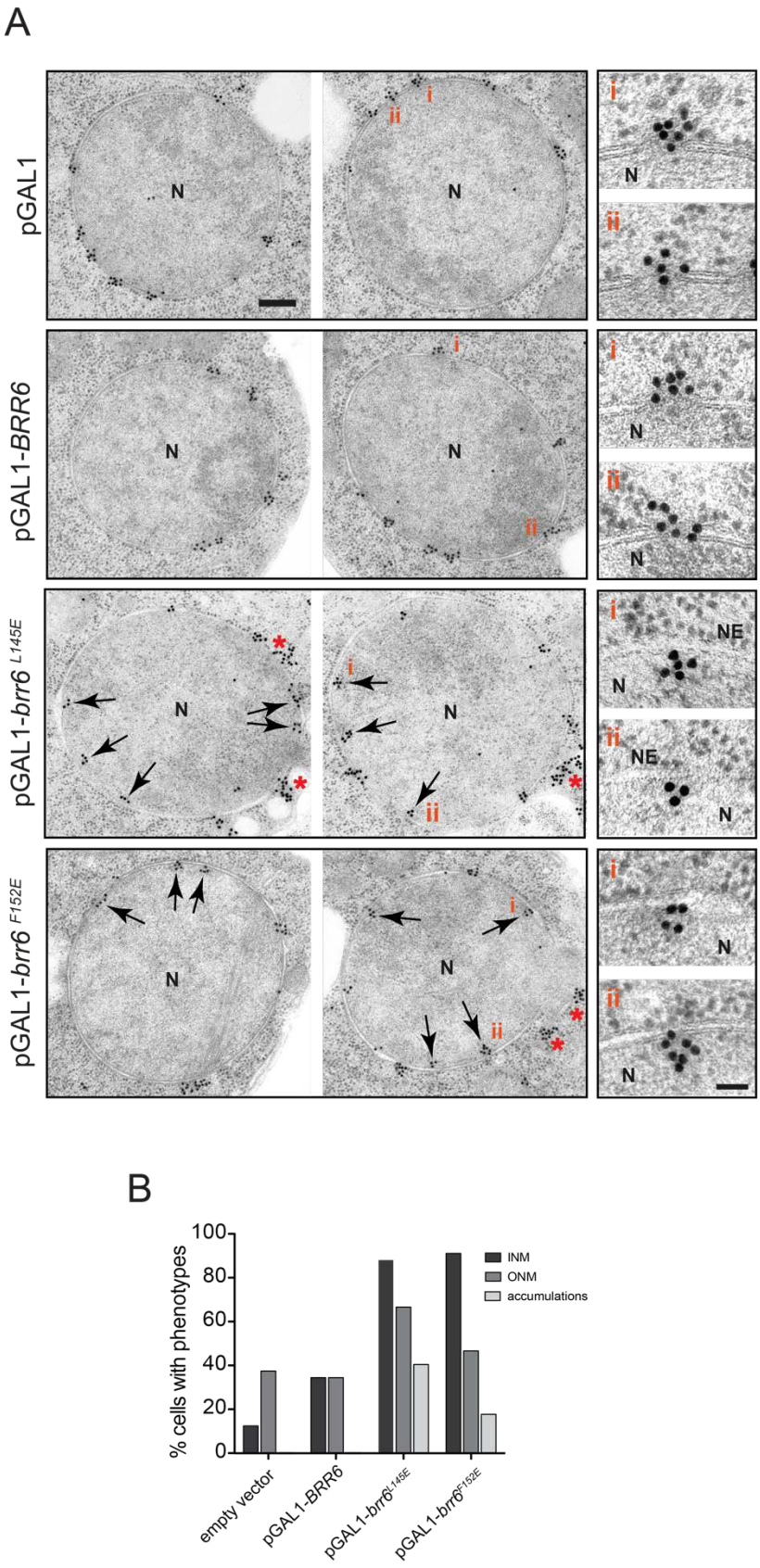

Figure 42. Nups accumulate into clusters upon *brr6*^{L145E} over-expression. **(A)** Immuno-electron micrographs of cells with indicated plasmids induced for 3 hours at 30˚C and stained with anti-Nsp1 antibodies. Scale bar: 200 nm. Magnifications are shown on right. Scale bar: 50 nm. **(B)** Quantification of the Nsp1 signal from (A).

3.18 Brr6 can compensate for the toxic effect of the mutant Brl1 AαH upon over-expression

Based on the data shown above, I speculated that the Brr6 AαH has a function earlier than the INM and ONM fusion. To further test this hypothesis, I co-overexpressed *BRR6* and *BRL1* mutants in different combinations. *brl1*^{F391E} over-expressed with the empty vector was toxic similar to *brl1*^{F391E} alone (Figure 43A). *brr6*^{L145E} was also toxic in combination with the empty vector much like *brr6*^{L145E} alone. However, *brl1*^{F391E} in combination with *BRR6* grew well like the control and interestingly, the two mutants *brl1*^{F391E} and *brr6*^{L145E} when co-overexpressed, also showed reduced toxicity compared to the single mutants (Figure 43A). To do a phenotypic analysis, I over-expressed these combinations in a *dsRED-HDEL* background. Both BRR6 and brr6L145E were able to suppress the formation of petal-like herniations (Figure 43B). Quantification also revealed a significant decrease in the phenotype upon over-expression of *brl1*^{F391E} and *brr6*^{L145E} together (Figure 43C).

This was further confirmed by EM analysis (Figure 43D-E). These findings indicate that Brr6 may have a role beyond nuclear envelope fusion, possibly in the earlier stages of NPC assembly or in maintaining NPC integrity.

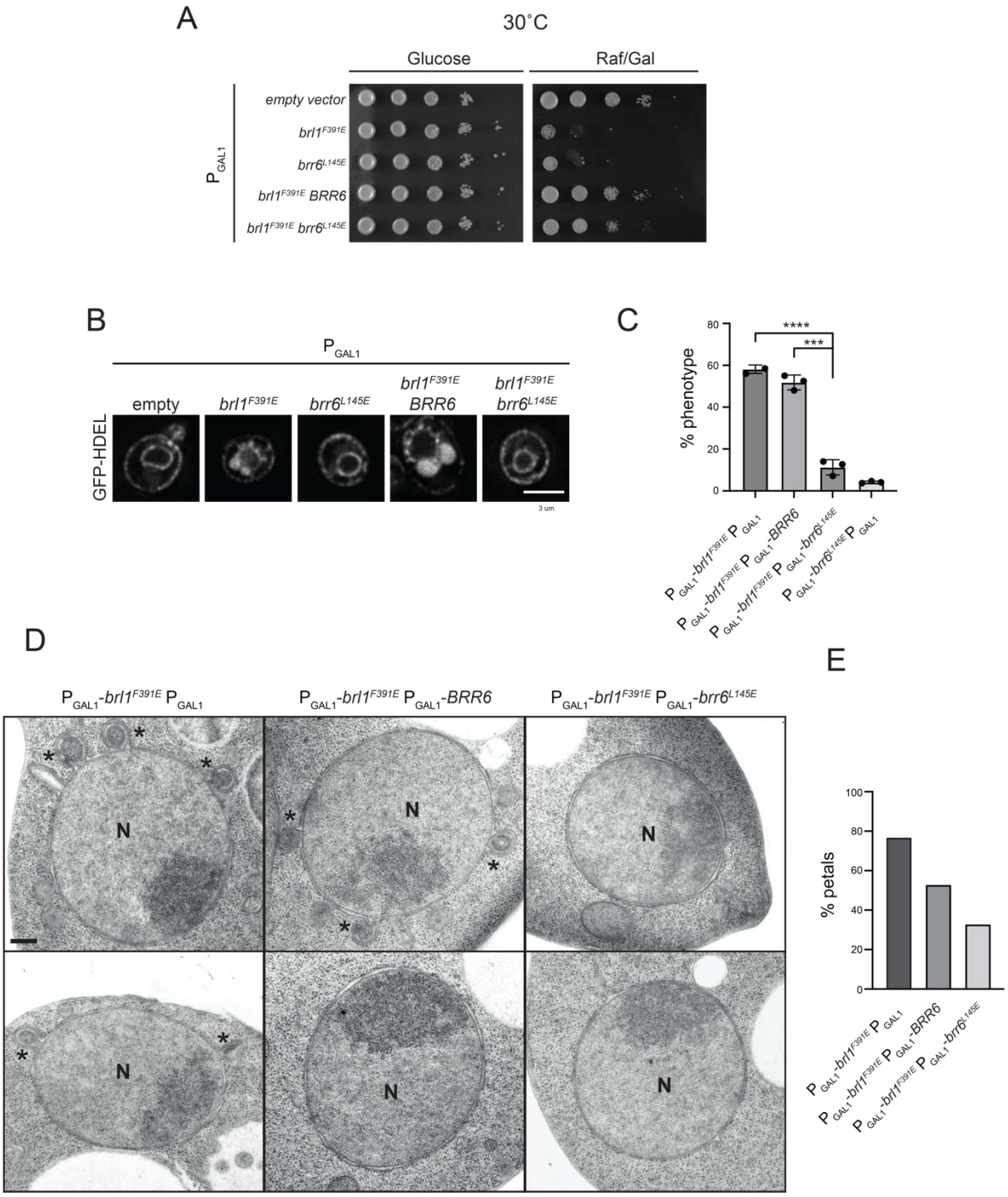

Figure 43. (A) Co-expression of the indicated plasmids in wildtype cells spotted on glucose and galactose/raffinose plates and incubated at 30˚C. **(B)** Fluorescence images of *dsRED-HDEL* cells carrying the indicated plasmids. Images taken 3 hours after induction with galactose at 30˚C. Scale bar: 3 µm. **(C)** Quantification of data from (B). n=3. Values are presented as means ± SD. Two-tailed t-test *p<0.05, **p<0.01, ***p<0.001, ****p<0.0001. **(D)** EM images of cells co-expressing the indicated plasmids for 3 hours at 30˚C. Scale bar: 200 nm. **(E)** Quantification performed on dataset from (D).

3.19 *brr6*^{L145E} impacts both the old and new NPCs

To look at whether *brr6*^{L145E} affects old NPCs or new NPCs, I used the RITE system for its ability to allow differentiation between old and new proteins. Nup82, Nup133, Nup159 and Pom152 were tagged with the RITE cassette. Expression of *brr6*^{L145E} and the Cre-recombinase was induced simultaneously by galactose and estradiol. Cell samples were analyzed by fluorescence microscopy 4 hours after the addition of galactose and estradiol. The analysis revealed that over-expression of *brr6*^{L145E} impacted not only the new GFP marked NPCs, but also the mCherry-labelled old or pre-existing NPCs including Nup133, Nup159 and Nup82 (Figure 44A). Line scan analysis confirmed colocalization of mCherry (existing NPCs) and GFP (newly synthesized NPCs) signals upon *brr6*^{L145E} overexpression, which was absent in control cells expressing *BRR6* or the empty vector . In contrast, when I analyzed Pom152, a nucleoporin that is not affected by *brr6*^{L145E} over-expression, no such correlation between the GFP and mCherry signals was observed (Figure 44A).

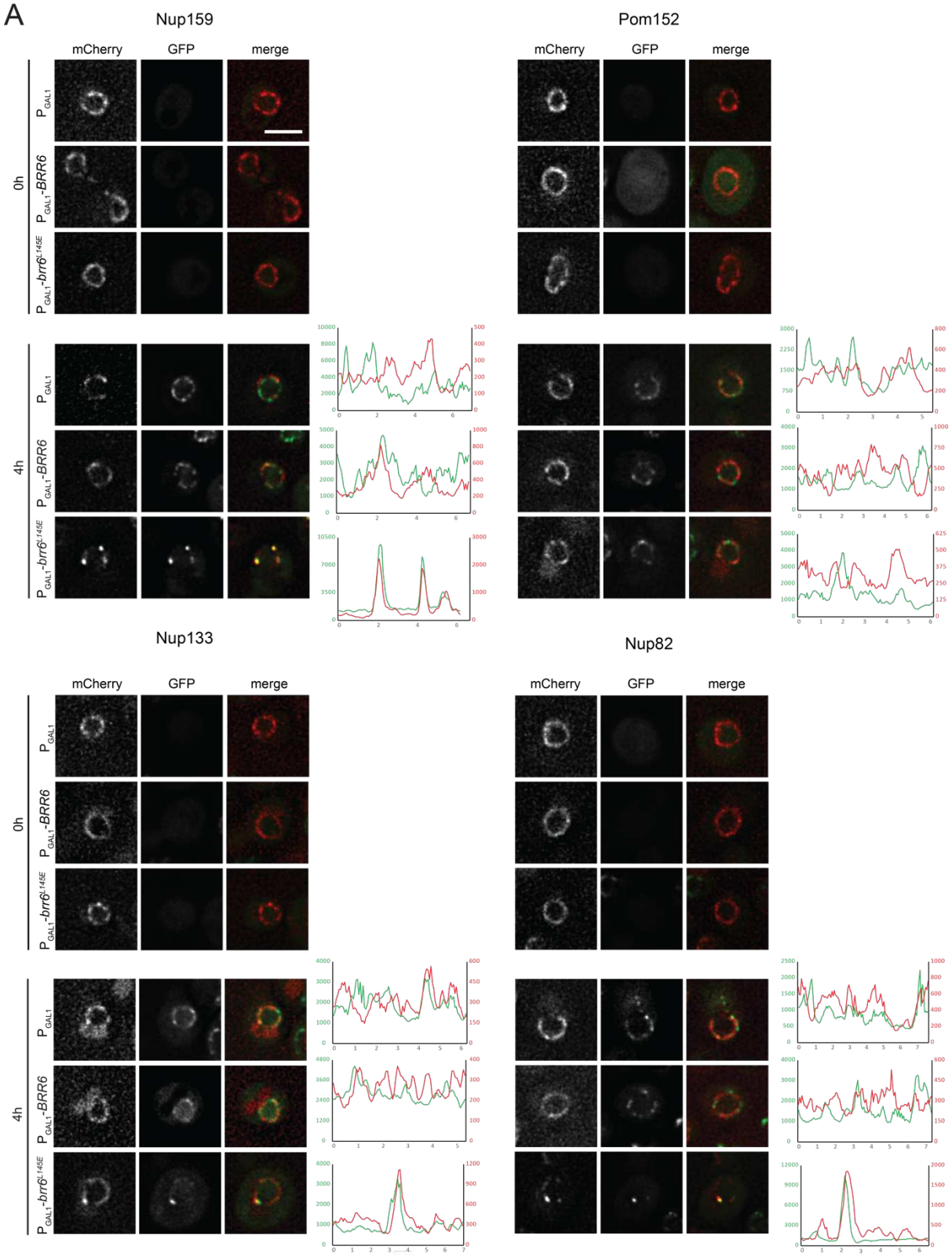

Figure 44. *brr6*^{L145E} affects both old and new NPCs. **(A)** Fluorescence microscopy images of cells with Nup159, Nup133, Pom152 and Nup82 tagged with the RITE cassette, taken at 0 and 4 hours after induction with galactose and estradiol. Scans of GFP and mCherry signals are shown on the left. Scale bar: 3 µm

3.20 *S. pombe* Brr6 is functionally equivalent to *S. cerevisiae* Brl1 & Brr6

S. pombe encodes a single Brl1/Brr6 homologue, spBrr6. spBrr6 has a sequence homology with *S. cerevisiae* Brl1 and Brr6 at the C-terminus, specifically in the PNS region as it contains 4 cysteines and an AαH (Saitoh, Ogawa et al. 2005). Previous research has shown that spBrr6 is able to compensate *BRL1* and *BRR6* deletions individually (Saitoh, Ogawa et al. 2005), however, whether it is able to compensate for *BRL1 BRR6* double deletion is not known.

First, I looked at the subcellular localization of spBrr6 by fusing it with yeGFP. Fluorescence microscopy showed that it localizes to the NE and ER similar to Brr6 and Brl1 (Figure 45A).

Next, I tested *spBRR6* in *brl1Δ* and *brr6Δ* strains by a plasmid shuffle approach. As reported before, *spBRR6* was able to rescue the lethal phenotype of *brl1Δ* and *brr6Δ* strains (Figure 45B). *BRL1* and *BRR6* were used as positive controls. I then used the plasmid shuffle approach in *brr6Δ brl1Δ* strain to check if *spBRR6* is able to complement the function of both Brr6 and Brl1 simultaneously. Results showed that spBrr6 was able to rescue the lethal phenotype of Brr6 and Brl1 double deletion (Figure 45C). This is noteworthy as it means that *S. pombe BRR6* evolved to carry the functions of both *BRL1* and *BRR6.*

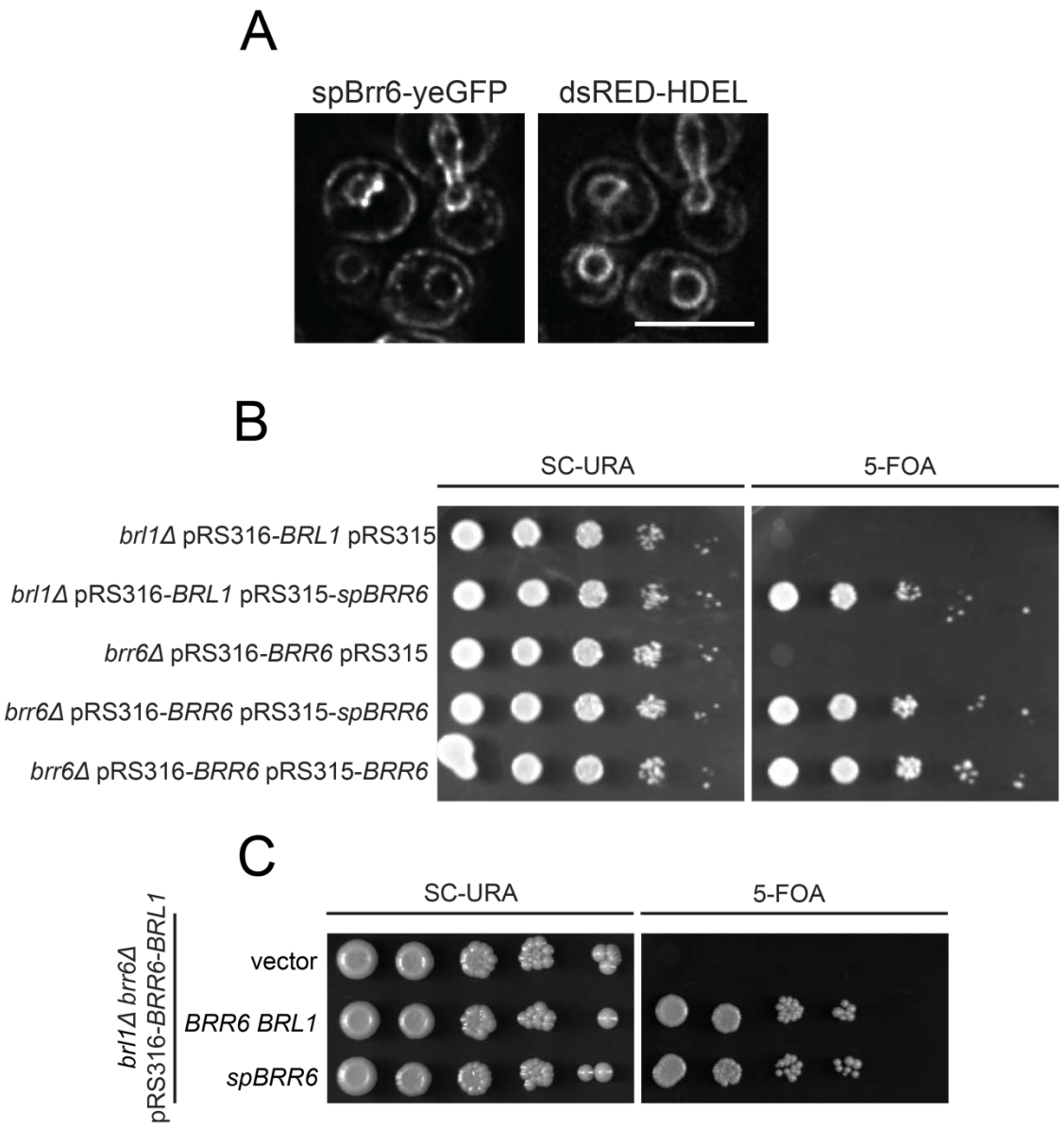

Figure 45. *S. pombe* Brr6 is functionally equivalent to *S. cerevisiae* Brl1 and Brr6. **(A)** *spBRR6-yeGFP* expressed in *dsRED-HDEL* background. Scale bar: Scale bar: 5 μm. **(B)** Growth assay for *spBRR6* using the plasmid shuffle approach. *BRR6* is used as a positive control. **(C)** Complementation assay of *spBRR6* in *brl1Δ brr6Δ* pRS316-*BRR6-BRL1* strain background.

4. Discussion

The nuclear pore complex stands out as one of the largest protein complexes within the cell, yet only a handful of non-NPC proteins have been linked to its biogenesis. Among these proteins are the integral membrane proteins Apq12, Brl1 and Brr6. However, the precise stage at which these proteins function in the process of NPC assembly, as well as the mechanism of their action, have remained unclear. In this study I analyze in detail their role in biogenesis by demonstrating that the Apq12-Brl1-Brr6 module is able to associate with assembly intermediates and has a potential role in membrane fusion.

Apq12 is a transmembrane protein that localizes to the NE and ER (Baker, Coller et al. 2004, Lone, Atkinson et al. 2015). It is known to be involved in mRNA transport, regulation of membrane dynamics and NPC assembly (Baker, Coller et al. 2004, Hodge, Choudhary et al. 2010, Lone, Atkinson et al. 2015). To understand how Apq12 is involved in NPC biogenesis, I started by analyzing its domain organization. It is a 138 a.a. long protein which carries two transmembrane domains (Figure 14). Given its lack of sequence similarity with proteins of known enzymatic activities, it is reasonable to assume that it functions either as a scaffold protein or as a membrane-shaping protein, akin to reticulons that deform the membrane through the presence of several transmembrane (TM) domains. Analysis of Apq12 by AmphipaSeek program predicted the presence of a short A*α*H flanked by its two TM domains (Figure 15). Further experiments revealed that this A*α*H resides in the perinuclear space of the nuclear envelope with its N and C-termini residing in the nucleus or cytoplasm. Moreover, a synthetic A*α*H peptide was able to bind to liposomes and this binding was dependent on its amphipathic nature. The fact that both Apq12 and Apq12-ah interact with Brl1 and Brr6 with the same efficiency indicates that integrity of the A*α*H is crucial for the overall function of Apq12. However, the mutation (*apq12-ah*) does not render it a loss-of-function allele, as evidenced by several phenotypic differences between *apq12Δ* and *apq12-ah*. For example, while *apq12Δ* exhibits NE invaginations and herniations at 16˚C, *apq12-ah* displays NE breakdown and NE extrusions as major phenotypes at the same temperature. Nonetheless, both mutants exhibit similar phenotypes, including cold sensitivity, herniations, and NE breakdown. Additionally, both mutants alter the cellular lipid composition such that the membrane fluidity is decreased. This explains why NE breakdown appears as a major defect at lower temperatures and potentially accounts for

the cold-sensitive growth defect of *apq12Δ* and *apq12-ah* mutants. Strikingly, over-expression of *APQ12* leads to significant over-proliferation of the NE, pointing towards its role in regulating membrane homeostasis. Moreover, a significant accumulation of PA was observed upon overexpression of Apq12 in an AαH-dependent manner. It remains unclear whether this accumulation results from increased PA synthesis or relocalization of existing PA. PA is known to accumulate at herniations (Thaller, Tong et al. 2021), however, the observation that overexpression of *APQ12* only leads to mislocalization of NPCs into regions lacking ONM over-proliferation, without causing NPC defects, suggests that PA accumulates at the NE independently of NPC integrity.

Previous studies have demonstrated that degron induced depletion of Brl1 and Brr6 leads to INM deformations or herniations, which represent NPCs that have failed to assemble properly (Zhang, Neuner et al. 2018). By inducing the depletion of Brr6 and Brl1 to generate these herniations or assembly intermediates, a notable enrichment of *APQ12* at these sites was observed, and this enrichment was found to be independent of a functional AαH. Consequently, it can be inferred that Apq12, in conjunction with Brl1 and Brr6, localizes to NPC assembly sites to facilitate biogenesis but does not interact with fully assembled mature NPCs. Consistent with this observation, Apq12 was observed to colocalize with only a subset of NPCs under wildtype conditions.

Brl1 and Brr6 are two paralogous proteins localized to NE and ER. While Brl1 primarily resides in the INM, Brr6 is distributed across both the INM and ONM (Zhang, Neuner et al. 2018). Similar to Apq12, Brr6 and Brl1 also carry an A*α*H between two TM domains. AlphaFold Protein structure database predictions of these two proteins identified an additional helix localized in the perinuclear space which is referred to as the DAH, stabilized by two disulfide bonds. These disulfide bonds are crucial for the function of these proteins, as mutating all four or the inner two cysteines in Brr6 and Brl1, respectively, results in cell death (Zhang, Neuner et al. 2018). Mutations in the outer cysteine of Brl1 or Brr6 results in a conditional lethal phenotype with the accumulation of herniations. Mutations in the predicted A*α*Hs of *BRL1* (*brl1*^{F391E}, *brl1*^{L402E}, *brl1*^{F391P}) and *BRR6* (*brr6*^{F152E}) that disrupt their amphipathic nature are lethal, indicating an essential role of the A*α*H for the function of these proteins.

Interestingly, over-expression of the *brl*^{F391E} mutants showed not only a growth defect but also resulted in the formation of a novel-type of herniation; petal-like structures. These structures are significantly larger than conventional herniations and appear to

contain multiple elongated INM sheets stacked upon each other. Further, proper incorporation of cytoplasmic Nups (Nsp1, Nup42, Nup159) is also affected upon over-expression of *brl1*^{F391E}. However, it is clear that NPC assembly itself is not blocked as can be seen by the proper localization of Nup188 core Nup. These results have been validated in a similar study in which kinetic analysis of incorporation rates of macromolecular assemblies (KARMA) approach identified Brl1 as an assembly factor involved in the fusion of INM and ONM during the interphase assembly pathway (Kralt, Wojtynek et al. 2022).

Depletion of Brl1 is known to lead to the formation of herniations containing all major nups, such as those from the inner ring, middle ring, Y-complex, and basket, with the exception of the cytoplasmic nups, which exhibit mislocalization similar to other reported assembly mutants (Scarcelli, Hodge et al. 2007, Makio, Stanton et al. 2009, Onischenko, Stanton et al. 2009, Hodge, Choudhary et al. 2010, Onischenko, Tang et al. 2017, Kralt, Wojtynek et al. 2022). Keeping this in mind it seems that the fusion of the INM and ONM must occur before the cytoplasmic Nups like Nup159 and Nsp1 can be recruited. Therefore, my findings align with an inside-out mode of interphase NPC assembly, consistent with earlier observations (Wente and Blobel 1993, Murphy, Watkins et al. 1996, Zabel, Doye et al. 1996, Makio, Stanton et al. 2009, Otsuka, Bui et al. 2016)

In the case of Brr6, its *brr6*^{L145E} mutant does not cause deformation of the NE upon over-expression, as is the case with *brl1*^{F391E} mutant, but it does lead to mislocalization of a number of nucleoporins. Among the Nups that did not show any mislocalization, most belong to the family of transmembrane Nups such as Pom152, Pom34, and Ndc1. Detailed analysis showed that not only is there a tendency for Nups to localize more at the INM compared to the ONM, but there also appear to be Nups outside the nucleus in clusters/patches. My data further shows that while NPC assembly is not blocked, Nups at both the old and new NPCs are affected upon the over-expression of *brr6*^{L145E}. This suggests that in addition to membrane fusion, Brr6 may also function in maintaining proper localization of the nucleoporins.

One aspect of assembly that is still unclear is how the cell deals with defective NPCs. Is there a possibility of repair of these herniations or are there mechanisms in place that remove or clear these defective NPCs? There is evidence that the cells have surveillance mechanisms that clear defective NPCs. A recent study showed that the INM protein Heh2

acts as a sensor of NPC assembly state by interacting with the scaffold Nups of the outer ring complex (Borah, Thaller et al. 2021). It recruits the AAA-ATPase Vps4 and Snf7 subunit of the endosomal sorting complex required for transport (ESCRT)-III to clear defective NPCs via proteasome degradation. In the absence of this surveillance machinery the herniations or defective NPCs accumulate in a storage of improperly assembled NPCs compartment (SINC) which is retained in the mother cells to ensure there is no loss of daughter lifespan (Webster, Colombi et al. 2014).

However, the question of repair is a bit more complex to address. It is known that over-expression of *BRL1* can suppress the growth defect of *nup116Δ* (Zhang, Neuner et al. 2018). What we don't know is that whether this rescue is due to repair or clearance of herniations. My data shows that herniations induced at restrictive temperature in *brr6-732* ts-mutant are significantly reduced upon expression of *BRR6* compared to the control (Figure 38). This result argues that the formation of herniations is probably not an irreversible process and that they can be actively repaired. However, it is also possible that this repair process depends on the size or age of the herniations; smaller newly formed herniations are likely easier and more likely to be repaired compared to larger, mature herniations.

Interestingly, the growth defect of $brl1^{F391E}$ over-expression is rescued by over-expression of *BRR6*, in an AαH dependent manner. This is interesting because both *BRL1* and *BRR6* are essential genes and are not able to complement each other (Saitoh, Ogawa et al. 2005). Similarly, the petal-like phenotype of $brl1^{F391E}$ is significantly suppressed upon over-expression of *BRR6* and $brr6^{L145E}$. It potentially means that $brr6^{L145E}$ is a dominant allele, however how it suppresses the herniation phenotype of $brl1^{F391E}$ over-expression is still unclear. It is possible that high enough concentrations of Brr6 or $Brr6^{L145E}$ suppress the phenotype of $Brl1^{F391E}$ in a manner that involves its N and C-termini and not an intact AαH.

It is noteworthy however, that over-expression of *BRL1* but not *BRR6* suppresses the herniation phenotype of *nup116Δ* and *gle2Δ* (Zhang, Neuner et al. 2018). In fact, BRR6 over-expression is toxic in *nup116Δ*. Moreover, the fact that deletion of *BRL1* and *BRR6* cannot be rescued by *BRR6* and *BRL1*, respectively (Saitoh, Ogawa et al. 2005), despite showing sequence and structural similarities, hints at the fact that Brl1 and Brr6 do not act in a redundant manner and have different functions during NPC assembly. This is in accordance with my data which shows that $brl1^{F391E}$ over-expression forms herniations,

whereas over-expression of *brr6*^{L145E} leads to mislocalization of Nups, and the differential localization of *BRL1* and *BRR6.*

To form mature NPCs, major deformation of the NE, including the formation of convex and concave curvatures, is necessary, which can create a dome shaped bend in the INM. AαHs are known motifs that bind to lipids and act by both sensing and generating membrane curvatures.

Proteins containing intrinsically disordered domains have been documented to undergo liquid-liquid phase separation, causing membrane deformations (Kusumaatmaja, May et al. 2021, Yuan, Alimohamadi et al. 2021). FG nucleoporins carry intrinsically disordered regions that form a sieve-like FG-hydrogel or "selective phase" (Frey and Görlich 2009) potentially serving as triggers for initiating membrane deformation (Frey and Görlich 2007, Milles and Lemke 2011). This process may be facilitated by the accumulation of PA at assembly sites due to Apq12 enrichment. PA, with its conical shape, renders membranes more susceptible to deformation by proteins (Jang, Lee et al. 2012, Tanguy, Kassas et al. 2018, Zhukovsky, Filograna et al. 2019). Recently, Chm7, an ESCRT-III protein, was reported to have PA binding activity (Thaller, Tong et al. 2021), suggesting the potential existence of PA binding sites in other NPC proteins. This could result in the recruitment of Brl1 and Brr6 to these assembly sites, supported by the co-immunoprecipitation of both proteins with Apq12 (Lone, Atkinson et al. 2015). The exact mechanism of recruitment remains unclear; however, it can be speculated that the three proteins of the Apq12-Brl1-Brr6 module act as sensors of membrane fluidity, given their implication in membrane homeostasis (Lone, Atkinson et al. 2015). My data supports the hypothesis that Brl1 and Brr6 are involved in fusion of the INM and ONM via their amphipathic helices, from the INM and ONM, respectively. Both proteins sense the curved or deformed membrane at assembly sites via their amphipathic helices. Once adequately enriched, the disulfide-bond-stabilized DAHs of Brl1 and Brr6 could span the approximately 20 nm perinuclear space, bringing the INM and ONM together and facilitating fusion mediated by the AαHs (Figure 47A). This model is also supported by AlphaFold predictions of the two proteins (Figure 46).

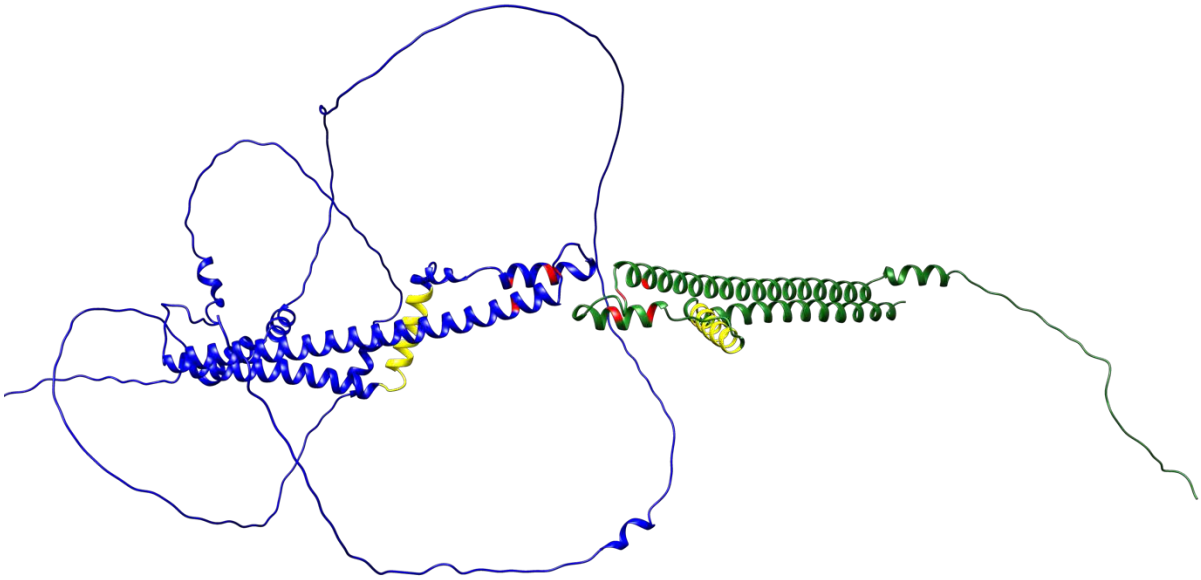

Figure 46. AlphaFold prediction of the Brl1 (blue) and Brr6 (green) interaction. Amphipathic helices are shown in yellow and cysteine residues in red. Provided by Dr. Martin Würtz.

Mutant amphipathic helices fail to correctly localize the proteins to the assembly sites, as evident from my data, which shows significantly reduced binding to the NE/ER. Consequently, this abolishes the ability of the Brl1 and Brr6 DAHs to span the perinuclear space and interact, thereby preventing the fusion of the two bilayers (Figure 47B). In agreement with this model, temperature-sensitive mutants of *BRL1* and *BRR6*, with mutations in the cysteine residues or the perinuclear space regions, exhibit herniations at restrictive temperatures.

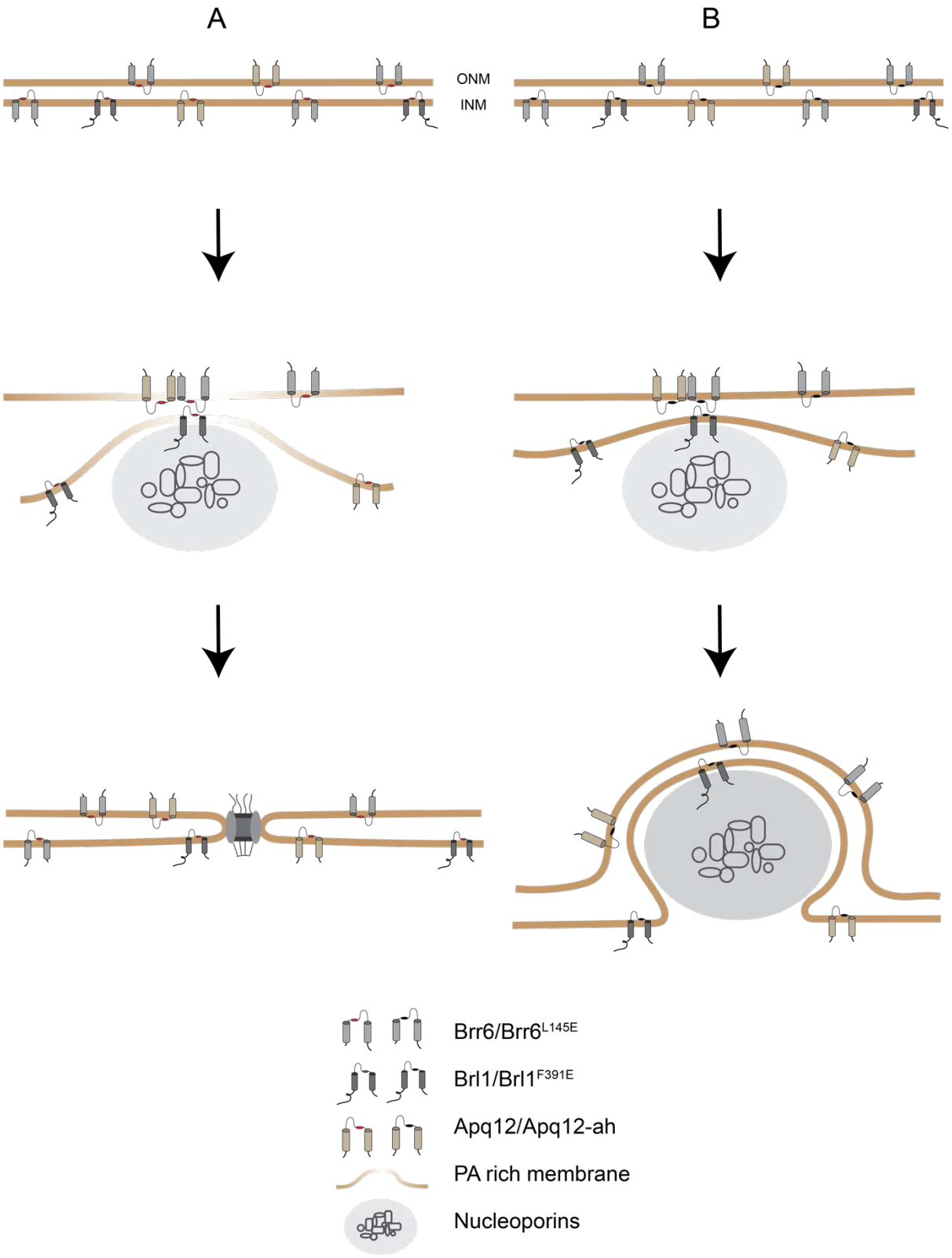

Figure 47. Model showing the role of Apq12-Brl1-Brr6 in membrane fusion (A), and the consequences of amphipathic helix mutations (B) during NPC assembly in the interphase pathway.

5. Conclusion & Outlook

The Apq12-Brl1-Brr6 module is conserved solely in organisms undergoing closed mitosis (Tamm, Grallert et al. 2011). However, given the straightforward domain organization of these proteins, featuring two TM domains and a short AαH, it is plausible that proteins with similar architecture could fulfill their function in higher eukaryotes without exhibiting amino acid homology. Brl1 and Brr6 possess an extended perinuclear space domain stabilized by two crucial disulfide bridges (Tamm, Grallert et al. 2011, Zhang, Neuner et al. 2018), suggesting that alternative structural features may substitute for this stabilization principle in equivalent proteins in higher eukaryotes. Understanding the principles and structural elements in yeast, a model organism, will aid in identifying vertebrate proteins that facilitate NE fusion during interphase NPC assembly.

To further investigate the hypothesis that the DAHs of Brl1 and Brr6 bring the IMN and ONM closer for fusion, it will be crucial to conduct immunoprecipitation studies of Brl1 and Brr6 using DAH mutants. Additionally, to elucidate the exact mechanism of this fusion, analyzing the interactors of Apq12, Brl1, and Brr6 is essential. Proximity-dependent biotinylation coupled with mass spectrometry (PDB-MS), a technique employing a version of the BirA biotin ligase called TurboID (Larochelle, Bergeron et al. 2019), can unveil the interaction landscape of Apq12, Brl1, and Brr6 during the assembly process. Purifying TAP-tagged Nups from Brl1 and Brr6 mutants can also provide insight into differential interactions. The membrane curvature and lipid composition of developing INM invaginations during NPC assembly could be crucial factors in recruiting Apq12, Brl1, and Brr6 to developing NPCs. Therefore, understanding the lipid-binding properties of these proteins will unravel their roles in NE fusion. To further corroborate the fusion function of Brl1 and Brr6, *in vitro* assays such as liposome binding can be employed. Decorating two liposome populations with purified recombinant Brl1 and Brr6 or their sub-domains to check for aggregation or deformation of liposomes will strengthen this hypothesis. Moreover, investigating the effect of different lipids on the binding properties of these proteins will shed light on the importance of membrane regulation during biogenesis. Furthermore, detailed comparative analysis between Brl1 and Brr6 and their *S. pombe* equivalent Brr6 can provide additional insights into how these proteins function.

6. Materials & Methods

6.1 Materials

6.1.1 Chemicals

All chemicals used in this study were purchased from Sigma-Aldrich, Thermo Fisher Scientific, Merck, AppliChem and Roth unless otherwise specified.

6.1.2 Media & Plates

Amino acid mix for Uracil, Leucine, Tryptophan and Histidine autotrophies

5 g Adenine
2 g Para-aminobenzoic acid
2 g each Alanine, Arginine, Asparagine, Aspartic acid, Cysteine, Glutamine, Glutamic acid, Glycine, Inositol, Isoleucine, Lysine, Methionine, Phenylalanine, Proline, Serine, Threonine, Tyrosine ang Valine

Drop-out mix selective for one or more auxotrophic markers

36.7 g amino acid mix
2 g Histidine
4 g Leucine
2 g Uracil
2 g Tryptophan

LB medium/plates

10 g Bacto-typtone (Difco)
10 g NaCl
5 g Bacto-yeast extract (Difco)
15 g Bacto-Agar (Difco) (for plates)
ddH_2O up to 1 L-autoclave

2X YT medium

16 g Bacto-typtone (Difco)
10 g NaCl
5 g Bacto-yeast extract (Difco)
ddH_2O up to 1 L-autoclave

YPAD medium

10 g Bacto-yeast extract (Difco)
20 g Bacto-peptone
20 g glucose
100 mg adenine
ddH_2O up to 1 L- autoclave

YPD medium/plates

10 g Bacto-yeast extract (Difco)
20 g Bacto-peptone
20 g glucose
20 g Bacto-Agar (Difco) (for plates)
ddH_2O up to 1 L-autoclave

YP-Raf medium

10 g Bacto-yeast extract (Difco)
20 g Bacto-peptone
20 g raffinose
ddH_2O up to 1 L-filter sterilize

YP-Raf/Gal plates

10 g Bacto-yeast extract (Difco)
20 g Bacto-peptone
ddH_2O up to 400 mL-autoclave
100 mL filter-sterilized 30% raffinose and 20% galactose solution
20 g Bacto-agar (Difco) in 500 mL ddH_2O-autoclave
Cool to 60°C, combine and pour

SC-medium

6.7 g Bacto-yeast nitrogen base w/o amino acids (Difco)
2 g drop-out mix
20 g glucose
ddH_2O up to 1 L-filter sterilize

SC-plates

6.7 g Bacto-yeast nitrogen base w/o amino acids (Difco)
2 g drop-out mix
20 g glucose
ddH_2O up to 500 mL-filter sterilize
20 g Bacto-agar (Difco) in 500 mL ddH_2O-autoclave
Cool to 60˚C, combine and pour

SC-Raf medium

6.7 g Bacto-yeast nitrogen base w/o amino acids (Difco)
2 g drop-out mix
20 g raffinose
ddH_2O up to 1 L-filter sterilize

SC-Raf/Gal plates

6.7 g Bacto-yeast nitrogen base w/o amino acids (Difco)
2 g drop-out mix
ddH_2O up to 400 mL-filter sterilize
100 mL filter-sterilized 30% raffinose and 20% galactose solution
20 g Bacto-agar (Difco) in 500 mL ddH_2O-autoclave
Cool to 60°C, combine and pour

5-FOA plates

6.7 g Bacto-yeast nitrogen base w/o amino acids (Difco)
2 g SC-Ura drop-out mix
0.1 g Uracil
1 g 5-FOA
20 g glucose
ddH_2O up to 500 mL-filter sterilize
20 g Bacto-agar (Difco) in 500 mL ddH_2O-autoclave
Cool to 60˚C, combine and pour

0.1 M CuSO4

2.5 g $CuSO_4$ powder
ddH_2O up to 100 mL-autoclave
Store in a cool dark place
Dilute 1:1000 for plates and media

Antibiotics

Ampicillin: 100 μg/mL
Kanamycin: 50 μg/mL
Chloramphenicol: 20 μg/mL
Geneticidinsulfate (Biochrome): 200 μg/mL
Hygromycin B (Cayla): 300 μg/mL
Noutseothricin (Werner BioAgents): 100 μg/mL

6.1.3 Buffers & Solutions

Yeast colony PCR lysis buffer

0.18 g D-Sorbitol
200 μL 50 mM Sodium phosphate buffer pH 8.0
40 μL Lyticase
ddH_2O up to 1000 μL

10X HiFi buffer

200 mM Tris-Cl pH 8.8
100 mM $(NH_4)_2SO_4$
100 mM KCl
1% Triton X-100
1 mg/mL BSA

10X Taq Bujard buffer

500 mM KCl
100 mM Tris-Cl pH 9.0
1% Triton X-100
15 mM $MgCl_2$

HU buffer

8 M Urea
200 mM Tris-Cl pH6.8
5% SDS
0.1 mM EDTA
0.5% Bromophenol blue
30 mM DTT (added just before use)
Store at -20˚C

Laemmli Buffer

50 mM Tris-Cl pH 7.0
2% SDS
10% Glycerol
0.02 % Bromophenol blue
100 mM DTT

6X DNA loading dye

0.25% Bromphenol blue (w/v)
0.25% Xylen cyanol (w/v)
30% Glycerol

50X TAE buffer

1 M Tris-Cl pH7.7
50 mM EDTA

10X SDS buffer

250 mM Tris
1.92 M Glycine
1% SDS

10X PBS

137 mM NaCl 2.7 mM KCl
10 mM Na_2HPO_4
Adjust pH to 7.4

10X TBS

200 mM Tris
1.5 M NaCl
Adjust to pH 8.0

TBS-T

1X TBS + 0.1 % Tween 20

Blocking buffer

2% milk powder in TBS-T

Blotting buffer

25 mM Tris-Cl
192 mM glycine
20% methanol (added fresh)

Coomassie Blue staining solution

70 g Coomassie brilliant blue
35 mM HCl
ddH_2O up to 1 L

LiSorb solution

91 g Sorbitol
2 mL 250 mM EDTA pH 8.0
5 mL 1 M Tris-Cl pH 8.0
5.1 g Lithium acetate
ddH_2O up to 500 mL-filter-sterilized

LiPEG solution

20 g PEG 3350
200 µL 250 mM EDTA pH 8.0
0.5 mL 1 M Tris-Cl pH 8.0
0.51 g Lithium acetate
ddH_2O up to 500 mL-filter-sterilized
Keep at 4°C

6.1.4 Antibodies

Name	Species	Dilution	Source
Anti-6*His	Mouse	1:1000	ProteinTech
Anti-Brl1	Rabbit	1:1000	Schiebel Lab
Anti-HA	Rabbit	1:500	Protein-Tech
Anti-GFP	Rabbit	1:1000	ProteinTech
Anti-GFP	Rabbit	1:5 (immuno-EM)	Seedorf Lab
Anti-Nsp1	Mouse	1:100 (immuno-EM)	Abcam
Anti-MAB414	Mouse	1:100 (immuno-EM)	Abcam
Anti-Tub2	Rabbit	1:1000	Schiebel Lab
Anti-streptavidin-HRP		1:1000	Schiebel Lab
Anti-mouse-HRP	Donkey	1:5000	Jackson
Anti-rabbit-HRP	Donkey	1:5000	Jackson

6.1.5 Primers

All primer pairs were designed depending upon the particular application. For endogenous gene tagging and deletions, S1-S4 primers were designed as described in (Janke, Magiera et al. 2004). For HiFi assembly primers were designed using the NEBuilder tool (https://nebuilder.neb.com/#!/).

6.1.6 Plasmids

Name	Description	Source
pSJ1321	*pRS315-NOP1pr-GFP$_{11}$-mCherry-PUS1*	(Smoyer, Katta et al. 2016)
pSJ1568	*pRS315-NOP1pr-GFP$_{11}$-mCherry-SCS2TM*	(Smoyer, Katta et al. 2016)
pSJ1256	*pFA6-link-yGFP1–10-CaURA3MX*	(Smoyer, Katta et al. 2016)
pSJ1643	*pFA6-NATMX-CDC42pr-yGFP1–10*	(Smoyer, Katta et al. 2016)
pZW111	*P426GAL1-APQ12-6HIS*	This study
pZW112	*P425GAL1-apq12-ah-6HIS*	This study
	pRS316-CYC1pr-NUP50(1-24)-OPI1	(Romanauska and Köhler 2018)
	pRS316-CYC1prom-OPI1 Q2-mCherry	(Romanauska and Köhler 2018)
pZW114	*p426GAL1-APQ12-yeGFP-8HIS*	This study
pZW110	*p426GAL1-APQ12*	This study
pAAK0010	*p415GAL1-APQ12-6HIS*	This study
pAAK0011	*p415GAL1-apq12-ah-6HIS*	This study
pZW78	*p426GAL1-BRL1*	This study
pAAK0014	*p425GAL1-brl1^{F391E}*	This study
pAAK0015	*p425GAL1-brl1^{L402E}*	This study
pJV034	*p426GAL1-brl1^{N353D}*	This study
pAAK0020	*p426GAL1-brl1^{F391P}*	This study
pJV035	*p426GAL1-brl1^{T355A}*	This study
pJV036	*p426GAL1-brl1^{P355G}*	This study
pAAK0021	*p426GAL1-brl1^{C343Y}*	This study
pAAK0027	*p426GAL1-brl1^{A360D}*	This study

pAAK0025	*p426GAL1-brl1^{Y347H}*	This study
pAAK0029	*p426GAL1-brl1^{W368Y}*	This study
pJV039	*p426GAL1-brl1$^{F391E\ P355G}$*	This study
pJV037	*p426GAL1-brl1$^{F391E\ N353D}$*	This study
pJV038	*p426GAL1-brl1$^{F391E\ T355A}$*	This study
pAAK0022	*p426GAL1-brl1$^{C343Y\ F391E}$*	This study
pAAK0018	*p426GAL1-brl1$^{C365S\ C371S}$*	This study
pAAK0028	*p426GAL1-brl1$^{A360D\ F391E}$*	This study
pAAK0026	*p426GAL1-brl1$^{Y347H\ F391E}$*	This study
pAAK0030	*p426GAL1-brl1$^{W368Y\ F391E}$*	This study
pAAK0019	*p426GAL1-brl1$^{F391E\ C365S\ C371S}$*	This study
pJV030	*P426GAL1-BRL1-yeGFP-8HIS*	This study
pAAK0016	*p426GAL1-brl1^{F391E}-yeGFP-8HIS*	This study
pJV046	*pRS315-brl1^{F391P}*	This study
pJV047	*pRS315-brl1^{C343Y}*	This study
pAAK0031	*pRS315-brl1$^{C365S\ C371S}$*	This study
pJV044	*pRS315-brl1^{Y347H}*	This study
pJV045	*pRS315-brl1^{A360D}*	This study
pJV043	*pRS315-brl1^{W368Y}*	This study
pJV040	*pRS315-brl1^{N353D}*	This study
pJV041	*pRS315-brl1^{T355A}*	This study
pJV042	*pRS315-brl1^{P356G}*	This study
pZW24	*pRS315-BRL1*	(Zhang, Neuner et al. 2018)
pKW1219	*pRS425-NLS-mRFP1*	K. Weis
pAAK0047	*p426GAL1-brr6L145E*	This study
pAAK0048	*p426GAL1-brr6F152E*	This study
pJV031	*p426GAL1-BRR6-yeGFP-8HIS*	This study
pAAK0071	*p426GAL1-brr6F152E-yeGFP-8HIS*	This study
pZW63	*pRS315-BRR6*	(Zhang, Neuner et al. 2018)
pAAK0053	*pRS315-brr6L145E*	This study
pAAK0054	*pRS315-brrF152E*	This study
pZW69	*p426GAL1-BRR6-10HIS*	(Zhang, Neuner et al. 2018)
pAAK0068	*p426GAL1-spBRR6-GFP-FLAG*	This study
pAAK0069	*pRS315-pADH1-spBRR6-FLAG*	This study
pAAK0051	*p426GAL1-BRR6$^{A^{\alpha H}}$-yeGFP-8HIS*	This study
pAAK0052	*p426GAL1-brr6$^{A^{\alpha H}}$-yeGFP-8HIS*	This study
pAAK0055	*pRS315-BRL1-BRR6*	This study
pAAK0056	*pRS316-BRL1-BRR6*	This study

6.1.7 *E. coli* strains

For all clonings, *E. coli* strain DH5α (supE44 ΔlacU169 (φ80lacZΔM15) hsdR17 recA1 gyrA96 thi-1 relA1) was used.

6.1.8 *S. cerevisiae* strains

Strain	Genotype	Source
ESM356-1	*MATa ura3-52 trp1Δ63 his3Δ200 leu2Δ1*	Schiebel Lab
YZW873	*MATa ura3-52 leu2Δ1 his3Δ200 trp1Δ63 apq12Δ::NatNT2*	This study
YZW952	*MATa ura3-52 leu2Δ1 his3Δ200 trp1Δ63 apq12-ah-NatNT2*	This study
YZW895	*MATa ura3-52 leu2Δ1 his3Δ200 trp1Δ63 NatNT2- pADH1-yeGFP-APQ12*	This study
AAK0032	*MATa ura3-52 leu2Δ1 his3Δ200 trp1Δ63 NatNT2- pADH1-yeGFP-apq12-ah*	This study
AAK0018	*MATa ura3-52 leu2Δ1 his3Δ200 trp1Δ63 APQ12-GFP$_{1-10}$-CaURA3MX*	This study
AAK0039	*MATa ura3-52 leu2Δ1 his3Δ200 trp1Δ63 NATMX-CDC42pr-yeGFP$_{1–10}$-APQ12*	This study
AAK0038	*MATa ura3-52 leu2Δ1 his3Δ200 trp1Δ63 apq12-ah-GFP$_{1-10}$-CaURA3MX*	This study
AAK0040	*MATa ura3-52 leu2Δ1 his3Δ200 trp1Δ63 NATMX-CDC42pr-yeGFP$_{1–10}$-apq12-ah*	This study
AAK0019	*MATa ura3-52 leu2Δ1 his3Δ200 trp1Δ63 MPS3-GFP$_{1-10}$-CaURA3MX*	This study
YZW902	*MATa ura3-52 leu2Δ1 his3Δ200 trp1Δ63 APQ12-HBH-HphMX4*	This study
AAK0020	*MATa ura3-52 leu2Δ1 his3Δ200 trp1Δ63 apq12-ah-HBH-HphMX4*	This study
YZW906	*MATa ura3-52 leu2Δ1 his3Δ200 trp1Δ63 TRP1-pGAL1-HBH-APQ12*	This study
AAK0021	*MATa ura3-52 leu2Δ1 his3Δ200 trp1Δ63 TRP1-pGAL1-HBH-apq12-ah*	This study
YZW967	*MATa ura3-52 leu2Δ1 his3Δ200 trp1Δ63 POM152-HBH-HphMX4*	This study
YZW945	*MATa ura3-52 leu2Δ1 his3Δ200 trp1Δ63 TRP1-pGAL1-HBH-POM152*	This study
YZW738	*MATa ura3-52 leu2Δ1 his3Δ200 trp1Δ63 NatNT2-pADH-GFP-BRL1*	(Zhang, Neuner et al. 2018)
YZW782	*MATa ura3-52 leu2Δ1 his3Δ200 trp1Δ63 NatNT2-pADH-GFP-BRR6 NUP85-tdTomato-KanMX6*	This study
YZW783	*MATa ura3-52 leu2Δ1 his3Δ200 trp1Δ63 NatNT2-pADH-GFP-BRL1 NUP85-tdTomato-KanMX4*	(Zhang, Neuner et al. 2018)
YZW931	*MATa ura3-52 leu2Δ1 his3Δ200 trp1Δ63 SEC63-GFP-HphNT1*	(Zhang, Neuner et al. 2018)
YZW932	*MATa ura3-52 leu2Δ1 his3Δ200 trp1Δ63 OLE1-GFP-hphNT1*	(Zhang, Neuner et al. 2018)
AAK0031	*MATa ura3-52 leu2Δ1 his3Δ200 trp1Δ63::YIPlac-dsRED-HDEL-NatMX RPL25-YeGFP-klTRP1*	This study
AAK0011	*GPY658 MATa ura3-52 leu2Δ1 his3Δ200 trp1Δ63 UBR1::pGAL1-HA-UBR1-HIS3MX6 NatNT2-pADH1-yeGFP-APQ12, NUP85-tdTomato-HphMX4*	This study
YJV068	*MATa ura3-52 leu2Δ1 his3Δ200 trp1Δ63 UBR1::pGAL1-HA-UBR1-HIS3MX6 NatNT2-pADH1-yeGFP-apq12-ah, NUP85-tdTomato-HphMX4*	This study
AAK0012	*GPY658 MATa ura3-52 leu2Δ1 his3Δ200 trp1Δ63 UBR1::pGAL1-HA-UBR1-HIS3MX6 KanMX6-pCUP1-Ubi-R-DHFR(ts)-Myc-BRR6 NatNT2-pADH1-yeGFP-APQ12, NUP85-tdTomato-HphMX4*	This study
YJV069	*MATa ura3-52 leu2Δ1 his3Δ200 trp1Δ63 UBR1::pGAL1-HA-UBR1-HIS3MX6 KanMX6-pCUP1-Ubi-R-DHFR(ts)-Myc-BRR6 NatNT2-pADH1-yeGFP-apq12-ah, NUP85-tdTomato-HphMX4*	This study
AAK0013	*GPY658 MATa ura3-52 leu2Δ1 his3Δ200 trp1Δ63 UBR1::pGAL1-HA-UBR1-His3MX6 KanMX6-pCUP1-Ubi-R-DHFR(ts)-Myc-BRL1 NatNT2-pADH1-yeGFP-APQ12, NUP85-tdTomato-HphMX4*	This study
YJV070	*MATa ura3-52 leu2Δ1 his3Δ200 trp1Δ63 UBR1::pGAL1-HA-UBR1-HIS3MX6 KanMX6-pCUP1-Ubi-R-DHFR(ts)-Myc-BRL1 NatNT2-pADH1-yeGFP-apq12-ah, NUP85-tdTomato-HphMX4*	This study
YZW929	*MATa ura3-52 leu2Δ1 his3Δ200 trp1Δ63 NUP85-tdTomatoKkanMX4*	This study
YJV014	*MATa ura3-52 leu2Δ1 his3Δ200 trp1Δ63 apq12Δ::NatNT2 leu2Δ1::pRS305H-BRR6-yeGFP his3Δ200::pRS303K-apq12-6HA*	This study
YJV015	*MATa ura3-52 leu2Δ1 his3Δ200 trp1Δ63 apq12Δ::NatNT2 leu2Δ1::pRS305H-BRR6-yeGFP his3Δ200::pRS303K-apq12-ah-6HA*	This study
YZW491	*MATa ura3-52 leu2Δ1 his3Δ200 trp1Δ63 BRL1-yeGFP-HphNT1*	This study

YJV073	*MATa ura3-52 leu2Δ1 his3Δ200 trp1Δ63 apq12-ah-6HA-KanMX4 BRL1-yeGFP-klTRP1*	This study
YJV058	*MATa ura3-52 leu2Δ1 his3Δ200 trp1Δ63 APQ12-6HA-KanMX4*	This study
YJV059	*MATa ura3-52 leu2Δ1 his3Δ200 trp1Δ63 apq12-ah-6HA-KanMX4*	This study
AAK0041	*MATa ura3-52 leu2Δ1 his3Δ200 trp1Δ63::YIPlac-GFP-HDEL-NatMX*	This study
YZW292	*MATa ura3-52 leu2Δ1 his3Δ200 trp1Δ63::YIPlac-dsRED-HDEL-NatMX*	This study
AAK0034	*MATa ura3-52 leu2Δ1 his3Δ200 trp1Δ63 brl1Δ::KanMX, pRS316-BRL1, pRS303N-brl1^{F391E}*	This study
AAK0035	*MATa ura3-52 leu2Δ1 his3Δ200 trp1Δ63 brl1Δ::KanMX, pRS316-BRL1, pRS303N-brl1^{L402E}*	This study
AAK0036	*MATa ura3-52 leu2Δ1 his3Δ200 trp1Δ63 brl1Δ::KanMX, pRS316-BRL1, pRS303N*	This study
AAK0037	*MATa ura3-52 leu2Δ1 his3Δ200 trp1Δ63 brl1Δ::KanMX, pRS316-BRL1, pRS315-BRL1*	This study
AK948	*MATa ura3-52 leu2Δ1 his3Δ200 trp1Δ63 NUP159- mCherry-KanMX6*	Schiebel lab
AAK0042	*MATa ura3-52 leu2Δ1 his3Δ200 trp1Δ63 NUP82- tdTomato-HpHMX6*	This study
AK725	*MATa ura3-52 leu2Δ1 his3Δ200 NUP133- mCherry-KanMX6*	Schiebel lab
YZW815	*MATa ura3-52 leu2Δ1 his3Δ200 trp1Δ63 NSP1- tdTomato-HphMX6*	This study
YJV075	*MATa ura3-52 leu2Δ1 his3Δ200 trp1Δ63 NUP42- tdTomato-HphMX6*	This study
AK723	*MATa ura3-52 leu2Δ1 his3Δ200 trp1Δ63 NUP84- mCherry-KanMX6*	Schiebel lab
YJV081	*MATa ura3-52 leu2Δ1 his3Δ200 trp1Δ63 NUP116-tdTomato-HphMX6*	This study
YJV076	*MATa ura3-52 leu2Δ1 his3Δ200 trp1Δ63 NUP82-tdTomato-HphMX6 NUP159-yeGFP-klTRP1*	This study
YJV077	*MATa ura3-52 leu2Δ1 his3Δ200 trp1Δ63 NUP159-yeGFP-klTRP1 NUP116-tdTomato-HphMX6*	This study
YZW332	*MATa ura3-52 leu2Δ1 his3Δ200 trp1Δ63 UBR1::pGAL1-HA-UBR1-His3MX6 leu2Δ1::pINT-CRE-EBD78-LEU2 NUP188-loxP-HA-mCherry-HphMX6-loxP-GFP*	(Zhang, Neuner et al. 2018)
YZW14	*MATa ura3-52 leu2Δ1 brr6-751*	Dr. I. Hagan
YZW13	*MATa ura3-52 leu2Δ1 brr6-19*	Dr. I. Hagan
YZW15	*MATa ura3-52 leu2Δ1 brr6-721*	Dr. I. Hagan
YZW16	*MATa ura3-52 leu2Δ1 brr6-732*	Dr. I. Hagan
YZW17	*MATa ura3-52 leu2Δ1 brr6-733*	Dr. I. Hagan
YZW19	*MATa ura3-52 leu2Δ1 brr6-69*	Dr. I. Hagan
YZW769	*MATa ura3-52 leu2Δ1 his3Δ200 trp1Δ63 Δnup116::HphNT1*	(Zhang, Neuner et al. 2018)
YZW05	*MATa ura3-52 leu2Δ1 brr6Δ::KanMX pRS316-BRR6*	Dr. I. Hagan
YZW079	*MATa ura3-52 leu2Δ1 his3Δ200 trp1Δ63 GLE1-tdTomato-HphMX6*	This study
YZW078	*MATa ura3-52 leu2Δ1 his3Δ200 trp1Δ63 GLE2-tdTomato-HphMX6*	This study
AAK0046	*MATa ura3-52 leu2Δ1 his3Δ200 trp1Δ63 POM152-tdTomato-HphMX6*	This study
AAK0047	*MATa ura3-52 leu2Δ1 his3Δ200 trp1Δ63 NUP170-yeGFP-klTRP1*	This study
AAK0048	*MATa ura3-52 leu2Δ1 his3Δ200 trp1Δ63 NUP60-yeGFP-klTRP1*	This study
AAK0050	*MATa ura3-52 leu2Δ1 his3Δ200 trp1Δ63 NUP84-yeGFP-klTRP1*	This study
AAK0052	*MATa ura3-52 leu2Δ1 his3Δ200 trp1Δ63 NUP82-yeGFP-klTRP1*	This study
AAK0078	*MATa ura3-52 leu2Δ1 his3Δ200 trp1Δ63 UBR1::pGAL1-HA-UBR1-His3MX6 leu2Δ1::pINT-CRE-EBD78-LEU2 NUP133-loxP-HA-mCherry-HphMX6-loxP-GFP*	This study
AAK0080	*MATa ura3-52 leu2Δ1 his3Δ200 trp1Δ63 UBR1::pGAL1-HA-UBR1-His3MX6 leu2Δ1::pINT-CRE-EBD78-LEU2 NUP82-loxP-HA-mCherry-HphMX6-loxP-GFP*	This study
AAK0079	*MATa ura3-52 leu2Δ1 his3Δ200 trp1Δ63 UBR1::pGAL1-HA-UBR1-His3MX6 leu2Δ1::pINT-CRE-EBD78-LEU2 POM152-loxP-HA-mCherry-HphMX6-loxP-GFP*	This study
AAK0084	*MATa ura3-52 leu2Δ1 his3Δ200 trp1Δ63 brl1Δ::KanMX brr6Δ::NatNT2 pRS316-BRR6-BRL1*	This study

AAK0081	*MATa ura3-52 leu2Δ1 his3Δ200 trp1Δ63 UBR1::pGAL1-HA-UBR1-His3MX6 leu2Δ1::pINT-CRE-EBD78-LEU2 NUP159-loxP-HA-mCherry-HphMX6-loxP-GFP*	This study
YZW129	*MATa ura3-52 leu2Δ1 his3Δ200 trp1Δ63 UBR1::pGAL1-HA-UBR1-His3MX6 SPC42-mCherry-NatNT2 KanMX6-pCup1-Ubi-R-DHFR(ts)-Myc-BRR6 klTRP1-pCUP1-Ubi-R-DHFR(ts)-Myc-BRL1 NUP188-GFP-HphNT1*	(Zhang, Neuner et al. 2018)
AK821	*MATa ura3-52 leu2Δ1 his3Δ200 trp1Δ63 NUP159-yeGFP-klTRP1*	Schiebel lab
AK819	*MATa ura3-52 leu2Δ1 his3Δ200 trp1Δ63 NDC1-yeGFP-klTRP1*	Schiebel lab
AK721	*MATa ura3-52 leu2Δ1 his3Δ200 trp1Δ63 POM34-yeGFP-klTRP1*	Schiebel lab
LD046	*MATa ura3-52 leu2Δ1 his3Δ200 trp1Δ63 NUP49-yeGFP-klTRP1*	Schiebel lab
AK949	*MATa ura3-52 leu2Δ1 his3Δ200 trp1Δ63 NUP2-mCherry-KanMX6*	Schiebel lab
AK820	*MATa ura3-52 leu2Δ1 his3Δ200 trp1Δ63NIC96-yeGFP-klTRP1*	Schiebel lab
AK969	*MATa ura3-52 leu2Δ1 his3Δ200 trp1Δ63 NUP120-yeGFP-klTRP1*	Schiebel lab
AK720	*MATa ura3-52 leu2Δ1 his3Δ200 trp1Δ63 NUP133-yeGFP-klTRP1*	Schiebel lab
YZW815	*MATa ura3-52 leu2Δ1 his3Δ200 trp1Δ63 UBR1::pGal1-HA-UBR1-His3MX6 NSP1-tdTomato-HphMX4*	Schiebel lab

6.2 Methods

6.2.1 Molecular Biology Methods

Polymerase chain reaction (PCR)

For amplification of DNA fragments for cloning, Q5 DNA polymerase was used. Reaction was set up as follows:

Components	Volume (µL)
Template	<1000 ng
100 µM Forward primer	0.25
100 µM Reverse primer	0.25
2 mM dNTP mix	5
5X Q5 reaction buffer	10
5X Q5 High GC enhancer	10
Q5 Polymerase	0.5
ddH_20	to 50

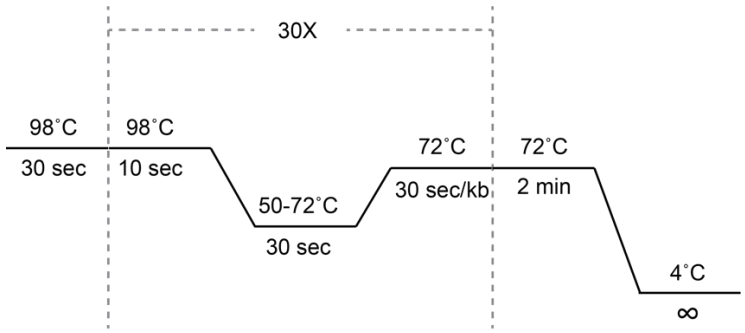

For amplification of gene tagging or deletion cassettes, HiFi DNA polymerase was used. The reaction and thermocycling conditions were set up as follows:

Components	Volume (μL)
Template	<1000 ng
100 μM Forward primer	0.25
100 μM Reverse primer	0.25
2 mM dNTP mix	5
10X HiFi buffer	5
50 mM MgCl2	2.5
5M Betaine	5
HiFi Polymerase	1
ddH_20	to 50

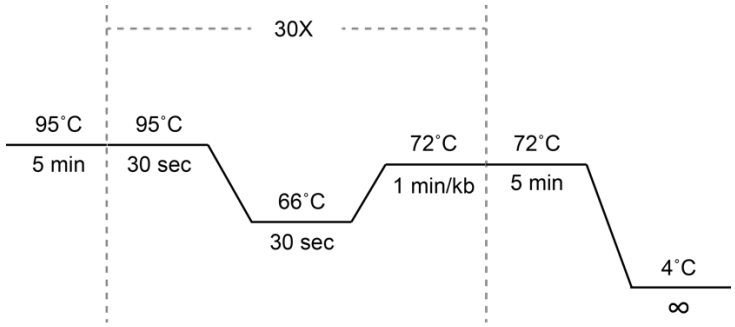

To confirm correct gene tagging or deletion, colony PCR was performed. Single yeast colonies were picked and resuspended in 50 μL of lysis buffer (see 6.1), and incubated at 37˚C for 1 h. 1 μL of the lysate was used as template for PCR. Reaction was set up as follows:

Components	Volume (μL)
Template	1
100 μM Forward primer	0.125
100 μM Reverse primer	0.125
2 mM dNTP mix	2.5
10X Taq Bujard buffer	2.5
Taq Polymerase	1
ddH_20	to 25

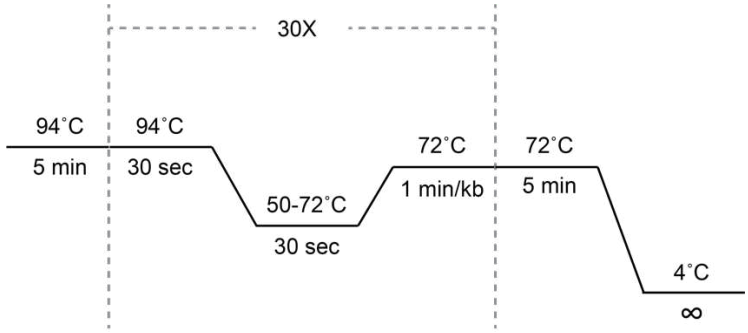

Restriction digestion

To digest plasmid DNA or PCR products, restriction endonucleases from NEB were used. Reaction conditions were optimized based on NEBcloner (https://nebcloner.neb.com/#!/redigest)

Agarose gel electrophoresis

To confirm the size of DNA fragments obtained by PCR or restriction digestion, samples mixed with 6X DNA loading dye were run on 1% agarose (Biozym) gel in 1X TAE buffer at 150 V. Staining of the gels was done in 1 ng/mL ethidium bromide bath for 20-30 min and visualized under a UV-trans-illuminator (BioRad).

Ligation

Ligation of PCR products and linearized plasmids was done using T4 DNA ligase (NEB), in 3:1 molar ratio, at room temperature for 15 min.

HiFi Assembly

Assembly of DNA fragments and linearized plasmids was done using the HiFi assembly master mix. Primers were designed by NEBuilder tool (https://nebuilder.neb.com/#!/). Plasmid and DNA fragments were combined in 1:3 molar ratio and incubated at 50˚C for 15-60 min.

6.2.2 Microbiological Methods

Culture and storage of *E. coli*

E. coli strains from stocks were streaked on LB plates with appropriate antibiotics followed by overnight incubation at 37˚C. Single colonies were then cultured at 37˚C in LB media with corresponding antibiotics. For long term storage of E. coli strains, liquid cultures were supplemented with 50% sterile glycerol and kept at -80˚C.

***E. coli* transformation**

For transformation of E. coli with plasmids and ligation products, DH5α chemically competent cells were used. 0.5 µL of plasmids or 5 µL of assembly products were added to 50 µL thawed competent cells and incubated on ice for 20 min followed by a heat-shock at 42˚C for 45 sec. Subsequently, the cells were chilled on ice for 2 minutes before adding 1 mL of LB/2X YT medium. The cells were then incubated at 37°C for 30 minutes with shaking. Afterward, they were centrifuged for 2 minutes at 3200 rpm and plated on LB plates containing the appropriate antibiotics and incubated at 37˚C overnight.

Plasmid isolation from *E. coli*

Cell pellets from 2 mL overnight cultures were alkaline lysed. Denatured proteins and chromosomal DNA were precipitated using a high concentration of potassium acetate. The resulting plasmid DNA was then precipitated by isopropanol followed by washing with 70% ethanol. The dried plasmid DNA was then rehydrated by adding 50 μL ddH_2O.

Culture and storage of yeast strains

Strains from the stocks were streaked out on appropriate selection plates and grown at 30˚C for 2 days. ts-mutants were incubated at 23˚C for 3-4 days. Plasmid containing strains were always grown on selective media/plates. Yeast strains were grown in YPD, SC, or SC-Raf medium. To induce the expression of proteins under the *GAL1* promoter, the SC-Raf media was supplemented with galactose added to a final concentration of 2%. For long-term storage, cells were resuspended in 15% sterile glycerol and kept at -80˚C.

Yeast competent cells and transformation

To make competent cells, 50 mL of media was inoculated with an overnight culture to an OD_{600} of 0.1 and grown at 30˚C with shaking until they reached an OD_{600} 0.6-1. The cells were then harvested at 3200 rpm, washed once with 25 mL ddH_20 and once with 12.5 mL LiSorb. LiSorb was completely removed before adding 300 μL of LiSorb and 50 μL of heat-denatured salmon-sperm DNA. Cells were resuspended thoroughly and aliquoted either for storage at -80˚C or immediate use. For transformation, 0.5-1 μL of plasmid DNA or 5-10 μL of PCR product was added to 50 μL of competent cells and incubated at room temperature (RT) for 15 min. Then, 300 μL of LiPEG was added and mixed by vortexing. After a 15 min incubation at RT, 30 μL of sterile DMSO was added to the cells followed by a 10 min heat-shock at 42˚C for 45 sec. The mixture was then spun down at 3200 rpm for 2 min and the supernatant was removed. For antibiotic selection, 600 of YPD medium was added to allow the cells to recover overnight, after which they were plated on appropriate plates. For auxotrophic selection, cell pellet was resuspended in 200 μL of PBS and plated on selection plates. Colonies appeared after 2-3 days after incubation at appropriate temperature. Single colonies were picked and purified further on selection plates before further analysis.

Spot assay

Yeast strains were grown overnight in appropriate media and temperature. 1 OD_{600} was collected by centrifugation at 3200 rpm for 2 min. Cells pellets were resuspended in 1 mL of sterile PBS and serially diluted 10, 100, 1000 and 10,000 times. 2-3 μL of the cell

suspensions were spotted on appropriate plates at incubated at desired temperatures for 2-4 days.

Analysis of heat-inducible degron strains

A heat inducible degron system (Sanchez-Diaz, Kanemaki et al. 2004) was used to deplete *BRL1* and *BRR6*. Both proteins were tagged with the degron at the N-terminus under the *CUP1* promoter. The *UBR1* gene was under the control of the *GAL1* promoter. The strains were initially cultured overnight at 23˚C in YP-Raf medium containing 0.1 mM $CuSO_4$. $CuSO_4$ was then washed out by replacing the medium with YP-Raf. To initiate depletion, the temperature was raised to 37˚C, and 2% galactose (final concentration) was added.

Recombination induced tag exchange (RITE)

The genes were tagged with the RITE cassette described in (Terweij, van Welsem et al. 2013). 1 µM estradiol was added to the culture to induce recombination. At the same time, expression from the *GAL1* promoter was induced by adding 2% galactose. Cells were incubated at 30°C with shaking and then imaged.

6.2.3 Biochemical Methods

Yeast total cell protein extraction

A TCA-based method was used to prepare a total protein lysate from yeast cells. 3 OD_{600} of cells were first collected, then resuspended in 1 mL of extraction buffer (1.5 mL of 1.85 M NaOH in 8.5 ml of ddH_2O) and incubated for 10 min on ice. 150 µL of 55% (w/v) TCA was then added, and the mixture was further incubated for another 10 minutes on ice. Precipitated proteins were collected by centrifugation at 14000 rpm for 15 minutes at 4°C. The supernatant was carefully removed, and the protein pellet was resuspended in 300 µL of HU buffer supplemented with 30 mM DTT, and heated at 65˚C for 10-15 min. Samples were centrifuged at 14000 rpm for 5-10 min before loading on the gel.

Sodium dodecyl sulfate-Polyacrylamide gel electrophoresis (SDS-PAGE)

Size separation of proteins was done by SDS-PAGE in Mini-PROTEAN II gel system (BioRad). 4-20% precast polyacrylamide gels (Mini-PROTEAN® TGX™ Precast Protein Gels, BioRad) were used. Samples were loaded along with prestained protein marker (ThermoFisher). Gels were run in SDS buffer at 30-40 mA/gel.

Western blot

PAGE separated proteins were transferred on to a PVDF membrane (Immobilon, Millipore) by a semi dry method, for 70 min at 110 mA per transfer. After transfer the

membrane was blocked in blocking buffer for 50-60 min at RT, and incubated overnight in primary antibody, diluted in blocking buffer, at 4˚C. Next, it was incubated in HRP-conjugated secondary antibody diluted in blocking buffer, for 1 h at RT. The membrane was washed 3 times, 5 min each with TBS-T before being imaged on the LAS-4000 camera system (FujiFilm) using freshly mixed ECL 1 and 2 solutions in 1:1 ratio.

Co-Immunoprecipitation

25 OD of cells were harvested and suspended in lysis buffer (20 mM Tris–Cl, pH 8.0, 150 mM NaCl, 5 mM MgCl2, and 10% glycerol) supplemented with 10 mM NaF, 60 mM β-glycerophosphate, 1 tablet per 50 ml of Roche protease inhibitor cocktail complete (EDTA free), and 1 mM PMSF. Lysis was performed using a FastPrep machine (MP Biomedicals) with the addition of glass beads (BioSpec Products). Subsequently, 0.5% Triton X-100 was introduced to the cell lysate and incubated on ice for 10 minutes. After centrifugation, the soluble proteins and cell debris were separated, followed by incubation with GFP-Trap agarose beads (Chromotek) for 2 hours at 4°C. The beads were washed thrice with lysis buffer containing 0.1% Triton X-100 and twice with wash buffer (20 mM Tris–Cl, pH 8.0, 150 mM NaCl, and 5 mM MgCl2). Elution of the bound proteins was performed using 50 µl of 2X laemmli buffer, followed by heating for 5 minutes at 95°C, and subsequently utilized for SDS-PAGE and western blotting.

Liposome preparation

All lipids were obtained from Avanti Polar lipids, except for Atto647 N, which was sourced from Atto-Tec. The lipid composition of the PM mix comprised: 34.8 mol% 1-palmitoyl-2-oleoyl-sn-glycero-3-phosphocholine (POPC), 15 mol% 1,2-dioleoyl-sn-glycero-3-phosphoserine (DOPS), 20 mol% 1-hexadecanoyl-2-octadecenoyl-sn-glycero-3-phospho-ethanolamine (POPE), 25 mol% cholesterol (from ovine wool), 5 mol% liver L-α-phosphatidylinositol (PI, from liver), and 0.2 mol% Atto647N-DPPE. The NE (nuclear envelope) lipid mix consisted of: 19.8 mol% POPC, 3 mol% DOPS, 42 mol% cholesterol, 7 mol% POPE, 23 mol% PI, 5 mol% PI(4,5)P2, and 0.2 mol% Atto647 (Zhendre, Grélard et al. 2011). SUVs (small uni-lamellar vesicles) were formed as previously described by dissolving the lipid mixtures in Octyl-β-D glucopyranoside (OG)-containing buffer, diluting OG below the critical micellar concentration, flow dialysis, and isolating SUVs using Nycodenz-gradient centrifugation (Weber, Zemelman et al. 1998). The concentrated liposomes were then extruded 23 times through a 100 nm filter and stored at 4°C.

For the preparation of GUVs (giant uni-lamellar vesicles), the PM (plasma membrane) mix was used. SUVs were employed to produce GUVs as previously described (Malsam, Parisotto et al. 2012), with the following modifications: (I) the GUVs underwent desalting twice using a PD10 column (GE Healthcare) instead of employing a Sephadex-G50 gel filtration column for the second desalting step. (II) Platinum-coated glass slides (GeSiM) were utilized instead of ITO-coated glass slides (GeSiM) (Meijer, Dörr et al. 2018).
The lipid concentration was determined by the fluorescence of Atto647 N with excitation at 647 nm and emission at 670 nm using a Fluoroskan Ascent FL plate reader (Thermo Scientific) in a 96-well plate (integration time: 1000 ms). The liposomes were disrupted by 0.5% Dodecyl-maltoside (DDM) to measure the recovery of total lipid, which was then compared to the lipid content after preparation.

Float-up assay

The interaction between AαH and AαH-ah peptides (PSL Peptide Specialty Laboratories GmbH, Heidelberg; amino acid sequence: KLLMNFITLVKRFL, KLDMNRNTLVKRNL) conjugated with Atto488 (prepared freshly in DMSO and diluted in fusion buffer: 25 mM HEPES pH 7.4, 135 mM KCl, 1 mM DTT) with SUVs was assessed using Nycodenz gradient centrifugation. A mixture containing 0.45 mM lipid and either 18 µM AαH or AαH-ah peptide, or 18 µM Atto488, in fusion buffer supplemented with 2.1% DMSO and 1 mM DTT was incubated for 30 minutes at room temperature, with 10% of the sample reserved as the reference input. The peptide-only sample served as the floatation control. Nycodenz (prepared in fusion buffer) was added to the sample to create a 40% Nycodenz layer at the bottom of the centrifugation tube. The sample was then overlaid with decreasing concentrations of Nycodenz (30%, 20%, 10%, and 0%) and centrifuged at 55,000 r.p.m. and 4°C for 2 hours and 30 minutes using an SW55 rotor (Beckman Coulter). The floated SUVs were located in the layer between 10% and 20% Nycodenz. The recovery of SUVs was determined by measuring the fluorescence of Atto647 N in the DDM lysed sample and comparing it to the input. The binding of the peptide or Atto488 was assessed by analyzing the fluorescence signal of Atto488 (excitation: 460 nm, emission: 538 nm, integration time: 1000 ms) in this layer and comparing it to the input probe. The binding of the peptide was adjusted based on the amount of the floated SUVs. To assess peptide interaction with GUVs, 3.3 µM GUVs were incubated with varying peptide concentrations ranging from a 1:1 to 10:1 ratio in fusion buffer at room temperature for 15 minutes. As a control to analyze changes in GUV morphology, 0.04%

DMSO was added to GUVs without peptide. The morphology of the GUVs was observed through the fluorescence of Atto647, while peptide interaction was monitored by the fluorescent signal of Atto488. Measurements were conducted in a chambered coverslip (Ibidi, catalogue no. 80826) using a DeltaVision microscope.

Microscale Thermophoresis (MST)

For determination of the KD values via MST, 2 µM Atto488 coupled to AαH and AαH-ah peptide, or Atto488 as a control, was incubated for 15 minutes at room temperature with increasing liposome concentrations in fusion buffer containing 0.01% Triton X-100. All samples were loaded into Premium capillaries, and thermophoresis was measured using a Monolith NT.115 (NanoTemper) instrument with an LED power of 40% (green filter) and an MST power of 17%. The MST data were evaluated using a single exponential function, considering the initial state calculated by linear regression. The data were normalized to the ratio of bound to unbound peptide, and the KD value was determined according to the Hill equation.

$$y = \frac{[c]^n}{[c]^n + K_D^n},$$

n = hill slope

Total lipids extraction

10 OD_{600} of cells were harvested and homogenized using a FastPrep machine (MP Biomedicals) in 155 mM ammonium bicarbonate buffer (pH 7.5). The homogenized cells underwent acidic Bligh & Dyer lipid extractions, with internal lipid standards added from a master mix containing various lipid species, including PC (phosphatidylcholine, Avanti Polar Lipids), PI (phosphatidylinositol), PE, PS, PG (phosphatidylethanolamine, phosphatidylserine, phosphatidylglycerol (Özbalci, Sachsenheimer et al. 2013)), DAG (diacylglycerol, Larodan), TAG (triacylglycerol, Avanti Polar Lipids), PA (phosphatidic acid, Avanti Polar Lipids), and t-Cer (t-ceramide, Avanti Polar Lipids). Lipids recovered in the organic extraction phase were evaporated using a gentle stream of nitrogen. Prior to measurements, lipid extracts were dissolved in 10 mM ammonium acetate in methanol and transferred to 96-well plates (Eppendorf twintec plate 96). Mass spectrometric measurements were performed in positive ion mode on an AB SCIEX QTRAP 6500+ mass spectrometer (Triversa Nanomate, Advion Biosciences), equipped with chip-based (HD-D ESI Chip, Advion Biosciences) nano-electrospray infusion and ionization (Özbalci, Sachsenheimer et al. 2013). The following precursor ion scanning (PREC) and neutral

loss scanning (NL) modes were used for the measurement of the various lipid classes: +Prec 184 (PC), +PREC282 (t-Cer), +NL141 (PE), +NL185 (PS), +NL277 (PI), + NL189 (PG), +NL115 (PA), +PREC 77 (ergosterol). Ergosterol was quantified following derivatization to ergosterol acetate in the presence of the internal standard (22E)-Stigmasta-5,7,22-trien-3-beta-ol (Aldrich). Data evaluation was performed using LipidView (ABSciex) and an in-house-developed software (ShinyLipids).

6.2.4 Microscopy Methods

Light microscopy

For live cell imaging, a DeltaVision RT system (Applied Precision, Olympus IX71 based) equipped with the Photometrics CoolSnap HQ camera (Roper Scientific) was used. Image acquisition was done using a 100x/1.4 NA UPlanSAPO objective (Olympus), a mercury arc light source and the softWoRx software (Applied Precision). Cells were always grown in SC media. Images were deconvoluted with the softWoRx software (Applied Precision) and processed with the ImageJ/Fiji software package (National Institutes of Health). For quantification purposes, all images were taken with the same exposure and illumination settings to allow direct comparison of the results. For time lapse experiments, cells were immobilized by coating glass bottom dishes (MatTek, P35G-1.5-14C) with a solution of 6% concanvalin A in PBS.

Electron microscopy (EM)

High-pressure frozen yeast samples were freeze-substituted, sectioned, and labeled for electron microscopy as described below: Cells were collected onto a 0.45 µm polycarbonate filter (Millipore) using vacuum filtration and then high-pressure frozen with an HPM010 (Abra-Fluid, Switzerland) freezing machine. Cells were freeze-substituted using the EM-AFS2 device (Leica Microsystems, Vienna, Austria) in a freeze substitution solution consisting of 0.1% glutaraldehyde, 0.2% uranyl acetate, and 1% water dissolved in anhydrous acetone, and then stepwise infiltrated with Lowicryl HM20 resin (Polysciences, Inc., Warrington, PA), beginning at a low temperature of -90°C. For polymerization, the samples were exposed to UV light for 48 hours at -45°C and gradually warmed up to 20°C. Lowicryl resin blocks containing embedded yeast cells were serially sectioned using a Reichert Ultracut S Microtome (Leica Instruments, Vienna, Austria) to a thickness of 70 - 80 nm. Post-staining with 3% uranyl acetate dissolved in water and lead citrate was performed. Sections were imaged using a Jeol JE-1400 (Jeol Ltd., Tokyo,

Japan) operating at 80 kV equipped with a 4k x 4k digital camera (F416, TVIPS, Gauting, Germany). Micrographs were adjusted for brightness and contrast using ImageJ/Fiji.

Immuno-electron microscopy

For immunolabeling sections of yeast cells, anti-GFP, anti-Nsp1 and anti-MAB414 antibodies were used. Samples were prepared in the same way, with the exception that glutaraldehyde was omitted from the freeze substitution solution. Sections on slot grids were treated with blocking buffer (1.5% BSA, 0.1% fish skin gelatin in PBS), then incubated with the primary antibody, rinsed in PBS, followed either by treatment with protein A-gold conjugates (15 nm, Utrecht University, Utrecht, The Netherlands) for anti-GFP, or incubated with a linker antibody, rabbit anti-mouse (for anti-Nsp1, mouse), and subsequently treated with protein A-gold conjugates (15 nm, Utrecht University, Utrecht, The Netherlands). Post-staining was performed as usual with 3% uranyl acetate and lead citrate.

7. Publications

Wanlu Zhang*, **Azqa Khan***, Jlenia Vitale, Annett Neuner, Kerstin Rink, Christian Lüchtenborg, Britta Burger, Thomas H. Söllner and Elmar Schiebel; A short perinuclear amphipathic α-helix in Apq12 promotes nuclear pore complex biogenesis. Open Biol. 24 November 2021 (11):210250210250.

DOI: https://doi.org/10.1098/rsob.210250

Jlenia Vitale*, **Azqa Khan***, Annett Neuner and Elmar Schiebel; A perinuclear α-helix with amphipathic features in Brl1 promotes NPC assembly. *Mol Biol Cell* (33), 14 April 2022.

DOI: https://doi.org/10.1091/mbc.E21-12-0616

***** Joint first authors

8. Bibliography

Adams, I. R. and J. V. Kilmartin (1999). "Localization of core spindle pole body (SPB) components during SPB duplication in Saccharomyces cerevisiae." J Cell Biol **145**(4): 809-823.

Afzelius, B. A. (1955). "The ultrastructure of the nuclear membrane of the sea urchin oocyte as studied with the electron microscope." Experimental Cell Research **8**(1): 147-158.

Akhtar, A. and S. M. Gasser (2007). "The nuclear envelope and transcriptional control." Nat Rev Genet **8**(7): 507-517.

Allegretti, M., C. E. Zimmerli, V. Rantos, F. Wilfling, P. Ronchi, H. K. H. Fung, C. W. Lee, W. Hagen, B. Turonova, K. Karius, M. Bormel, X. J. Zhang, C. W. Muller, Y. Schwab, J. Mahamid, B. Pfander, J. Kosinski and M. Beck (2020). "In-cell architecture of the nuclear pore and snapshots of its turnover." Nature **586**(7831): 796-+.

Anderson, D. J. and M. W. Hetzer (2007). "Nuclear envelope formation by chromatin-mediated reorganization of the endoplasmic reticulum." Nat Cell Biol **9**(10): 1160-1166.

Antonin, W., J. Ellenberg and E. Dultz (2008). "Nuclear pore complex assembly through the cell cycle: regulation and membrane organization." FEBS letters **582**(14): 2004-2016.

Antonny, B., S. Vanni, H. Shindou and T. Ferreira (2015). "From zero to six double bonds: phospholipid unsaturation and organelle function." Trends in Cell Biology **25**(7): 427-436.

Baker, K. E., J. Coller and R. Parker (2004). "The yeast Apq12 protein affects nucleocytoplasmic mRNA transport." Rna **10**(9): 1352-1358.

Borah, S., D. J. Thaller, Z. Hakhverdyan, E. C. Rodriguez, A. W. Isenhour, M. P. Rout, M. C. King and C. P. Lusk (2021). "Heh2/Man1 may be an evolutionarily conserved sensor of NPC assembly state." Mol Biol Cell **32**(15): 1359-1373.

Brohawn, S. G., N. C. Leksa, E. D. Spear, K. R. Rajashankar and T. U. Schwartz (2008). "Structural evidence for common ancestry of the nuclear pore complex and vesicle coats." Science **322**(5906): 1369-1373.

Bullitt, E., M. P. Rout, J. V. Kilmartin and C. W. Akey (1997). "The yeast spindle pole body is assembled around a central crystal of Spc42p." Cell **89**(7): 1077-1086.

Byers, B. and L. Goetsch (1975). "Behavior of spindles and spindle plaques in the cell cycle and conjugation of Saccharomyces cerevisiae." Journal of Bacteriology **124**(1): 511-523.

Callan, H. G., J. T. Randall and S. G. Tomlin (1949). "An Electron Microscope Study of the Nuclear Membrane." Nature **163**(4138): 280-280.

Casey, A. K., S. Chen, P. Novick, S. Ferro-Novick and S. R. Wente (2015). "Nuclear pore complex integrity requires Lnp1, a regulator of cortical endoplasmic reticulum." Molecular Biology of the Cell **26**(15): 2833-2844.

Chook, Y. M. and G. Blobel (1999). "Structure of the nuclear transport complex karyopherin-β2–Ran˙GppNHp." Nature **399**(6733): 230-237.

Dawson, T. R., M. D. Lazarus, M. W. Hetzer and S. R. Wente (2009). "ER membrane–bending proteins are necessary for de novo nuclear pore formation." Journal of Cell Biology **184**(5): 659-675.

DeGrasse, J. A., K. N. DuBois, D. Devos, T. N. Siegel, A. Sali, M. C. Field, M. P. Rout and B. T. Chait (2009). "Evidence for a shared nuclear pore complex architecture that is conserved from the last common eukaryotic ancestor." Mol Cell Proteomics **8**(9): 2119-2130.

Devos, D., S. Dokudovskaya, F. Alber, R. Williams, B. T. Chait, A. Sali and M. P. Rout (2004). "Components of Coated Vesicles and Nuclear Pore Complexes Share a Common Molecular Architecture." PLOS Biology **2**(12): e380.

Doucet, C. M., J. A. Talamas and M. W. Hetzer (2010). "Cell Cycle-Dependent Differences in Nuclear Pore Complex Assembly in Metazoa." Cell **141**(6): 1030-1041.
Drin, G. and B. Antonny (2010). "Amphipathic helices and membrane curvature." FEBS Letters **584**(9): 1840-1847.
Drin, G., J.-F. Casella, R. Gautier, T. Boehmer, T. U. Schwartz and B. Antonny (2007). "A general amphipathic α-helical motif for sensing membrane curvature." Nature Structural & Molecular Biology **14**(2): 138-146.
Dultz, E. and J. Ellenberg (2010). "Live imaging of single nuclear pores reveals unique assembly kinetics and mechanism in interphase." J Cell Biol **191**(1): 15-22.
Dultz, E., E. Zanin, C. Wurzenberger, M. Braun, G. Rabut, L. Sironi and J. Ellenberg (2008). "Systematic kinetic analysis of mitotic dis-and reassembly of the nuclear pore in living cells." The Journal of cell biology **180**(5): 857-865.
Eisenhardt, N., J. Redolfi and W. Antonin (2014). "Interaction of Nup53 with Ndc1 and Nup155 is required for nuclear pore complex assembly." Journal of cell science **127**(4): 908-921.
Elliott, S., M. Knop, G. Schlenstedt and E. Schiebel (1999). "Spc29p is a component of the Spc110p subcomplex and is essential for spindle pole body duplication." Proceedings of the National Academy of Sciences **96**(11): 6205-6210.
Farge, E. and P. F. Devaux (1992). "Shape changes of giant liposomes induced by an asymmetric transmembrane distribution of phospholipids." Biophysical journal **61**(2): 347-357.
Farge, E., D. M. Ojcius, A. Subtil and A. Dautry-Varsat (1999). "Enhancement of endocytosis due to aminophospholipid transport across the plasma membrane of living cells." American Journal of Physiology-Cell Physiology **276**(3): C725-C733.
Farsad, K. and P. D. Camilli (2003). "Mechanisms of membrane deformation." Current Opinion in Cell Biology **15**(4): 372-381.
Franke, W. W., U. Scheer, G. Krohne and E. D. Jarasch (1981). "The nuclear envelope and the architecture of the nuclear periphery." Journal of Cell Biology **91**(3): 39s-50s.
Franz, C., R. Walczak, S. Yavuz, R. Santarella, M. Gentzel, P. Askjaer, V. Galy, M. Hetzer, I. W. Mattaj and W. Antonin (2007). "MEL-28/ELYS is required for the recruitment of nucleoporins to chromatin and postmitotic nuclear pore complex assembly." EMBO reports **8**(2): 165-172.
Frey, S. and D. Görlich (2007). "A saturated FG-repeat hydrogel can reproduce the permeability properties of nuclear pore complexes." Cell **130**(3): 512-523.
Frey, S. and D. Görlich (2009). "FG/FxFG as well as GLFG repeats form a selective permeability barrier with self-healing properties." The EMBO Journal **28**(17): 2554-2567.
Funakoshi, T., M. Clever, A. Watanabe and N. Imamoto (2011). "Localization of Pom121 to the inner nuclear membrane is required for an early step of interphase nuclear pore complex assembly." Molecular Biology of the Cell **22**(7): 1058-1069.
Gall , J. G. (1967). "OCTAGONAL NUCLEAR PORES." Journal of Cell Biology **32**(2): 391-399.
Gallop, J. L., C. C. Jao, H. M. Kent, P. J. G. Butler, P. R. Evans, R. Langen and H. T. McMahon (2006). "Mechanism of endophilin N-BAR domain-mediated membrane curvature." The EMBO Journal **25**(12): 2898-2910.
Galy, V., P. Askjaer, C. Franz, C. López-Iglesias and I. W. Mattaj (2006). "MEL-28, a novel nuclear-envelope and kinetochore protein essential for zygotic nuclear-envelope assembly in C. elegans." Current Biology **16**(17): 1748-1756.
Gardner, J. M., E. O'Toole and S. L. Jaspersen (2021). "A mutation in budding yeast BRR6 affecting nuclear envelope insertion of the spindle pole body." MicroPubl Biol **2021**.

Gautier, R., D. Douguet, B. Antonny and G. Drin (2008). "HELIQUEST: a web server to screen sequences with specific α-helical properties." Bioinformatics **24**(18): 2101-2102.
Gerace, L. and B. Burke (1988). "Functional organization of the nuclear envelope." Annu Rev Cell Biol **4**: 335-374.
Görlich, D. and U. Kutay (1999). "Transport Between the Cell Nucleus and the Cytoplasm." Annual Review of Cell and Developmental Biology **15**(Volume 15, 1999): 607-660.
Görlich, D., S. Prehn, R. A. Laskey and E. Hartmann (1994). "Isolation of a protein that is essential for the first step of nuclear protein import." Cell **79**(5): 767-778.
Gruneberg, U., K. Campbell, C. Simpson, J. Grindlay and E. Schiebel (2000). "Nud1p links astral microtubule organization and the control of exit from mitosis." The EMBO journal **19**(23): 6475-6488.
Güttinger, S., E. Laurell and U. Kutay (2009). "Orchestrating nuclear envelope disassembly and reassembly during mitosis." Nature Reviews Molecular Cell Biology **10**(3): 178-191.
Hawryluk-Gara, L. A., E. K. Shibuya and R. W. Wozniak (2005). "Vertebrate Nup53 interacts with the nuclear lamina and is required for the assembly of a Nup93-containing complex." Molecular biology of the cell **16**(5): 2382-2394.
Hodge, C. A., V. Choudhary, M. J. Wolyniak, J. J. Scarcelli, R. Schneiter and C. N. Cole (2010). "Integral membrane proteins Brr6 and Apq12 link assembly of the nuclear pore complex to lipid homeostasis in the endoplasmic reticulum." Journal of cell science **123**(1): 141-151.
Hurt, E. and M. Beck (2015). "Towards understanding nuclear pore complex architecture and dynamics in the age of integrative structural analysis." Curr Opin Cell Biol **34**: 31-38.
Jang, J.-H., C. S. Lee, D. Hwang and S. H. Ryu (2012). "Understanding of the roles of phospholipase D and phosphatidic acid through their binding partners." Progress in Lipid Research **51**(2): 71-81.
Janke, C., M. M. Magiera, N. Rathfelder, C. Taxis, S. Reber, H. Maekawa, A. Moreno-Borchart, G. Doenges, E. Schwob, E. Schiebel and M. Knop (2004). "A versatile toolbox for PCR-based tagging of yeast genes: new fluorescent proteins, more markers and promoter substitution cassettes." Yeast **21**(11): 947-962.
Jaspersen, S. L. and S. Ghosh (2012). "Nuclear envelope insertion of spindle pole bodies and nuclear pore complexes." Nucleus **3**(3): 226-236.
Jaspersen, S. L. and M. Winey (2004). "THE BUDDING YEAST SPINDLE POLE BODY: Structure, Duplication, and Function." Annual Review of Cell and Developmental Biology **20**(1): 1-28.
Jaspersen, S. L. and M. Winey (2004). "The budding yeast spindle pole body: structure, duplication, and function." Annu Rev Cell Dev Biol **20**: 1-28.
Joseph, J. and M. Dasso (2008). "The nucleoporin Nup358 associates with and regulates interphase microtubules." FEBS Lett **582**(2): 190-196.
Jumper, J., R. Evans, A. Pritzel, T. Green, M. Figurnov, O. Ronneberger, K. Tunyasuvunakool, R. Bates, A. Žídek, A. Potapenko, A. Bridgland, C. Meyer, S. A. A. Kohl, A. J. Ballard, A. Cowie, B. Romera-Paredes, S. Nikolov, R. Jain, J. Adler, T. Back, S. Petersen, D. Reiman, E. Clancy, M. Zielinski, M. Steinegger, M. Pacholska, T. Berghammer, S. Bodenstein, D. Silver, O. Vinyals, A. W. Senior, K. Kavukcuoglu, P. Kohli and D. Hassabis (2021). "Highly accurate protein structure prediction with AlphaFold." Nature **596**(7873): 583-589.
Kaláb, P., P. Solc and J. Motlík (2011). "The role of RanGTP gradient in vertebrate oocyte maturation." Results Probl Cell Differ **53**: 235-267.
Kalderon, D., W. D. Richardson, A. F. Markham and A. E. Smith (1984). "Sequence requirements for nuclear location of simian virus 40 large-T antigen." Nature **311**(5981): 33-38.

Kitamata, M., T. Inaba and S. Suetsugu (2020). "The roles of the diversity of amphipathic lipids in shaping membranes by membrane-shaping proteins." Biochemical Society Transactions **48**(3): 837-851.
Knop, M., G. Pereira, S. Geissler, K. Grein and E. Schiebel (1997). "The spindle pole body component Spc97p interacts with the γ-tubulin of Saccharomyces cerevisiae and functions in microtubule organization and spindle pole body duplication." The EMBO journal **16**(7): 1550-1564.
Knop, M. and E. Schiebel (1997). "Spc98p and Spc97p of the yeast γ-tubulin complex mediate binding to the spindle pole body via their interaction with Spc110p." The EMBO journal **16**(23): 6985-6995.
Kralt, A., M. Wojtynek, J. S. Fischer, A. Agote-Aran, R. Mancini, E. Dultz, E. Noor, F. Uliana, M. Tatarek-Nossol, W. Antonin, E. Onischenko, O. Medalia and K. Weis (2022). "An amphipathic helix in Brl1 is required for nuclear pore complex biogenesis in S. cerevisiae." eLife **11**: e78385.
Kusumaatmaja, H., A. I. May, M. Feeney, J. F. McKenna, N. Mizushima, L. Frigerio and R. L. Knorr (2021). "Wetting of phase-separated droplets on plant vacuole membranes leads to a competition between tonoplast budding and nanotube formation." Proceedings of the National Academy of Sciences **118**(36): e2024109118.
Larochelle, M., D. Bergeron, B. Arcand and F. Bachand (2019). "Proximity-dependent biotinylation mediated by TurboID to identify protein–protein interaction networks in yeast." Journal of Cell Science **132**(11).
Lau, C. K., T. H. Giddings and M. Winey (2004). "A Novel Allele of Saccharomyces cerevisiae NDC1 Reveals a Potential Role for the Spindle Pole Body Component Ndc1p in Nuclear Pore Assembly." Eukaryotic Cell **3**(2): 447-458.
Lone, M. A., A. E. Atkinson, C. A. Hodge, S. Cottier, F. Martínez-Montañés, S. Maithel, L. Mène-Saffrané, C. N. Cole and R. Schneiter (2015). "Yeast Integral Membrane Proteins Apq12, Brl1, and Brr6 Form a Complex Important for Regulation of Membrane Homeostasis and Nuclear Pore Complex Biogenesis." Eukaryot Cell **14**(12): 1217-1227.
Makio, T., L. H. Stanton, C.-C. Lin, D. S. Goldfarb, K. Weis and R. W. Wozniak (2009). "The nucleoporins Nup170p and Nup157p are essential for nuclear pore complex assembly." Journal of Cell Biology **185**(3): 459-473.
Malsam, J., D. Parisotto, T. A. Bharat, A. Scheutzow, J. M. Krause, J. A. Briggs and T. H. Söllner (2012). "Complexin arrests a pool of docked vesicles for fast Ca2+-dependent release." The EMBO journal **31**(15): 3270-3281.
Masuda, M., S. Takeda, M. Sone, T. Ohki, H. Mori, Y. Kamioka and N. Mochizuki (2006). "Endophilin BAR domain drives membrane curvature by two newly identified structure-based mechanisms." Embo j **25**(12): 2889-2897.
Matthews, H. K., C. Bertoli and R. A. M. de Bruin (2022). "Cell cycle control in cancer." Nature Reviews Molecular Cell Biology **23**(1): 74-88.
McKeon, F. D., M. W. Kirschner and D. Caput (1986). "Homologies in both primary and secondary structure between nuclear envelope and intermediate filament proteins." Nature **319**(6053): 463-468.
Meijer, M., B. Dörr, H. C. Lammertse, C. Blithikioti, J. R. van Weering, R. F. Toonen, T. H. Söllner and M. Verhage (2018). "Tyrosine phosphorylation of Munc18-1 inhibits synaptic transmission by preventing SNARE assembly." The EMBO journal **37**(2): 300-320.
Mészáros, N., J. Cibulka, M. J. Mendiburo, A. Romanauska, M. Schneider and A. Köhler (2015). "Nuclear pore basket proteins are tethered to the nuclear envelope and can regulate membrane curvature." Developmental cell **33**(3): 285-298.

Milles, S. and E. A. Lemke (2011). "Single molecule study of the intrinsically disordered FG-repeat nucleoporin 153." Biophys J **101**(7): 1710-1719.
Moens, P. B. and E. Rapport (1971). "Spindles, spindle plaques, and meiosis in the yeast Saccharomyces cerevisiae (Hansen)." J Cell Biol **50**(2): 344-361.
Moore, M. S. and G. Blobel (1993). "The GTP-binding protein Ran/TC4 is required for protein import into the nucleus." Nature **365**(6447): 661-663.
Muller, E. G., B. E. Snydsman, I. Novik, D. W. Hailey, D. R. Gestaut, C. A. Niemann, E. T. O'Toole, T. H. Giddings Jr, B. A. Sundin and T. N. Davis (2005). "The organization of the core proteins of the yeast spindle pole body." Molecular Biology of the Cell **16**(7): 3341-3352.
Murphy, R., J. L. Watkins and S. R. Wente (1996). "GLE2, a Saccharomyces cerevisiae homologue of the Schizosaccharomyces pombe export factor RAE1, is required for nuclear pore complex structure and function." Molecular Biology of the Cell **7**(12): 1921-1937.
Murray, A. W. (2004). "Recycling the Cell Cycle: Cyclins Revisited." Cell **116**(2): 221-234.
Nakano, H., T. Funasaka, C. Hashizume and R. W. Wong (2010). "Nucleoporin translocated promoter region (Tpr) associates with dynein complex, preventing chromosome lagging formation during mitosis." J Biol Chem **285**(14): 10841-10849.
Nurse, P. (2000). "A Long Twentieth Century of the Cell Cycle and Beyond." Cell **100**(1): 71-78.
O'Toole, E. T., M. Winey and J. R. McIntosh (1999). "High-Voltage Electron Tomography of Spindle Pole Bodies and Early Mitotic Spindles in the Yeast Saccharomyces cerevisiae." Molecular Biology of the Cell **10**(6): 2017-2031.
Oertle, T., M. Klinger, C. A. O. Stuermer and M. E. Schwab (2003). "A reticular rhapsody: phylogenic evolution and nomenclature of the RTN/Nogo gene family1." The FASEB Journal **17**(10): 1238-1247.
Onischenko, E., E. Noor, J. S. Fischer, L. Gillet, M. Wojtynek, P. Vallotton and K. Weis (2020). "Maturation Kinetics of a Multiprotein Complex Revealed by Metabolic Labeling." Cell **183**(7): 1785-1800.e1726.
Onischenko, E., L. H. Stanton, A. S. Madrid, T. Kieselbach and K. Weis (2009). "Role of the Ndc1 interaction network in yeast nuclear pore complex assembly and maintenance." Journal of Cell Biology **185**(3): 475-491.
Onischenko, E., J. H. Tang, K. R. Andersen, K. E. Knockenhauer, P. Vallotton, C. P. Derrer, A. Kralt, C. F. Mugler, L. Y. Chan and T. U. Schwartz (2017). "Natively unfolded FG repeats stabilize the structure of the nuclear pore complex." Cell **171**(4): 904-917. e919.
Otsuka, S., K. H. Bui, M. Schorb, M. J. Hossain, A. Z. Politi, B. Koch, M. Eltsov, M. Beck and J. Ellenberg (2016). "Nuclear pore assembly proceeds by an inside-out extrusion of the nuclear envelope." eLife **5**: e19071.
Otsuka, S., A. M. Steyer, M. Schorb, J.-K. Hériché, M. J. Hossain, S. Sethi, M. Kueblbeck, Y. Schwab, M. Beck and J. Ellenberg (2018). "Postmitotic nuclear pore assembly proceeds by radial dilation of small membrane openings." Nature Structural & Molecular Biology **25**(1): 21-28.
Otsuka, S., J. O. B. Tempkin, W. Zhang, A. Z. Politi, A. Rybina, M. J. Hossain, M. Kueblbeck, A. Callegari, B. Koch, N. R. Morero, A. Sali and J. Ellenberg (2023). "A quantitative map of nuclear pore assembly reveals two distinct mechanisms." Nature **613**(7944): 575-581.
Özbalci, C., T. Sachsenheimer and B. Brügger (2013). Quantitative Analysis of Cellular Lipids by Nano-Electrospray Ionization Mass Spectrometry. Membrane Biogenesis: Methods and Protocols. D. Rapaport and J. M. Herrmann. Totowa, NJ, Humana Press**:** 3-20.
Paine, P. L., L. C. Moore and S. B. Horowitz (1975). "Nuclear envelope permeability." Nature **254**(5496): 109-114.

Pajtinka, P. and R. Vácha (2024). "Amphipathic Helices Can Sense Both Positive and Negative Curvatures of Lipid Membranes." J Phys Chem Lett **15**(1): 175-179.
Pawar, S. and U. Kutay (2021). "The Diverse Cellular Functions of Inner Nuclear Membrane Proteins." Cold Spring Harb Perspect Biol **13**(9).
Raices, M. and M. A. D'Angelo (2022). "Structure, Maintenance, and Regulation of Nuclear Pore Complexes: The Gatekeepers of the Eukaryotic Genome." Cold Spring Harbor Perspectives in Biology **14**(3).
Rasala, B. A., A. V. Orjalo, Z. Shen, S. Briggs and D. J. Forbes (2006). "ELYS is a dual nucleoporin/kinetochore protein required for nuclear pore assembly and proper cell division." Proceedings of the National Academy of Sciences **103**(47): 17801-17806.
Robinow, C. F. and J. Marak (1966). "A fiber apparatus in the nucleus of the yeast cell." J Cell Biol **29**(1): 129-151.
Romanauska, A. and A. Köhler (2018). "The inner nuclear membrane is a metabolically active territory that generates nuclear lipid droplets." Cell **174**(3): 700-715. e718.
Rothballer, A. and U. Kutay (2013). "Poring over pores: nuclear pore complex insertion into the nuclear envelope." Trends in biochemical sciences **38**(6): 292-301.
Saitoh, Y.-h., K. Ogawa and T. Nishimoto (2005). "Brl1p – A Novel Nuclear Envelope Protein Required for Nuclear Transport." Traffic **6**(6): 502-517.
Sanchez-Diaz, A., M. Kanemaki, V. Marchesi and K. Labib (2004). "Rapid Depletion of Budding Yeast Proteins by Fusion to a Heat-Inducible Degron." Science's STKE **2004**(223): pl8-pl8.
Scarcelli, J. J., C. A. Hodge and C. N. Cole (2007). "The yeast integral membrane protein Apq12 potentially links membrane dynamics to assembly of nuclear pore complexes." J Cell Biol **178**(5): 799-812.
Schaerer, F., G. Morgan, M. Winey and P. Philippsen (2001). "Cnm67p is a spacer protein of the Saccharomyces cerevisiae spindle pole body outer plaque." Molecular biology of the cell **12**(8): 2519-2533.
Schwartz, T. U. (2016). "The Structure Inventory of the Nuclear Pore Complex." J Mol Biol **428**(10 Pt A): 1986-2000.
Sheetz, M. P., R. G. Painter and S. J. Singer (1976). "Biological membranes as bilayer couples. III. Compensatory shape changes induced in membranes." Journal of Cell Biology **70**(1): 193-203.
Sheetz, M. P. and S. J. Singer (1974). "Biological Membranes as Bilayer Couples. A Molecular Mechanism of Drug-Erythrocyte Interactions." Proceedings of the National Academy of Sciences **71**(11): 4457-4461.
Shen, H., M. Pirruccello and P. De Camilli (2012). "SnapShot: Membrane Curvature Sensors and Generators." Cell **150**(6): 1300-1300.e1302.
Shulga, N. and D. S. Goldfarb (2003). "Binding dynamics of structural nucleoporins govern nuclear pore complex permeability and may mediate channel gating." Molecular and cellular biology **23**(2): 534-542.
Smoyer, C. J., S. S. Katta, J. M. Gardner, L. Stoltz, S. McCroskey, W. D. Bradford, M. McClain, S. E. Smith, B. D. Slaughter and J. R. Unruh (2016). "Analysis of membrane proteins localizing to the inner nuclear envelope in living cells." Journal of Cell Biology **215**(4): 575-590.
Solovei, I., A. S. Wang, K. Thanisch, C. S. Schmidt, S. Krebs, M. Zwerger, T. V. Cohen, D. Devys, R. Foisner, L. Peichl, H. Herrmann, H. Blum, D. Engelkamp, C. L. Stewart, H. Leonhardt and B. Joffe (2013). "LBR and lamin A/C sequentially tether peripheral heterochromatin and inversely regulate differentiation." Cell **152**(3): 584-598.

Stankunas, E. and A. Köhler (2023). "The interplay of nuclear pores and lipids." Current Opinion in Cell Biology **85**: 102251.
Stewart, M. (2007). "Molecular mechanism of the nuclear protein import cycle." Nature Reviews Molecular Cell Biology **8**(3): 195-208.
Stewart, M. (2007). "Ratcheting mRNA out of the nucleus." Mol Cell **25**(3): 327-330.
Strambio-De-Castillia, C., M. Niepel and M. P. Rout (2010). "The nuclear pore complex: bridging nuclear transport and gene regulation." Nature Reviews Molecular Cell Biology **11**(7): 490-501.
Subtil, A., I. Gaidarov, K. Kobylarz, M. A. Lampson, J. H. Keen and T. E. McGraw (1999). "Acute cholesterol depletion inhibits clathrin-coated pit budding." Proceedings of the National Academy of Sciences **96**(12): 6775-6780.
Sundberg, H. A. and T. N. Davis (1997). "A mutational analysis identifies three functional regions of the spindle pole component Spc110p in Saccharomyces cerevisiae." Molecular biology of the cell **8**(12): 2575-2590.
Talamas, J. A. and M. W. Hetzer (2011). "POM121 and Sun1 play a role in early steps of interphase NPC assembly." Journal of Cell Biology **194**(1): 27-37.
Tamm, T., A. Grallert, E. P. S. Grossman, I. Alvarez-Tabares, F. E. Stevens and I. M. Hagan (2011). "Brr6 drives the Schizosaccharomyces pombe spindle pole body nuclear envelope insertion/extrusion cycle." Journal of Cell Biology **195**(3): 467-484.
Tanguy, E., N. Kassas and N. Vitale (2018). "Protein¯Phospholipid Interaction Motifs: A Focus on Phosphatidic Acid." Biomolecules **8**(2).
Terweij, M., T. van Welsem, S. van Deventer, K. F. Verzijlbergen, V. Menendez-Benito, D. Ontoso, P. San-Segundo, J. Neefjes and F. van Leeuwen (2013). "Recombination-Induced Tag Exchange (RITE) Cassette Series to Monitor Protein Dynamics in Saccharomyces cerevisiae." G3 Genes|Genomes|Genetics **3**(8): 1261-1272.
Thaller, D. J., D. Tong, C. J. Marklew, N. R. Ader, P. J. Mannino, S. Borah, M. C. King, B. Ciani and C. P. Lusk (2021). "Direct binding of ESCRT protein Chm7 to phosphatidic acid–rich membranes at nuclear envelope herniations." Journal of Cell Biology **220**(3).
Timney, B. L., B. Raveh, R. Mironska, J. M. Trivedi, S. J. Kim, D. Russel, S. R. Wente, A. Sali and M. P. Rout (2016). "Simple rules for passive diffusion through the nuclear pore complex." J Cell Biol **215**(1): 57-76.
Towbin, B. D., P. Meister and S. M. Gasser (2009). "The nuclear envelope--a scaffold for silencing?" Curr Opin Genet Dev **19**(2): 180-186.
van Meer, G. and A. I. P. M. de Kroon (2011). "Lipid map of the mammalian cell." Journal of Cell Science **124**(1): 5-8.
van Meer, G., D. R. Voelker and G. W. Feigenson (2008). "Membrane lipids: where they are and how they behave." Nature Reviews Molecular Cell Biology **9**(2): 112-124.
Vitale, J., A. Khan, A. Neuner and E. Schiebel (2022). "A perinuclear α-helix with amphipathic features in Brl1 promotes NPC assembly." Molecular Biology of the Cell **33**(5): ar35.
Voeltz, G. K., W. A. Prinz, Y. Shibata, J. M. Rist and T. A. Rapoport (2006). "A Class of Membrane Proteins Shaping the Tubular Endoplasmic Reticulum." Cell **124**(3): 573-586.
Vollmer, B., M. Lorenz, D. Moreno-Andrés, M. Bodenhöfer, P. De Magistris, Susanne A. Astrinidis, A. Schooley, M. Flötenmeyer, S. Leptihn and W. Antonin (2015). "Nup153 Recruits the Nup107-160 Complex to the Inner Nuclear Membrane for Interphasic Nuclear Pore Complex Assembly." Developmental Cell **33**(6): 717-728.
Vollmer, B., A. Schooley, R. Sachdev, N. Eisenhardt, A. M. Schneider, C. Sieverding, J. Madlung, U. Gerken, B. Macek and W. Antonin (2012). "Dimerization and direct membrane

interaction of Nup53 contribute to nuclear pore complex assembly." The EMBO journal **31**(20): 4072-4084.
Weber, T., B. Zemelman, J. McNew, B. Westermann, M. Gmachl, F. Parlati, T. Sollner and J. Rothman (1998). SNARE dependent membrane fusion. MOLECULAR BIOLOGY OF THE CELL, AMER SOC CELL BIOLOGY PUBL OFFICE, 9650 ROCKVILLE PIKE, BETHESDA, MD 20814 USA.
Weberruss, M. and W. Antonin (2016). "Perforating the nuclear boundary – how nuclear pore complexes assemble." Journal of Cell Science **129**(24): 4439-4447.
Webster, Brant M., P. Colombi, J. Jäger and C. P. Lusk (2014). "Surveillance of Nuclear Pore Complex Assembly by ESCRT-III/Vps4." Cell **159**(2): 388-401.
Webster, M., K. L. Witkin and O. Cohen-Fix (2009). "Sizing up the nucleus: nuclear shape, size and nuclear-envelope assembly." Journal of Cell Science **122**(10): 1477-1486.
Wen, W., J. L. Meinkotht, R. Y. Tsien and S. S. Taylor (1995). "Identification of a signal for rapid export of proteins from the nucleus." Cell **82**(3): 463-473.
Wente, S. R. and G. Blobel (1993). "A temperature-sensitive NUP116 null mutant forms a nuclear envelope seal over the yeast nuclear pore complex thereby blocking nucleocytoplasmic traffic." Journal of Cell Biology **123**(2): 275-284.
Yang, Y., L. Guo, L. Chen, B. Gong, D. Jia and Q. Sun (2023). "Nuclear transport proteins: structure, function, and disease relevance." Signal Transduction and Targeted Therapy **8**(1): 425.
Yewdell, W. T., P. Colombi, T. Makhnevych and C. P. Lusk (2011). "Lumenal interactions in nuclear pore complex assembly and stability." Molecular Biology of the Cell **22**(8): 1375-1388.
Yuan, F., H. Alimohamadi, B. Bakka, A. N. Trementozzi, K. J. Day, N. L. Fawzi, P. Rangamani and J. C. Stachowiak (2021). "Membrane bending by protein phase separation." Proceedings of the National Academy of Sciences **118**(11): e2017435118.
Zabel, U., V. Doye, H. Tekotte, R. Wepf, P. Grandi and E. C. Hurt (1996). "Nic96p is required for nuclear pore formation and functionally interacts with a novel nucleoporin, Nup188p." Journal of Cell Biology **133**(6): 1141-1152.
Zhang, W., A. Khan, J. Vitale, A. Neuner, K. Rink, C. Lüchtenborg, B. Brügger, T. H. Söllner and E. Schiebel (2021). "A short perinuclear amphipathic α-helix in Apq12 promotes nuclear pore complex biogenesis." Open Biology **11**(11): 210250.
Zhang, W., A. Neuner, D. Rüthnick, T. Sachsenheimer, C. Lüchtenborg, B. Brügger and E. Schiebel (2018). "Brr6 and Brl1 locate to nuclear pore complex assembly sites to promote their biogenesis." J Cell Biol **217**(3): 877-894.
Zhendre, V., A. Grélard, M. Garnier-Lhomme, S. Buchoux, B. Larijani and E. J. Dufourc (2011). "Key role of polyphosphoinositides in dynamics of fusogenic nuclear membrane vesicles." PLoS One **6**(9): e23859.
Zhukovsky, M. A., A. Filograna, A. Luini, D. Corda and C. Valente (2019). "Phosphatidic acid in membrane rearrangements." FEBS Lett **593**(17): 2428-2451.